Viscoelastic Modelling of Road Deflections for use with the Traffic Speed Deflectometer

Pedersen, Louis

Publication date:
2013

Document Version
Publisher's PDF, also known as Version of record

Viscoelastic Modelling of Road Deflections for use with the Traffic Speed Deflectometer

An industrial Ph.D. study in collaboration with Greenwood Engineering, Technical University of Denmark and the Ministry of Science and Innovation

Author:

Louis Pedersen
louis@greenwood.dk

Main supervisor:

Associate Professor Poul G. Hjorth, Ph.D.
Department of Mathematics - Technical University of Denmark
pghj@dtu.dk

Co-supervisor:

Associate Professor Kim Knudsen, Ph.D.
Department of Mathematics - Technical University of Denmark
K.Knudsen@mat.dtu.dk

Greenwood Engineering supervisor:

Civil Engineer Jørgen A. Krarup, Ph.D.
jk@greenwood.dk

Study period: 1/9/2009 - 30/11/2012.

Preface

Introduction

This text is the dissertation written as part of the industrial Ph.D. project "Viscoelastic Modelling of Road Deflections for use with the Traffic Speed Deflectometer" by the author Louis Pedersen in collaboration with the Department of Mathematics at the Technical University of Denmark and financed by Greenwood Engineering and the Ministry of Science and Innovation in Denmark. The study ran from Sep 1. 2009 to Nov 30. 2012.
The research question arching over this project is: How can mathematical modelling provide further insight into the data collected from the Traffic Speed Deflectometer?
The main thesis statement is:
A new model based on more advanced and realistic mathematical simulation of asphalt physics can fit data from the Traffic Speed Deflectometer better and further useful information can be extracted from this data.
This text is the documentation of pursuing this thesis statement and the research, methods and solutions that sprang from this work.

Acknowledgements

The author would like to thank the following for their contributions and support:
Special thanks go to my wife, Kealey Dias, Ph.D. for both her loving support, helpful advice and mathematical discussions.
Huge thanks also goes to my supervisors, at DTU Mathematics, Associate Professor Poul G. Hjorth, Ph.D. and Associate Professor Kim Knudsen, Ph.D, and my Greenwood supervisor, Engineer Jørgen Krarup, Ph.D.
Furthermore thanks goes to the CEO of Greenwood Engineering Leif Grønskov for choosing to fund the project and TSD expert Research Engineer Søren Rasmussen for his help.
My office roommate at DTU Mathematics in office 111 Ph.D. candidate Michael Elmegård deserves a mentioning too for help with hard work when needed and help with fun distractions when needed.
Appreciation also goes out to the Technical University of Denmark as a whole and in particular for allowing a 3-month extension so as to be able to deliver a more complete work.
And thank you all to the rest of the Department of Mathematics, Greenwood Engineering and

the Ministry of Science and Innovation.
The author appreciates being allowed to use the ViscoRoute software from Laboratoire Central des Ponts et Chaussées (LCPC), which is now in the Institute Français des Sciences et Technologies, des Transports, de l'Aménagement et des Réseaux (IFSTTAR) - see [Chabot et al.] and [Chabot et al., 2009] for ViscoRoute information.

Abstract - English

This Ph.D. study is at its core about how asphalt and road structures responds to dynamic loads.
Existing models for the deflections under a moving load using beam equations are revisited and it is concluded they leave room for improvement for the particular setup and problem at hand.
Then a different approach is set up to model visco-elastic deflections starting from the physically based framework of continuum mechanics by using Finite Element Methods (FEM) combined with the Laplace transform.
It is shown that this approach coincides with a more standard time-stepping FEM setup in the case of a generalized Maxwell model.
Validations by comparison to ViscoRoute simulations are also made.
This justifies the use of the Laplace FEM for generating simulated data using a Huet-Sayegh model for the visco-elastic behaviour of asphalt.
These simulated data, along with measured data, are then used to suggest an approach for a computationally simpler synthetic model capturing essential behaviour of deflection bassins under a moving wheel.

Additionally the setup allows for simulated comparisons of the cases of loadings emulating the use of a Falling Weight Deflectometer with loadings emulating a moving wheel as in the case of using a Traffic Speed Deflectometer. The flexibility of the method also allows for looking into cases excluded by imposing simplifying assumptions such as the structure imagined to be an infinite halfspace.

Resumé - Dansk (In Danish)

Omdrejningspunktet i dette ph.d.-studie er hvorledes asfalt og vejkonstruktioner reagerer på dynamiske belastninger.
Eksisterende modeller for deflektioner under en belastning der bevæger sig, der benytter sig af bjælkeligninger, bliver genbesøgt og det konkluderes at de efterlader plads til forbedringer til den konkrete anvendelse her.
En anden fremgangsmåde benyttes derfor til at modellere visko-elastiske deflektioner med udgangspunkt i den fysisk baserede kontekst af kontinuum-mekanik ved brug af Finite Element Metoder (FEM) kombineret med Laplace-transformationen.
Det bliver eftervist at denne fremgangsmåde stemmer overens med en mere standard tidsskridt-baseret FEM i tilfældet af en generaliseret Maxwell model.
Der valideres yderligere ved sammenligning med ViscoRoute-simulationer.
Dette retfærdiggør brugen af Laplace-FEM til at generere simulerede data ved brug af en Huet-Sayegh model for den visko-elastiske opførsel af asfalt.
Disse simulerede data bruges dernæst sammen med målte data til at foreslå en fremgangsmåde for en beregningsmæssigt simplere syntetisk model, der fanger essentielle aspekter af deflektionsbassiners opførsel under et hjul der bevæger sig.

Ydermere tillader opsætningen simulerede sammenligninger imellem situationerne ved belastninger der emulerer belastningen fra et faldlod og en belastning der emulerer et Traffic Speed Deflektometer. Fleksibiliteten af metoden tillader også studier af tilfælde der udelades når der påtrykkes simplificerende antagelser såsom at strukturen er et uendeligt halvrum.

Contents

Chapter 1

Introduction

This section introduces the project, the actors involved and gives a brief insight into the history and timeline of this Ph.D. study.

1.0.1 Greenwood Engineering

Here a brief introduction and overview of the funding company is given to help explain the background of the project.
Greenwood Engineering is a company with the main office located in Brøndby[1] which is a suburb to Copenhagen, the capital of Denmark. Greenwood Engineering employs around 30 people and has an office in Beijing, China for local sales and support in that region.
The company produces solutions regarding measurements for the transport sector with different products for both railway and road management.
Examples of these products are profilers for measuring the longitudinal and transversal profile of the road utilizing lasers and MiniProf for measuring the profile of a railroad track very accurately.[2]
The product which is the pivotal point for this project and dissertation is the Traffic Speed Deflectometer (TSD), which I will explain in further detail in section 2.

1.0.2 ESGI and DTU Mathematics

Greenwood Engineering participated in the 55th European Study Group wth Industry (ESGI 55) in 2005. ESGI gathers, usually annually, mathematicians, engineers, physicists and others from the natural sciences to spend a week finding solutions to problems encountered in industry. It may be modelling of a phenomenon, statistics, optimizations and much more.
My main supervisor Associate Professor Poul G. Hjorth is often part of the organizing group for ESGI and his former master's student Lisbeth Aagaard Pedersen worked at Greenwood Engineering at the time. They brought to ESGI the problem of proposing a mathematical physics model for calculating deflection bassins from the TSD data. The problem was also

[1] Greenwood Engineering A/S, H. J. Holst Vej 3-5C, DK-2605 Brøndby, Denmark.
[2] The interested reader can go to `www.greenwood.dk` for more product or contact information.

turned into a Master's Thesis re-solving the problem and implementing proposed solutions by Jacob Ajslev Hersbøll in his "Undersøgelse af kørebanedeformationer ved hjælp af en Traffic Speed Deflectometer", [Jacob Ajslev Hersbøll, 2008].
This Ph.D. study can therefore be seen as a wish to continue the work started at ESGI, [Dias et al., 2005], and further advance this modelling and understanding of road structure dynamics. The author has since then experienced ESGI both as a participant and as an industry representative for Greenwood Engineering regarding another problem related to image recognition and I would like to take this opportunity to promote the initiative and similar concepts as it has been most rewarding.

1.0.3 About the Author

Another actor in this project is naturally the author. The author recieved his master of science degree from Aalborg University after studying there from 2003 to 2008 majoring in mathematics for 4 years with a 1-year minor in physics.
The focus of the degree was more of an abstract one and less on application and implementation. It was therefore very interesting to sign up for an industrial Ph.D. study which in its nature is very applied and sighted towards implementation. In an industry consisting mostly of engineers and their traditions the author feels it has been fruitful to come from a slightly different background and point of view at times - and believes fruitful discussions have been had with plenty lessons learned and hopefully a few taught as well.
The author is thankful for being allowed to take part in this project which must be said to be a good example of where mathematics, physics, and engineering meet, mixing theory with application. Enough about the author and moving on to the scientific content.

1.1 Nomenclature - Notation and Units

This section is to be used for reference for the use of units, symbols etc. throughout the text unless otherwise noted. Regarding the choice of units, this text uses SI units and tables 1.1 and 1.2 show units and prefixes respectively, while table 1.3 show some often used notations.

Table 1.1: A non-exhaustive nomenclature of units used.

Unit	Name	Description
kg	kilogram	mass
s	second	time
m	meter	length
Pa := kg/m^2	Pascal	pressure
rad	radian	angle

Table 1.2: A nomenclature of decadic prefixes used with the units of 1.1.

Prefix	Factor	Name
μ	10^{-6}	micro-
m	10^{-3}	milli-
c	10^{-2}	centi-
	1	
k	10^{3}	kilo-
M	10^{6}	mega-
G	10^{9}	giga-

Table 1.3: A non-exhaustive nomenclature of symbols used in this text.

Symbol	Unit	Description
ρ	kg /m^3	Density
E	Pa	Youngs Modulus
ν	1	Poisson Ratio
K	Pa	Bulk Modulus
G	Pa	Shear Modulus
x or x_1 [3]	m	Distance along the longitudinal direction of the road. [4]
y or x_2	m	Distance along the transversal direction of the road.
z or x_3	m	Distance along the vertical direction of the road.
$\mathbf{x}$	m	Vector notation for $(x_1, x_2, x_3) = (x, y, z)$.
t	s	Time
$\mathbf{u}$	m	Vector function for displacement $\mathbf{u}(\mathbf{x}, t) = \mathbf{X}(\mathbf{x}, t) - \mathbf{x}$.[5]
σ	N /m^2	Stress.
ε	1	Strain.
$\hat{f}$		Fourier transform of the function f. See Appendix .1 for details.
ω	rad /s	Angular frequency used in the Fourier Transform.
$\tilde{f}$		Laplace transform of the function f. See Appendix .2 for details.
s	rad /s	Complex frequency of the Laplace transform. See Appendix .2 for details.
c	rad /s	Re(s).
w	rad /s	Im(s).

Chapter 2

Traffic Speed Deflectometer Technology

This chapter introduces the Traffic Speed Deflectometer to the reader - explaining the design and principle of the apparatus.

2.1 Deflectometers in general

Deflectometers are instruments for measuring the deflection of a structure - in our case a pavement. The deflectometers for pavement use have a long history with various concepts having been tried throughout the years - some were meant to be placed, measure, move, and repeat (or measure while moving very slowly), which naturally limits the average speed of measuring and the speed moving along the road.
The earlier Lacroix deflectographs and Benkelman beams are examples of relatively slow moving deflectometer technologies doing mechanical measurements upon the road. It is important to remember that it is of interest to measure on actively used roads without having to interrupt the traffic flow.
A procedure involving moving and stopping or moving very slowly in traffic can and has been fatal during early deflectometer experiments of these older mechanical designs. Hence technologies able to do measurements near actual traffic speed on the move should in this sense be preferable.

Being able to survey an entire road network in the shortest amount of time is again naturally desirable by road authorities - less time spent measuring means possibly having time to check the network more often leading to a more up to date road management.

There are situations where speed of measurement is concievably less important:
Another natural use of deflectometers is during road construction, where the contractor promises to deliver a road complying with particular regulations and characteristics in particular ranges. The use of equipment by the contractor himself to survey the performance of a project or by the contracting customer at the product delivery does not necessarily require the same speed as the road is not in use. So regarding safety the speed is presumably less of a factor here.

However along with speed there is also the matter of resolution. Any system requiring stopping, moving, measuring etc. is likely to have fewer measurements along a given route. Any system will also have a resolution depending on the technology used - sensor type etc. System development naturally involves consideration of the noise involved with the sensor type used: mechanical contact or light/lasers for instance. The occurrence of noise necessitates performing rolling averages or similar approaches over a stretch of road. Hence even though some setups might be able to make actual measurement on a cm resolution of the road, an average over a certain distance, for instance 100 m might be necessary to eliminate noise.
Deflection measurement are used in conjunction with studies relating the deflection for various asphalt mixes to where the asphalt is in its life cycle. See [Vejregel Arbejdsgruppe P. 21, 2011a] for danish recommendations and [Y. Richard Kim, 2009] and [ARA, Inc. and Eres Consultants Division, 2004] for information on mechanistic-empirical approaches.
Data for such conclusions often come from (very) long term empirical studies on how asphalt wear and break down - a classic example is the American Association of State Highway Officials (ASHOO) road test[1] performed in the late 1950s which a massive effort in actually driving repeatedly on test sites in Ottawa, Illinois in the US.

One of the end goals of pavement management is of course to estimate the remaining life time of the asphalt so as to better plan repairs and spot deteriorating areas quickly. For pavement management purposes it is therefore important to establish that what is being spent time and efforts on measuring is related to useful parameters and indices for estimating the structural state and lifetime of the asphalt. Recent work such as [National Research Council (U.S.). Transportation Research Board and Universidad Católica de Chile and Ingenieria Dictus, 2011] establishes that curvature measurements, measured directly or computed from deflections, are correlated with strains in the bottom part of the base course, which again is known to be a strong predictor of asphalt breakdown - and hence is of great interest.
Work such as [National Research Council (U.S.). Transportation Research Board and Universidad Católica de Chile and Ingenieria Dictus, 2011] and [Axel O. Bohn, p. 3] tell how the centre deflection, often denoted d_0, by itself contains little information about the uppermost layers which are of principal interest. Other indices such as SCI300, often written as the difference af deflections in 0 mm and 300 mm, i.e. SCI300 $= d_0 - d_{300}$ are interesting and because of a differences slope-like nature is well-suited for the TSD which actually measures slopes as will be explained in section 2.2.1.

2.2 Design of the TSD

First and foremost a TSD in its entirety is a truck with the latest edition being sold, as of writing this fall 2012, to SANRAL in South Africa seen in the figure 2.1.
The TSD mostly consists of a truck fitted with a tightly regulated steel beam/frame inside the

[1] See `http://en.wikipedia.org/wiki/AASHO_Road_Test` and `http://www.fhwa.dot.gov/infrastructure/50aasho.cfm` for more information.

Figure 2.1: The SANRAL TSD with the tractor not painted. In this picture one can even see the odometer, measuring driving distance, behind the wheel and the extra measurement and scanning equipment mounted on the back of the trailer which in this truck has been combined into the same truck for a multipurpose vehicle.

trailer where Doppler laser sensors are installed. The number of sensors were originally 4, 3 doing the measurements and one reference laser. The latest TSDs as of 2012 have 7-10 sensor depending on the request of the customer.
The lasers are pointed at a slight angle at the road directly in front of the rear wheelset, illustrated in figure 2.2, at various distances. The wheelsets on the trailer are actually twin wheels and the lasers are mounted so as to measure in between, and specially designed hubs allow for measurements close to the centre of the twin-wheel-set.
The beam holding the sensors has fans for controlling the temperature, gyroscope/accelerometers to record movements and the lasers can be installed in various distances or the entire beam can be slid further back or forwards and clamped tightly onto the rail upon it moves to allow for measurements in different distances from the wheelset.
On the newer TSDs the slit and rail for the beam extends far enough backwards to measure with a couple of lasers behind the wheelset.[2]
The entire trailer is custom made and of course a lot of supporting systems are also built in, GPS, server racks, data acquisition boards - all of these are for the purpose of this report not relevant and the measurement principle is the main focus of this next section.

[2]Which is interesting given the viscoelastic nature of the road.

2.2.1 Measurement setup

For an overview of the measurement setup consider the (grossly exagerrated at places) illustration in figure 2.2.
The angle of incidence α between vertical and each laser beam is assumed quite small $\alpha \approx 2° \approx 0.035\,\text{rad}$. The deflection u_3 is also very small $\|\mathbf{u}\| << 1$. It is assumed that the deflection slope at the reference laser point P_{ref} of measurement is 0 so subtraction of the signal here from the other measurements eliminate noise stemming truck movements and the contribution of a driving speed component and left are velocity measurements in the vertical direction - measurements of $\frac{\partial u_3}{\partial t}$ at given points, see also 2.3.

Figure 2.2: An illustration of the measurement situation in full generality.

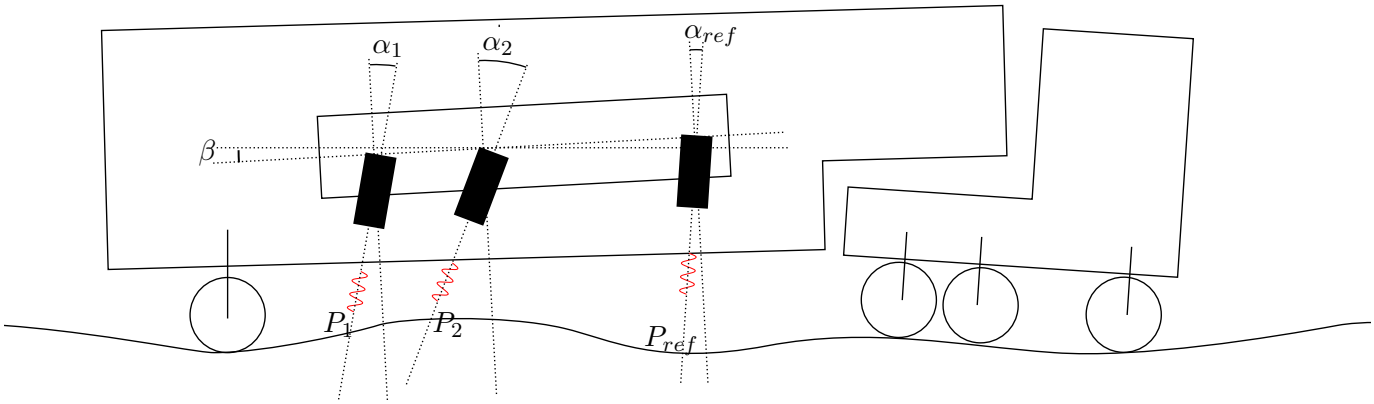

Figure 2.3: An illustration of the two components picked up by the TSD Doppler lasers. Because of the angling a component of driving speed is picked up.

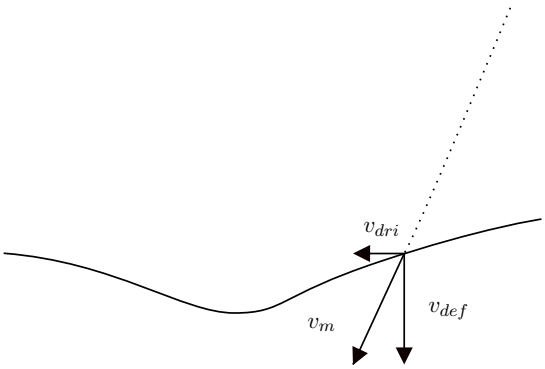

Building upon correspondence used by my main supervisor Poul G. Hjorth to further clarify the TSD principle after inquiry by a research institute for more information about the difference between the TSD principle and other deflectometer strategies - such as the Benkelman beam measuring mechanically or using triangulating laser for the deflection directly.
The TSD employs Doppler sensors from which the deflections are calculated using the following argument:
The Doppler sensors onboard the TSD measures pavement surface velocities. It does so by illuminating the road surface with one part of a beam split laser beam of a known frequency and a small amount will be reflected back into the Doppler device and recombined with half of the original beam. The difference in the frequency of the original beam and the reflected beam carries the frequency and thereby velocity information of the road surface. It is a wellknown application of interferometry called laser Doppler velocimetry or a laser Doppler vibrometer. Assuming a constant driving speed v and constant load a moving bassin shape Y is assumed in the moving X-frame given by $X := x - vt$. The deflection y in the x-frame stationary with the road can be written using this moving frame.[3]

$$y(x,t) = Y(x - vt) = Y(X) \tag{2.1}$$

The TSD measures, under the small deflection assumption and suitable corrections, instaneneously the vertical velocity $\frac{\partial y}{\partial t}$ at n laser position points $\{x_i\}, i = 1, \ldots, n$.

$$\frac{\partial y}{\partial t}(x,t) = \frac{\partial}{\partial t}Y(X) = -v\frac{\partial Y}{\partial X}(X). \tag{2.2}$$

Meaning that the slope of the instanteneous bowl shape is known at $\{x_i\}$ from the TSD-data divided by $-v$. To convert these into deflections where reasonably the deflection bassin is assumed to decay, $\lim_{X\to-\infty} Y(X) = 0$, the slope is naturally integrated:

$$Y(X) = -\frac{1}{v}\int_{-\infty}^{X} Y'(\chi)\mathrm{d}\chi. \tag{2.3}$$

Equation (2.3) is the reason why a deflection slope model is needed.

2.2.2 Need for a Deflection Model

A model is needed to go from the discrete measurement points to the full picture of the velocities which in turn can be used to calculate the deflection bassins. Hence it is not enough to invent a model fitting deflections of a road structure well - it is inherently important for this particular use that the model also fits well slope-wise.

[3] Later the letter y is reserved for the transverse direction.

2.2.3 The TSD as a product.

The entire TSD system has shown good repeatability and now has several authorities actively using it around the world collaborating with Greenwood Engineering on continued development of the product, procedures, and uses. This text will not delve deeper into the TSD as a product and the market it is meant for. The author refers interested readers to the following works containing more information on all aspects of the TSD, its competitors, uses etc.

- The results of the Danish Road Directorates doing measurements in Australia and evaluating there upon in [Baltzer et al., 2010]
- A repeatability test performed in Denmark between Greenwood and the Danish Road Directorate in [Rasmussen et al., 2008]
- A trial and study of the measurement principle [Simonin et al., 2003]

2.3 Brief Introduction to Road Structures and Materials

This sections aims to clarify the physical and structural situation and conditions under which the TSD operates - especially the structure of typical roads. See for instance [Y. Richard Kim, 2009] for more information about asphalts and deterioration processes.[4] There are many types of road design and a multitude of different asphalts, binders, concretes, aggregates and soils with different strategies and preferences around the world both due to tradition, availability of ressources and different needs of which a great deal stems from different climate conditions.

2.3.1 Anatomy of Asphalt

First and foremost it is important to notice the differences in connotation between American and British English words related to this topic to avoid confusion.[5]

This study is based out of Denmark and this text generally use British English so here an attempt is made to follow the wordings as common outside the United States. Asphalt here refers to a mix of binding material called bitumen and aggregate material.[6] This text does not focus around the mixing and the chemical properties of different asphalts other than the structural properties regarding stiffness and viscosity. Properties regarding interaction, noise generation, roughness, and the like are also not considered.
What is important for the purposes here is remembering that asphalt consists of primarily two parts: a bituminous binder and an aggregate material.
The grading, i.e. the size distribution, of the aggregate can vary quite a lot in both asphalt and the subbase material. Three important points are the following:

[4] http://www.highwaysmaintenance.com/design.htm and its front page is a nice source of easily accessible overviews maintained by C.J. Summer, a retired Materials Engineer.

[5] `http://en.wikipedia.org/wiki/Asphalt` does a good job at clarifying this.

[6] In American English texts this is mostly seen called asphalt concrete with asphalt referring to the bitumen.

1. Asphalt is interlocked materials that are very stiff and hard - i.e. rocks - held together by a binder.

2. The bituminous binding material is a hydrocarbon material and in the similar pitch - meaning it appears solid but is actually viscous and flows.

3. Bituminous materials are quite sensitive to temperatures - even temperatures within the working conditions of roads.

2.3.2 Anatomy of a Typical Pavement

The road structure assumed in this text consists of at most 4 layers which from the top down are designated as follows - see figure 2.4:

Figure 2.4: Layers of a road structure as assumed in this study.

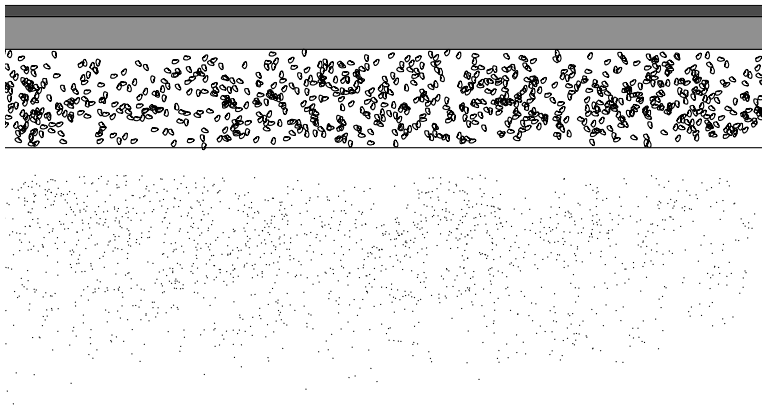

1. On top a wearing course consisting of a finer asphalt often intended for keeping water out and providing good driving experience parameters - ie. acceptable friction, noise and roughness.

2. Next is a base course - a often coarser and stiffer asphalt for spreading the load from the wearing course, providing an even platform for the wearing course and in some designs keep water out instead of the wearing course.

3. The subbase below the base course often consists of unbound materials, gravel or the like and functions as a drainage layer coupled with some form of runoff to drain water away from the road structure.

4. Subgrade is the term used for the bottom layer - most often natural soil.

There can be more layers, maybe especially for drainage purposes or to support a weak subgrade, but road construction strategies and designs are not delved into here. The reader is just presented this basic terminology and understanding of a road structure.

2.3.3 Comparison to Falling Weight Deflectometer

Another technology belonging to the same class of monitoring systems as the TSD are Falling Weight Deflectometers (FWD). FWDs have been in service for a long time and is therefore a stable of the industry with a lot of experience behind their usage. Along with experience comes establised standards and procedures for its use and the interpretation of measurements. The TSD being a newer technology does not have the same foothold in the market and it is of course necessary to prove that a new technology can, be competetive of course, but also bring new advantages to the table.
A comparison between the FWD and the TSD is therefore natural and understanding the relationship between the respective data could help immensely with establishing procedures, standards, backcalculations and the like for the TSD - possibly even using TSD data directly in FWD procedures. The TSD and FWD measures in different ways and on different loading strategies - they are not expected to give exactly the same output so understanding the differences and comparing would be a good validation and supporting documention.
Interesting info on the workings and history of the FWD can be found by the interested reader on the website for Grontmij `http://sites.grontmij.dk/Pavement-consultants-com/About-us/Fwd-history/Pages/default.aspx` where the text [Axel O. Bohn] is also available. Regarding the topic of speed as brought up in section 2.1 a speed of up to 60 measurement points per hour is reported by Dynatest[7], a manufacturer of FWDs via their website.
The mathematical assumptions regarding the loading for a representative FWD, see figure 2.5, as used in the report is described in section 5.4.2.

Figure 2.5: A Falling Weight Deflectometer of Grontmijs PRIMAX series [8].

[7] Brochures via. `http://www.dynatest.com/structural-hwd-fwd.php?tab=structural`

[8] As seen on `http://sites.grontmij.dk/Pavement-consultants-com/About-us/Fwd-history/Pages/default.aspx`

Chapter 3

Generalizing the ESGI Model

3.1 The Original and why more is needed

The crux of the matter regarding the need of a new model is the following. The early TSDs to be sold had 3 measurement laser and 1 reference laser. With 3 data points at most a 2-parameter model family should be used for the data fit. The beam model that was proposed as the foundation for a modelling method in [Dias et al., 2005] illustrated in figure 3.1 is governed by equation (3.1)[1]:

$$\left(EI\frac{\partial^4}{\partial X^4} + k_0\right) u(X) = -F\delta(X) \quad , \quad X \in \mathbb{R}, \tag{3.1}$$

subjected to the boundary condition that $\lim_{X\to\pm\infty} u(X) = 0$, where EI is the bending stiffness or flexural rigidity of the beam as given by the Young's modulus E[Pa] and the second moment of inertia I [m^4] and where F[N/m] is the load distribution and k_0[N/m^2] is the spring coefficient per length of the Winkler foundation.
As mentioned in section 1.0.2 one solution approach is shown in [Jacob Ajslev Hersbøll, 2008] however in the following, a slightly different approach will be used as serve as an illustration for the same method applied to a more general model attempting to get a better fit with data from more sensors than the original model was designed for:
By Fourier transforming equation (3.1), see Appendix .1, it follows:

$$\left(EI(iz)^4 + k_0\right)\hat{u}(z) = -\frac{F}{\sqrt{2\pi}} \quad , \quad z \in \mathbb{C}, \tag{3.2}$$

The characteristic equation for equation (3.1) is thus

[1] Where the vertical deflection is now u in the variable X conflicting slightly with our normal use of $\mathbf{u}$ for the deflection vector and $\mathbf{X}$ as the new position of a material point.

Figure 3.1: Proposed ESGI Model.

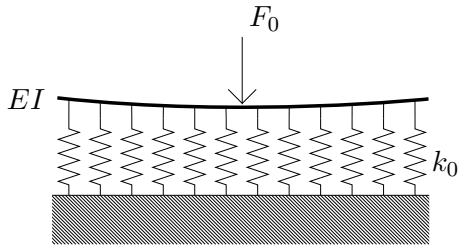

$$z^4 + 4\frac{k_0}{4EI} = 0 \tag{3.3}$$

$$z = \pm\sqrt[4]{\frac{k_0}{4EI}}(1+i) \vee \pm\sqrt[4]{\frac{k_0}{4EI}}(1-i) \tag{3.4}$$

$$\tag{3.5}$$

Define the following parameter to keep in line with the previously mentioned authors [Dias et al., 2005] and [Jacob Ajslev Hersbøll, 2008]:

$$B := \sqrt[4]{\frac{k_0}{4EI}}. \tag{3.6}$$

The inverse Fourier transform needed to get back to u is now solved via. the Cauchy Residue Theorem - see Appendix .1 and Appendix .6 respectively. For $X \geq 0$ by choosing a semicircular contour in the upper halfplane encircling two of the roots from (3.3):

$$u(X) = \frac{1}{\sqrt{2\pi}} \int_{-\infty}^{\infty} -\frac{F}{EI}\frac{1}{\sqrt{2\pi}}\frac{e^{iXk}}{k^4 + 4B^4}\mathrm{d}k \tag{3.7}$$

$$= 2\pi i \left(-\frac{1}{2\pi}\frac{F}{EI}\frac{e^{iXB(1+i)}}{4B^3(1+i)^3} - \frac{F}{EI}\frac{e^{iXB^3(-1+i)}}{4B(-1+i)^3} \right) \tag{3.8}$$

$$= -i\frac{F}{B^3EI}\left(\frac{e^{iXB(1+i)}}{4(1+i)^3} + \frac{e^{iXB(-1+i)}}{4(-1+i)^3} \right) \tag{3.9}$$

$$\tag{3.10}$$

$$u(X) = -\frac{F}{B^3EI} i \left(\frac{e^{iBX(1+i)}}{4(1+i)^3} + \frac{e^{iBX(-1+i)}}{4(-1+i)^3} \right) \tag{3.11}$$

$$= -\frac{1}{4}\frac{F}{B^3EI} i \left(\frac{e^{iBX(1+i)}}{-2+2i} + \frac{e^{iBX(-1+i)}}{2+2i} \right) \tag{3.12}$$

$$= -\frac{1}{4}\frac{F}{B^3EI} i \left(\frac{(2+2i)e^{iBX(1+i)} + (-2+2i)e^{iBX(-1+i)}}{(2+2i)(-2+2i)} \right) \tag{3.13}$$

$$= -\frac{1}{8}\frac{F}{B^3EI} e^{-BX} \left(\frac{(e^{iBX} + e^{-iBX})}{2} + \frac{(e^{iBX} - e^{-iBX})}{2i} \right) \tag{3.14}$$

$$= -\frac{1}{8}\frac{F}{B^3EI} e^{-BX}(\cos(BX) + \sin(BX)), \tag{3.15}$$

and similarly for $X < 0$ except for a few signs giving:

$$u(X) \quad = \quad -\frac{1}{8}\frac{F}{B^3EI} e^{BX}(\cos(BX) - \sin(BX)) \quad , \quad X < 0 \tag{3.16}$$

Regarding the above B:

$$B^2 = \sqrt{\frac{k}{4EI}} \Rightarrow \frac{F}{2EI} = \frac{F}{B^3EI} = \frac{F}{8B\sqrt{\frac{k}{4EI}}EI} = \frac{F}{2^2B\sqrt{kEI}} \tag{3.17}$$

By defining

$$A := \frac{F}{2\sqrt{kEI}}, \tag{3.18}$$

the solution to equation (3.1) composed from equations (3.11) and (3.16) becomes

$$u(X) = \begin{cases} -\frac{A}{2B} e^{BX}(\cos(BX) - \sin(BX)) & , \quad X < 0 \\ -\frac{A}{2B} e^{-BX}(\cos(BX) + \sin(BX)) & , \quad X \geq 0 \end{cases} \tag{3.19}$$

Note that regardless of the choice of parameters A and B the solutions have oscillatory behaviour, which is an important feature to determine whether is a realistic and true physical phenomenon or not.

3.1.1 Extended Beam Model

The goal of this section is to extend the previous beam model expressed by equation (3.1) to include more parameters and consider the effects of different assumptions regarding the loading: The hope is of course a better fit with real data especially considering the original ESGI model was based on the use of 3 measuring lasers and the TSD devices are since then being built with more (6-9) depending on the preferences of the customer. Also the introduction of more

parameters, especially in a damping term, will introduce the possibility of asymmetric bassins around the load which are to be expected in cases of visco-elastic asphalt.

Figure 3.2: Generalization of the ESGI Model. In [Andersen, 2002] referred to as a Kelvin-Pasternak foundation[2].

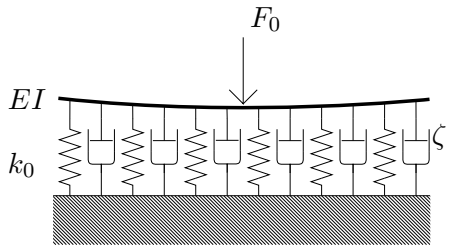

The starting point is to consider a beam equation in the frame of the road where the load is moving:

$$\left(\mu\frac{\partial^2}{\partial t^2} + EI\frac{\partial^4}{\partial x^4} + \zeta\frac{\partial}{\partial t} + k_0\right) u(x,t) = f(x,t) \quad , \quad (x,t) \in \mathbb{R}\times\mathbb{R}_+ \tag{3.20}$$

where $\mu[\mathrm{kg\,m^{-1}}]$ is the mass per length of the beam, $EI[\mathrm{Pa{\cdot}m^4}]$ is the flexural rigidity, ζ $[\mathrm{kg/(m{\cdot}s)}]$ is a damping coefficient per length and $k_0[\frac{N}{m^2}]$ is the spring coefficient per length of the foundation.
Assuming that the load is a static profile moving at velocity v :

$$f(x,t) = f(x-vt), \tag{3.21}$$

A change of coordinates to a frame co-moving with the load profile f:

$$X = x - vt \tag{3.22}$$
$$t' = t, \tag{3.23}$$

implies:

$$\frac{\partial}{\partial t} = -v\frac{\partial}{\partial X} + \frac{\partial}{\partial t'} \tag{3.24}$$
$$\frac{\partial^2}{\partial t^2} = (-v)^2\frac{\partial^2}{\partial X^2} + \frac{\partial^2}{\partial t'^2} - 2v\frac{\partial^2}{\partial X\partial t'} \tag{3.25}$$
$$\frac{\partial}{\partial x} = \frac{\partial}{\partial X}. \tag{3.26}$$

[2]Except the shear stiffness and viscosity parameters included there.

With

$$u^*(X,t') := u(X+vt',t') = u(x,t) \tag{3.27}$$

and assuming without loss of generality the point load sits at $X=0$ so

$$f(x,t) = f(x-vt) = -\lambda\delta(x-vt) = -\lambda\delta(X). \tag{3.28}$$

In (X,t')-coordinates equation (3.20) becomes:

$$\left(\mu(-v)^2\frac{\partial^2}{\partial X^2} + \mu\frac{\partial^2}{\partial t'^2} - 2v\mu\frac{\partial^2}{\partial X\partial t'} + EI\frac{\partial^4}{\partial X^4} - \zeta v\frac{\partial}{\partial X} + \zeta\frac{\partial}{\partial t'} + k_0\right)u^*(X,t') = -\lambda\delta(X) \tag{3.29}$$

Assuming the deformation is static is the frame of the load i.e. $u^*(X,t') = u^\dagger(X)$:

$$\left(\mu v^2\frac{\partial^2}{\partial X^2} + EI\frac{\partial^4}{\partial X^4} - \zeta v\frac{\partial}{\partial X} + k_0\right)u^\dagger(X) = -\lambda\delta(X) \tag{3.30}$$

For nondimensionalization it is noted that the equations contains the following 3 fundamental units: kg, m, s and the following 6 parameters: $EI, \mu, v, \zeta, k, \lambda$. This implies $6-3=3$ dimensionless parameters C_2, C_1, C_0 governing the problem and they will be defined shortly. See for instance [Sablani et al., 2006]
Introducing a scaling α implies (and recycling the notation u^* for the function of the next variable):

$$\alpha X' = X \tag{3.31}$$

$$u^*(X') := u^\dagger\left(\frac{X'}{\alpha}\right) = u^\dagger(X) \tag{3.32}$$

$$\frac{d}{dX} = \frac{dX'}{dX}\frac{d}{dX'} = \frac{1}{\alpha}\frac{d}{dX'} \Rightarrow \tag{3.33}$$

$$\frac{d^2}{dX^2} = \frac{1}{\alpha^2}\frac{d^2}{dX'^2} \tag{3.34}$$

$$\frac{d^4}{dX^4} = \frac{1}{\alpha^4}\frac{d^4}{dX'^4} \tag{3.35}$$

The scaled point load is given as:

$$\delta(X) = -\lambda\delta(\alpha X') = -\lambda\frac{\delta(X')}{|\alpha|} = -\lambda\frac{\delta(X')}{\alpha} \tag{3.36}$$

$$\left(\frac{EI}{\alpha^4}\frac{\partial^4}{\partial X'^4} + \frac{\mu v^2}{\alpha^2}\frac{\partial^2}{\partial X'^2} - \frac{\zeta v}{\alpha}\frac{\partial}{\partial X'} + k_0\right)u^*(X') = \frac{\delta(X')}{|\alpha|} \tag{3.37}$$

$$\left(\frac{\partial^4}{\partial X'^4} + \frac{\alpha^2\mu v^2}{EI}\frac{\partial^2}{\partial X'^2} - \frac{\zeta v\alpha^3}{EI}\frac{\partial}{\partial X'} + \frac{k_0\alpha^4}{EI}\right)u^*(X') = -\frac{\lambda\alpha^3}{EI}\delta(X') \tag{3.38}$$

$$\tag{3.39}$$

Setting $\alpha = \sqrt[3]{\frac{EI}{\lambda}} \geq 0$ and defining $C_2 := \frac{\alpha^2 \mu v^2}{EI} \geq 0$, $C_1 := \frac{\zeta v \alpha^3}{EI} \geq 0$, $C_0 := \frac{k_0 \alpha^4}{EI} \geq 0$ gives the equation:

$$\left(\frac{\partial^4}{\partial X'^4} + C_2 \frac{\partial^2}{\partial X'^2} - C_1 \frac{\partial}{\partial X'} + C_0 \right) u^*(X') = -\delta(X'). \tag{3.40}$$

Doing a Fourier transform of equation (3.40).

$$\left((ik)^4 + C_2 (ik)^2 - C_1 ik + C_0 \right) \hat{u}(k) = -\frac{1}{\sqrt{2\pi}} \tag{3.41}$$

$$\left(k^4 - C_2 k^2 - C_1 ik + C_0 \right) \hat{u}(k) = -\frac{1}{\sqrt{2\pi}} \tag{3.42}$$

The strategy is to again use contour integration for the inversion of the Fourier transformed solution and look at the family of solutions. Define the polynomial p:

$$p(z) := z^4 - C_2 z^2 - C_1 iz + C_0 \tag{3.43}$$

The following observation regarding symmetry around the imaginary axis of the roots of p in (3.43) is made:

$$\begin{aligned} p(z) = p(a+ib) &= 0 \Rightarrow \\ (a+ib)^4 - C_2(a+ib)^2 - iC_1(a+ib) + C_0 &= 0 \Rightarrow \\ (a^4 + 4a(ib)^3 + 6a^2(ib)^2 + 4a^3 ib + (ib)^4) - C_2 a^2 + C_2 b^2 - 2C_2 abi - iC_1 a + C_1 b + C_0 &= 0 \\ (a^4 - 6a^2 b^2 + b^4 + C_1 b + C_0 - C_2 a^2 + C_2 b^2) + i(-4ab^3 + 4a^3 b + C_1 a - 2C_2 ab) &= 0 \end{aligned} \tag{3.44}$$

A root $r_1 = a + ib$ implies a root $r_2 = -a + ib$. Vieta's formulas and the lack of a z^3-term implies.

$$\begin{aligned} r_1 + r_2 + r_3 + r_4 &= 0 \\ (a+ib) + (-a+ib) + (-c+id) + (c+id) &= 0 \\ i(2b+2d) = 0 \Rightarrow b = -d. & \end{aligned} \tag{3.45}$$

Four roots of the complex polynomial $p(z)$ on the form:

$$\begin{aligned} r_1 &= a + ib \\ r_2 &= -a + ib \\ r_3 &= -c - ib \\ r_4 &= c - ib \end{aligned} \tag{3.46}$$

The idea now was to describe the solution parametrized in the numbers, a,b, and c, describing these roots and numerically fit this family of solutions to the data, with some constraints to

keep the physical parameters such as density etc. real and positive: Using the Residue Theorem as described in .6:

$$\begin{aligned}
u(x) &= \frac{1}{\sqrt{2\pi}}\int_{-\infty}^{\infty}\frac{1}{\sqrt{2\pi}}\frac{de^{ixk}}{k^4 - C_2k^2 - C_1ik + C_0} \\
&= \frac{1}{(\sqrt{2\pi})^2}2\pi di\left(\frac{e^{ix(a+ib)}}{(r_1-r_2)(r_1-r_3)(r_1-r_4)} + \frac{e^{ix(-a+ib)}}{(r_2-r_1)(r_2-r_3)(r_2-r_4)}\right) \\
&= die^{-bx}\left(\frac{e^{ixa}}{(r_1-r_2)(r_1-r_3)(r_1-r_4)} + \frac{e^{-ixa}}{(r_2-r_1)(r_2-r_3)(r_2-r_4)}\right) \\
&= die^{-bx}\left(\frac{e^{ixa}}{2a(a+c+2ib)(a-c+2ib)} + \frac{e^{-ixa}}{-2a(-a+c+2ib)(-a-c+2ib)}\right) \\
u'(x) &= di\left(i\frac{(a+ib)e^{ix(a+ib)}}{2a(a+c+2ib)(a-c+2ib)} + i\frac{(-a+ib)e^{ix(-a+ib)}}{-2a(-a+c+2ib)(-a-c+2ib)}\right) \\
&= -d\left(\frac{(a+ib)e^{ix(a+ib)}}{2a(a+c+2ib)(a-c+2ib)} + \frac{(-a+ib)e^{ix(-a+ib)}}{-2a(-a+c+2ib)(-a-c+2ib)}\right)
\end{aligned} \tag{3.47}$$

The reader will be spared of tedious calculations to further express the above solutions since another avenue will be take altogether.

The reason for this is moving the roots around to parametrize different solutions still produce solutions with behaviour not recognized from real data - oscillations, the type of decay etc. The new solution do not differ enough from the ESGI solution with its symmetrically placed roots. Now simple plate models are considered as an option.

3.1.2 Plate Model

Here an approach similar to the one used in 3.1.1 will be used to look at the simplest possible plate solution. Using the Laplacian

$$\Delta = \frac{\partial^2}{\partial X^2} + \frac{\partial^2}{\partial Y^2}, \tag{3.48}$$

the simplest plate model concievable for our use is a plate on a elastic foundation described by k_0

$$(\Delta\Delta + k_0)u(X,Y) = \delta(X,Y) \tag{3.49}$$

which 2D Fourier transforms into

$$(k_1^4 + k_2^4 + 2k_1^2k_2^2 + k_0)\hat{u}(k_1,k_2) = \frac{1}{2\pi} \tag{3.50}$$

$$u(X,Y) = \int_{\mathbb{R}^2} \frac{1}{2\pi} e^{i(Xk_1+Yk_2)} \frac{1}{k_1^4 + k_2^4 + 2k_1^2k_2^2 + k_0} \mathrm{d}k_1\mathrm{d}k_2. \tag{3.51}$$

The 2D inverse Fourier Transform in (3.51) can be done analytically for the strip $y = 0$ which is the strip of interest for our use with the TSD where measurements are assumed performed directly in front of the center of the load. By the following change of coordinates to standard polar coordinates, $r \in [0,\infty[, \theta \in [0, 2\pi[$:

$$k_1 = r\cos\theta \tag{3.52}$$

$$k_2 = r\sin\theta, \tag{3.53}$$

Equation (3.51) becomes for $y = 0$: [3]

$$u(X,0) = \int_0^{2\pi}\int_0^{\infty} \frac{1}{2\pi} e^{iXr\cos\theta} \frac{1}{r^4 + k_0} r\mathrm{d}r\mathrm{d}\theta \tag{3.54}$$

$$= \int_0^{\infty} \frac{1}{2\pi} \int_0^{2\pi} e^{iXr\cos\theta}\mathrm{d}\theta \frac{1}{r^4 + k_0} r\mathrm{d}r. \tag{3.55}$$

$$= \int_0^{\infty} \frac{2\pi}{2\pi} \mathrm{BesselJ}(0, Xr) \frac{1}{r^4 + k_0} r\mathrm{d}r. \tag{3.56}$$

which for $k_0 = 1$, for illustration purposes, can be expressed as a Meijer G-function using Maple(TM) 16 a registrered trademark of Maplesoft, a division of Waterloo Maple Inc., Waterloo, Ontario, see [Maplesoft].

$$u(X,0) = -\frac{1}{X}\mathrm{MeijerG}\left([[],[]], \left[\left[\frac{3}{4}, \frac{3}{4}, \frac{1}{4}\right], \left[\frac{1}{4}\right]\right], \frac{1}{256}X^4\right), \tag{3.57}$$

[3] A Bessel function of the first kind, order 0 is used.

Figure 3.3: Illustration of the solution for $x \geq 0$ from equation 3.57 by a Maple 16 graph.

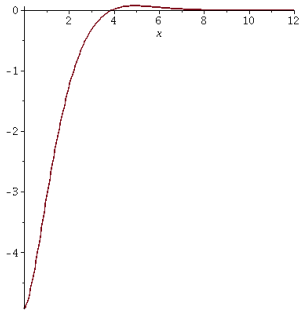

which is similarly oscillatory, see figure 3.3, and deemed not appropriate for the fitting data looking more as in figure 6.5. The author was working on a damped plate model and looking into an approach similar to the one found in [Hayes et al., 2000] where a Green's function is found for a plate equation plus a damping term, however before the work was completed this path was abandoned from similar reason as already mentioned regarding beams vs. damped beams.

3.1.3 Conclusion Regarding Beam and Plate Models

Interesting work on beam equation modelling can be seen in the Ph.D. thesis [Andersen, 2002] and the article [Hardy and Cebon, 1993].
In the article [Hardy and Cebon, 1993] the conclusion from the authors seems satisfied with the fit of the deflections for practical use. See the strain calculations and comments there [Hardy and Cebon, 1993, p. 1776-1778].

However the problem sought to be solved here involves not only deflections, but as mentioned in section 2.2.2 a good fit with the slopes is needed so as to fit the velocity data with a velocity model from which the deflections can be calculated. In [Hardy and Cebon, 1993] the strain plots also show the real data to not exhibit same oscillatory behaviour as the model predicts, which is amplified in the derivative.

It is the conclusion and belief of the author that the behaviour of beam and plate models differ too much in the metric of comparing the slopes implied by the models to get a satisfying fit with data from the TSD. The author has investigated but not found a satisfactorily simple way to fit beam and plate model with these behaviours and the right decay as the story told by data, figure 6.5. Attempting to rectify these shortcomings with more complex beam equations quickly leads to a situation where one loses the property of fairly easily expressed explicit solutions and hence a great deal of the convenience of the simplifying assumption ceases to apply.

The nature of the stress distribution in the continuum mechanics case with full 3D stress distributions is probably simply more involved than the Winkler foundation. Hence another approach was chosen within continuum mechanics, the topic of Chapter 4.

Chapter 4

Continuum Mechanics

This section serves to introduce the necessary continuum mechanics concept and equations which serve as the foundation for simulation of material behaviour. See also [A.C. Fowler, 1997] and [Carini et al., 2008].

4.1 Viscoelasticity

Considered here is a viscoelastic body described by the volume $\Omega(t) \subset \mathbb{R}^3$, $t \in T \subset \mathbb{R}$, deforming as described by the displacement vector function $\mathbf{u} : \mathbb{R}^4 \to \mathbb{R}^3$ under surface stresses given by the function $\mathbf{p} : \Gamma_1 \times \mathbb{R}_0^+ \to \mathbb{R}^3$ and prescribed deformations $\mathbf{g} : \Gamma_2 \times \mathbb{R}_0^+ \to \mathbb{R}^3$, where $\delta\Omega(t) = \Gamma_1(t) \cup \Gamma_2(t)$:

$$\rho(\mathbf{x})\frac{\partial^2 u_i}{\partial t^2}(\mathbf{x},t) = \frac{\partial \sigma_{ij}}{\partial x_j}(\mathbf{x},t) + f_i(\mathbf{x},t) \quad , \quad \Omega(t) \times T \tag{4.1}$$

with boundary stresses given, with the aid of the outwards normal vector ν to $\delta\Omega$, by

$$\sigma_{ij}(\mathbf{x},t)\nu_j(\mathbf{x},t) = p_i(\mathbf{x},t) \quad , \quad \Gamma_1(t) \times T \tag{4.2}$$

and deflections described as

$$u_i(\mathbf{x},t) = g_i(\mathbf{x},t) \quad , \quad \Gamma_2(t) \times T \tag{4.3}$$

with initial conditions at time $t = t_0$ denoted by:

$$\begin{aligned} u_i(\mathbf{x},t_0) &= U_i(\mathbf{x}) \quad , \quad \Omega(t_0) \\ \frac{\mathrm{d}u_i}{\mathrm{d}t}(\mathbf{x},t_0) &= v_i(\mathbf{x}) \quad , \quad \Omega(t_0) \end{aligned} \tag{4.4}$$

using the following strain definition for small strains:

$$\varepsilon_{ij}(\mathbf{x},t) = \frac{1}{2}\left(\frac{\partial u_i}{\partial x_j}(\mathbf{x},t) + \frac{\partial u_j}{\partial x_i}(\mathbf{x},t)\right) \quad , \quad \Omega(t) \times T \tag{4.5}$$

Also deformations are assumed small enough that geometric non-linearity can be neglected meaning the volume Ω is considered constant in time and hence the outwards normal vector

ν is also constant in time, allowing for a linear problem for the sake of being able to compute Laplace transforms.

$$\begin{aligned}\rho\frac{\partial^2}{\partial t^2}\mathbf{u}(\mathbf{x},t) - \nabla\cdot\sigma(\mathbf{x},t) &= \mathbf{f}(\mathbf{x},t) \\ \mathbf{u}(\mathbf{x},t) &= \mathbf{g}(\mathbf{x},t) \quad , \quad \mathbf{x}\in\Gamma_2 \\ \sigma(\mathbf{x},t):\nu(\mathbf{x},t) &= \mathbf{p}(\mathbf{x},t) \quad , \quad \mathbf{x}\in\Gamma_1\end{aligned} \tag{4.6}$$

Assumed now is furthermore that body forces are irrelevant so $\mathbf{f}$ is zero.

$$\begin{aligned}\rho s^2\tilde{\mathbf{u}}(\mathbf{x},s) - \nabla\cdot\tilde{\sigma}(\mathbf{x},s) &= 0 \\ \tilde{\mathbf{u}}(\mathbf{x},s) &= \tilde{\mathbf{g}}(\mathbf{x},s) \quad , \quad \mathbf{x}\in\Gamma_2 \\ \tilde{\sigma}(\mathbf{x},s):\nu(\mathbf{x}) &= \tilde{\mathbf{p}}(\mathbf{x},s) \quad , \quad \mathbf{x}\in\Gamma_1\end{aligned} \tag{4.7}$$

Equation (4.7) gives a series of stationary problems instead of a time-stepping problem. Meaning a set of complex frequencies are chosen and simulations are done for those. For the inversion described in Appendix .2.2 complex frequencies of the form $s = c + i\omega_n$, $n = 0, \cdots, N_{samp}$ are needed.

As in [Carini et al., 2008] one could look at

$$\sigma_{ij}(\mathbf{x},t) = \int_{-\infty}^{t} R_{ijhk}(\mathbf{x},t,\tau)\mathrm{d}\varepsilon_{hk}(\mathbf{x},\tau), \tag{4.8}$$

where the stresses σ is giving as an integral over a relaxation tensor kernel for the past until time t.

Assuming a starting time t_0 before which the system was unstressed and unstrained. That is $\sigma_{ij}(\mathbf{x},t) = 0$ and $\varepsilon_{ij}(\mathbf{x},t) = 0$ for $t < t_0$. and the further assumption of

$$\sigma_{ij}(\mathbf{x},t) = R_{ijhk}(\mathbf{x},t,t_0)\varepsilon_{hk}(\mathbf{x},t_0) + \int_{t_0^+}^{t} R_{ijhk}(\mathbf{x},t,\tau)\mathrm{d}\varepsilon_{hk}(\mathbf{x},\tau), \quad \Omega\times T \tag{4.9}$$

$$R_{ijhk}(\mathbf{x},t,t)\gamma_{ij}\gamma_{hk} > 0, \quad , \quad \mathbf{x}\in\Omega, t_0 \le t \le \infty, \tag{4.10}$$

for doubly symmetric tensors γ.

With the following for isotropic materials where R_1 is the shear relaxation and R_2 is the volumetric relaxation:

$$\begin{aligned}R_{ijhk}(\mathbf{x},t,\tau) &= \frac{1}{3}[R_2(\mathbf{x},t,\tau) - R_1(\mathbf{x},t,\tau)]\delta_{ij}\delta_{hk} + \frac{1}{2}R_1(\mathbf{x},t,\tau)[\delta_{ih}\delta_{jk} + \delta_{ik}\delta_{jh}] \Rightarrow \\ R_{ijhk}\varepsilon_{hk} &= \frac{1}{3}[R_2 - R_1]\delta_{ij}\delta_{hk}\varepsilon_{hk} + \frac{1}{2}R_1[\delta_{ih}\delta_{jk}\varepsilon_{hk} + \delta_{ik}\delta_{jh}\varepsilon_{hk}] \\ &= \frac{1}{3}[R_2 - R_1]\delta_{ij}\varepsilon_{kk} + \frac{1}{2}R_1[\varepsilon_{ij} + \varepsilon_{ji}] \\ &= \frac{1}{3}[R_2 - R_1]\delta_{ij}\varepsilon_{kk} + R_1\varepsilon_{ij}\end{aligned} \tag{4.11}$$

$$R_{ijhk}(\mathbf{x},t,\tau)\varepsilon_{hk}(\mathbf{x},\tau) = \frac{1}{3}[R_2(\mathbf{x},t,\tau) - R_1(\mathbf{x},t,\tau)]\delta_{ij}\varepsilon_{kk}(\mathbf{x},\tau) + R_1\varepsilon_{ij}(\mathbf{x},\tau). \tag{4.12}$$

Example 4.1.1. Note that with

$$R_1(\mathbf{x},t,\tau) = \begin{cases} 2G, & \text{if } \tau = t_0 \\ O, & \text{if } \tau \neq t_0 \end{cases} \tag{4.13}$$

$$R_2(\mathbf{x},t,\tau) = \begin{cases} 3K, & \text{if } \tau = t_0 \\ O, & \text{if } \tau \neq t_0 \end{cases}, \tag{4.14}$$

Hooke's Law (See [Mase and Mase, 1999] for instance.) is recovered

$$\begin{aligned} \sigma_{ij}(\mathbf{x},t) = R_{ijhk}(\mathbf{x},t,\tau)\varepsilon_{hk}(\mathbf{x},\tau) &= \frac{1}{3}[3K - 2G]\delta_{ij}\varepsilon_{kk}(\mathbf{x},\tau) + 2G\varepsilon_{ij}(\mathbf{x},\tau) \\ &= [K - \frac{2}{3}G]\delta_{ij}\varepsilon_{kk}(\mathbf{x},\tau) + 2G\varepsilon_{ij}(\mathbf{x},\tau). \end{aligned}$$

◇

The important parts here is equation (4.7) describing the transformed physics, leaving the choice of assumptions regarding the material behaviour to be described in the upcoming socalled constitutive equations..

4.2 Constitutive Equations

This section aims to introduce the necessary concepts for modelling visco-elasticity. Firstly what is meant by a visco-elastic material is a material which behaves like an everyday spring in the sense that when loaded it compresses and when loading is removed it fully recovers. Visco in visco-elasticity refers to viscous like fluids. Fluids does not support shear stresses and do not recover after loading, see [Mase and Mase, 1999, chap. 7] for instance. Asphalt partly consists of a binding material as mentioned in 2.3 and hence partly behaves in a viscous manner.

4.2.1 Viscoelasticiy and Rheological Models

When one sets up a model drawing springs and dampers in series and parallel what is conveyed is an assumption that a modulus of the system is governed approximately by analogous relations as the depicted system would relate stresses (forces per areas in the material) to strains (relative displacements) in a sense.

Imagining two components connected in serial. For instance 4.1.

Figure 4.1: Serially connected springs.

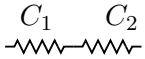

The total displacement ε_{tot} of the combined system must be the sum of the displacements of the components, so serial strains add.
The total stress σ_{tot} of two components in serial must be equal to the stress in each of them as stresses are forces per area and hence drawing a free-body diagram reveals that the serial stresses are equal by Newtons law of equal opposing action and reaction.
Considering a parallel connection the situation reverses and since the two components must give equally the strains are now equal.
Also the stresses add together as each component pushes back "side by side" so all in all the following are the rules for combining components and finding the governing equations of such models:

$$\begin{aligned} &\text{Serial} \\ &\varepsilon_{tot} = \varepsilon_1 + \varepsilon_2 \\ &\sigma_{tot} = \sigma_1 = \sigma_2 \\ &\text{Parallel} \\ &\varepsilon_{tot} = \varepsilon_1 = \varepsilon_2 \\ &\sigma_{tot} = \sigma_1 + \sigma_2. \end{aligned} \tag{4.15}$$

A spring relates stress to strain by proportionality with a spring constant denoted $C > 0, [\text{Pa}]$.

$$\sigma(t) \quad = \quad C\varepsilon(t). \tag{4.16}$$

A damper denotes a relation of stress to strain by proportionality with a factor denoted $\eta > 0, [\text{Pa} \cdot \text{s}]$ to the rate of change of strain.

$$\sigma(t) \quad = \quad \eta \frac{\mathrm{d}\varepsilon}{\mathrm{d}t}(t). \tag{4.17}$$

Example 4.2.1. Two springs in series (Figure 4.1) behaves as follows by using equations 4.15.

$$\begin{aligned} \varepsilon_{tot} &= \frac{\sigma_1(t)}{C_1} + \frac{\sigma_2(t)}{C_2} = \left(\frac{1}{C_1} + \frac{1}{C_2}\right)\sigma_{tot}(t) \\ \sigma_{tot}(t) &= \frac{1}{\frac{1}{C_1} + \frac{1}{C_2}}\varepsilon_{tot}, \end{aligned} \tag{4.18}$$

giving an equivalent total constant C_{tot} as follows:

$$C_{tot} = \frac{1}{\frac{1}{C_1} + \frac{1}{C_2}}. \tag{4.19}$$

Figure 4.2: Springs connected in parallel.

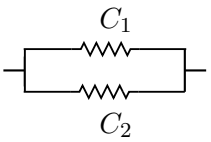

Two springs in parallel, figure 4.2, behaves as follows by using 4.15.

$$\sigma_{tot} \quad = \quad C_1\varepsilon_1 + C_2\varepsilon_2 = (C_1 + C_2)\varepsilon_{tot}(t) \tag{4.20}$$

giving an equivalent total constant C_{tot} as follows:

$$C_{tot} = C_1 + C_2 \tag{4.21}$$

$\diamond$

The above manipulations in example 4.2.1 giving equations (4.20) and (4.18) rests crucially upon the conversion between stress and strain being a simple multiplication.

Example 4.2.2.

Figure 4.3: Spring and damper connected in parallel, Kelvin model.

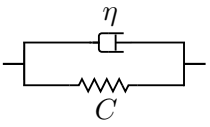

As an example consider a spring and damper in parallel (Kelvin model figure 4.3):

$$\sigma_{tot} \quad = \quad \eta\frac{\mathrm{d}\varepsilon_1}{\mathrm{d}t}(t) + C\varepsilon_2 = \eta\frac{\mathrm{d}\varepsilon_{tot}}{\mathrm{d}t}(t) + C\varepsilon_{tot}, \tag{4.22}$$

leaving a differential equation describing the relationship between stresses from strains.

$\diamond$

The rules or equations of (4.15) hold just as well under linear integral transforms such as the Fourier Transform - see Appendix .1 and the Laplace Transform - see Appendix .2.
Anticipating where the Huet-Sayegh model, to be introduced in equation (4.34), comes from: Assume a component is modelled by

$$\sigma(t) = \eta\frac{\partial^n \varepsilon}{\partial t^n}(t) \quad , \quad n \in \{0, 1\}. \tag{4.23}$$

Taking the Fourier transform of equation 4.23 results in

$$\hat{\sigma}(w) = \eta(iw)^n \hat{\varepsilon}(w) \quad , \quad n \in \{0, 1\}, \tag{4.24}$$

which is now a simple multiplication so our Kelvin example 4.2.2 can in the Fourier frequency (w) domain be treated analoguous to the rules in 4.20

$$\hat{\sigma}_{tot}(w) \quad = \quad \eta(iw)^n \hat{\varepsilon}_1(w) + C\varepsilon_2(w) = (\eta(iw)^n + C)\hat{\varepsilon}_{tot}(w) \tag{4.25}$$

Similarly using the Laplace transform instead: Taking the Laplace transform of 4.23 with $n = 1$ results in

$$\tilde{\sigma}(s) = \eta s(\tilde{\varepsilon}(s) - \varepsilon(0)). \tag{4.26}$$

In the case of zero initial conditions one has similar expressions using the Laplace transform as with the Fourier transform:

$$\tilde{\sigma}(s) = \eta s\tilde{\varepsilon}(s), \tag{4.27}$$

which for the Kelvin example 4.2.2 gives

$$\tilde{\sigma}_{tot}(s) \quad = \quad \eta s^n \tilde{\varepsilon}_1(s) + C\varepsilon_2(s) = (\eta s^n + C)\tilde{\varepsilon}_{tot}(s) \tag{4.28}$$

4.2.2 Model examples

Example 4.2.3.

Figure 4.4: Generalized Maxwell model with n branches.

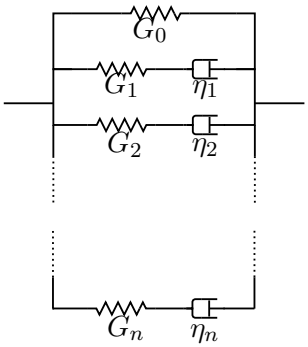

Figure 4.5: A rheological illustration of the generalized Kelvin model with n sections.

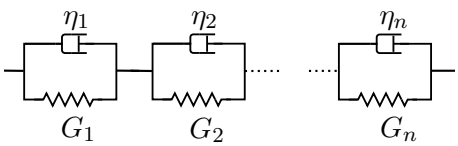

The Burger model is an example of combining Maxwell and Kelvin sections further:

Figure 4.6: A rheological illustration of the Burger model

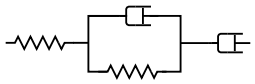

◇

The more branches used equals more parameters used in the model. It is of course preferable to minimize the amount of parameters while maintaining a good fit with the master curves of the material. The generalized models above can fit master curves fairly well quantitatively but qualitatively looks different due to the discrete nature of the branches. See [Xu and Solaimanian, 2009, p. 408-410] for examples of master curve fits of asphalts with generalized models with between 4 and 16 branches.

4.2.3 Huet-Sayegh Model

This section introduces the Huey-Sayegh rheological model as seen in the works [Ministerie van Verkeer en Waterstaat, 2012], [Pronk, 2003] and [Xu and Solaimanian, 2009]. It differs from more standard (generalized) Maxwell and Kelvin models by introducing socalled variable or parabolic dampers which in words best can be described as a mechanical model component inbetween a spring and damper. See also [Andersen, 2002, p. 53] for good comments on fractional derivative models in the context of beam equations on foundations for railtrack modelling. Mathematically the link to the relaxation functions and analogous to Boltzmann convolution integrals as in [Allan F. Bower, 2008, p. 141] in section 4.1 is

$$\sigma(t) = \eta \int_{-\infty}^{t} (\tau - t)^{-\alpha} \frac{\partial \varepsilon}{\partial \tau}(\tau) \mathrm{d}\tau, \tag{4.29}$$

with $\alpha = 1$ for a damper and $\alpha = 0$ for a spring and a variable damper is for $0 < \alpha < 1$.

Figure 4.7: Huet-Sayegh (HS) rheological model.

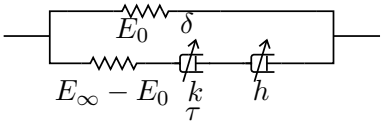

It is important to note that the author has focused on the Huet-Sayegh model for this study since it has been shown in [Ministerie van Verkeer en Waterstaat, 2012], [Pronk, 2003], and [Xu

and Solaimanian, 2009] to be a good model for the complex dynamic modulus of asphalt and their master curves, but there is nothing in the methods used prohibiting adding more branches and sections with more components (variable dampers) to adjust the model.
The HS model consists of two springs and two variable dampers as illustrated in figure 4.7 and is assumed to govern the behaviour of the dynamic modulus as a function of the frequency. Thereby six parameters is initially needed: Two spring constants E_0 and $E_\infty - E_0$. Two viscosities of the dampers η_1 and η_2. Two exponents $0 \leq \alpha_1, \alpha_2 \leq 1$ placing each variable damper in between a pure spring action for the value 0 and a pure damper for the value 1.
Furthermore each damper has a time constant τ_i modelling the influence of temperature θ governed by the equation:

$$\tau_i(\theta) \quad = \quad e^{a_i + b_i\theta + c_i\theta^2} \tag{4.30}$$

The stress to strain relation for a variable damper is:

$$\hat{\sigma}(w) \quad = \quad \frac{\eta}{\tau(\theta)}(iw\tau(\theta))^\alpha \hat{\varepsilon}(w)$$

Following the rules for combining components we get the following expression for the Young's modulus under this model:

$$E(w) \quad = \quad E_0 + \frac{1}{\frac{1}{E_\infty - E_0} + \frac{1}{\frac{\eta_1}{\tau_1(\theta)}(iw\tau_1(\theta))^{\alpha_1}} + \frac{1}{\frac{\eta_2}{\tau_2(\theta)}(iw\tau_2(\theta))^{\alpha_2}}},$$

which is usually rewritten as (and in the litterature the exponents are often designated as $k = \alpha_1$ and $h = \alpha_2$)

$$\begin{aligned} E(w) \quad &= \quad E_0 + \frac{1}{\frac{1}{E_\infty - E_0} + \frac{1}{\frac{\eta_1}{\tau_1(\theta)}(iw\tau_1(\theta))^{\alpha_1}} + \frac{1}{\frac{\eta_2}{\tau_2(\theta)}(iw\tau_2(\theta))^{\alpha_2}}} \\ &= \quad E_0 + \frac{E_\infty - E_0}{1 + \frac{\tau_1(\theta)(E_\infty - E_0)}{\eta_1(iw\tau_1(\theta))^k} + \frac{\tau_2(\theta)(E_\infty - E_0)}{\eta_1(iw\tau_2(\theta))^h}}, \end{aligned}$$

As explained in the work [Ministerie van Verkeer en Waterstaat, 2012] Pronk reduced the number of parameters by setting

$$\tau(\theta) := \tau_1(\theta) = \tau_2(\theta), \tag{4.31}$$

and

$$\delta_2 := \frac{\tau_2(\theta)(E_\infty - E_0)}{\eta_2} = 1, \tag{4.32}$$

and similarly writing

$$\delta := \frac{\tau_1(\theta)(E_\infty - E_0)}{\eta_1}, \tag{4.33}$$

leaving

$$E(w) = E_0 + \frac{E_\infty - E_0}{1 + \delta(iw\tau)^{-k} + (iw\tau)^{-h}}, \tag{4.34}$$

as the governing equation for the complex modulus in the Fourier frequency domain. For now fix $\tau = 1\,\mathrm{s}$. In this text there will not be a comparison of runs across temperatures anyway, but the Time Temperature Superposition should be applicable in an analogous manner in the choice of a Laplace transform since the Fourier and Laplace transforms have similar properties regarding scaling. See [Xu and Solaimanian, 2009] or [Y. Richard Kim, 2009, p. 24] for starting points regarding time temperature superposition.
Similarly for the Laplace complex frequency domain assuming zero initial conditions:

$$E(s) \quad = E_0 + \tfrac{E_\infty - E_0}{1+\delta s^{-k} + s^{-h}}. \tag{4.35}$$

Equation (4.35) is the foundation of the complex frequency modulus implemented in this study in a finite element framework to directly simulate the Huet-Sayegh model instead of approximating master curves with generalized models with several branches in a Prony series - see [Xu and Solaimanian, 2009] or [Allan F. Bower, 2008]. Plotted below are the master curves for the Fourier and Laplace setups:

Figure 4.8: Master Curve and Phase Angle in MPa vs. ω and material as Layer #1 in table 5.5

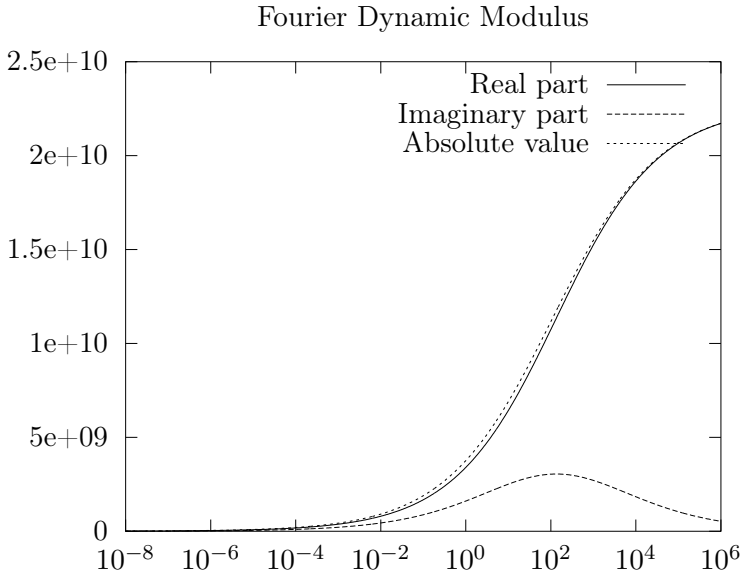

Figure 4.9: Laplace Master Curve and Laplace Phase Angle MPa vs. ω for $c = 12.053$, $s = c + i\omega$ and material as Layer #1 in table 5.5

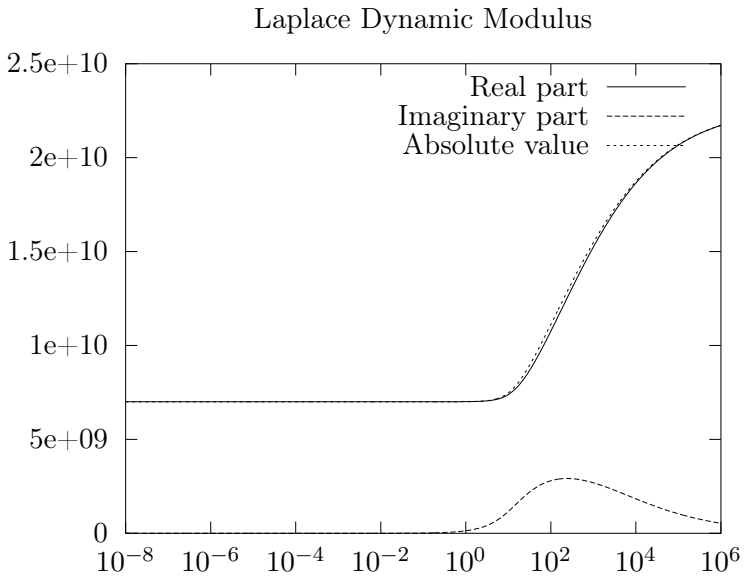

Now for the simulation technique used.

Chapter 5

Finite Element Method

This section describes the use of the Finite Element Method (FEM) for gaining insight into the relevant dynamics of a road structure and needed in the thesis to develop better models for road behaviour under loading.
FEM is a numerical method for approximating solutions to ordinary and partial differential equations. The basic principle of the method is discretization of the domain in which a solution is sought and the projection of the true solution onto a finite-dimensional subspace of basis functions instead of the often infinite dimensional space needed to describe the exact solution. The discretization procedure is called meshing and the resulting set of nodes and volume elements is called a mesh.
The mathematical setting for this is primarily functional analysis and the main results supporting the approach are the convergence results which, in words, promises convergence towards the true result with refined discretization of the domain or use of higher-order basis functions. See [G.R.Liu and Trung, 2010] as a starting point for such considerations.
In practice this means that we can get arbitrarily precise solutions but at the cost of increased computational time. There are of course a plethora of great textbooks on Finite Element Methods, its variants and related techniques and it is not a goal of the author here to give a course which is better left to books and ressources such as [COMSOL, 2011] and [Fish and Belytschko, 2007].

5.1 The Choice of FEM

The reasons for the use of FEM by the author is the wide variety of situations it can be adapted to. When working with partial differential equations exact solutions are mostly known only for very simple geometries, halfspaces, simple source functions and simple constitutive equations - e.g. linear elasticity.
The situation of interest for the study of road structures here can be described as a geometry consisting of a halfspace in 3D with different layers of material properties as we go deeper - asphalt, a different asphalt, gravel, soil, rock, magma, molten iron however that is probably too deep even for an in-depth study...

One could hope that a halfspace with parallel layers would be simple enough to allow for exact solutions or clever approximations. However it is not known to the author that solutions exists to satisfactorily cover the situations relevant for this study, such as:

- Moving Loads.
- Varying Loads.
- Visco-elastic layers (e.g. generalized Maxwell models but also more general Huet-Sayegh-like models).
- Finite size of the road in the transverse direction meaning boundaries with soil or other materials.
- Asymmetry: Measurements being done closer to one side of the road.
- Physical real situations during measurements: Driving across bridges and the like.

This text will not fully cover all of the above points, however these are some of the points to keep in mind as possible future work and the framework used for the study should preferably be extendable to give insights into the significance of these variations.

5.2 Simulation Techniques

This section clarifies the setup used in the FEM in this study.
Two methods will be used: A non-standard approach combining FEM in COMSOL® Multiphysics[1] with the Laplace transform to run the actual simulation in the complex frequency domain and a more standard time-solver as built into COMSOL Multiphysics already.
A natural question arising in computational topics such as this is computation time. The multitude of possible different settings, meshings, required precisions and more makes a thorough comparison of computational times quite an undertaking, especially as the tools are still being calibrated.
Most of the work was done on a 2.2 GHz with 8 Gb Asus G74 Laptop from 2011, with simulations taking anywhere from minutes for toy problems to a couple of hours for larger runs. Hence there is ample room for improvement with respect to computational capacity and setup. The computation time topic is mostly neglected from here though. First a description of the geometry.

5.3 Geometry

The same basic geometry will be used in all the FEM simulations presented, both time domain and Laplace method, and used for this study. Specific lengths will change.

[1] Registered trademarks.

Example 5.3.1 (Illustration of choices regarding infinite elements.)**.**

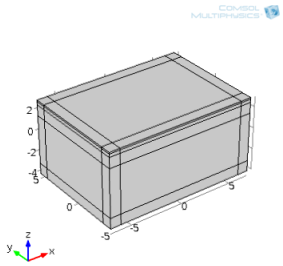

Figure 5.1: #1 No infinite elements.

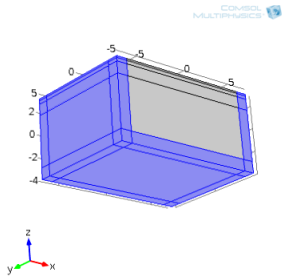

Figure 5.2: #2 Infinite elements lengthwise and downwards.

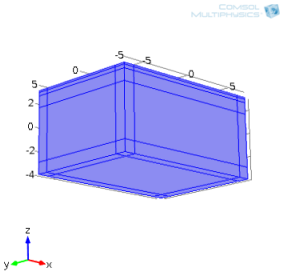

Figure 5.3: #3 Infinite elements lengthwise, width-wise and downwards.

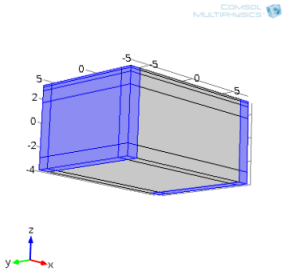

Figure 5.4: #4 Infinite elements lengthwise only.

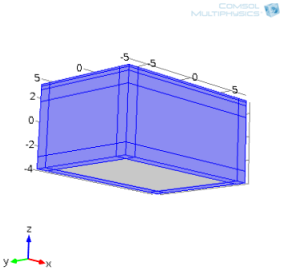

Figure 5.5: #4 Infinite elements lengthwise and widthwise.

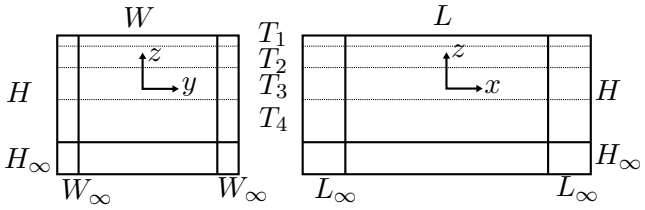

Figure 5.7: Lengths (H,W,L) and thicknesses (T). Four layers with interfaces illustrated with dashed lines. Layers are enumerated from the top down.

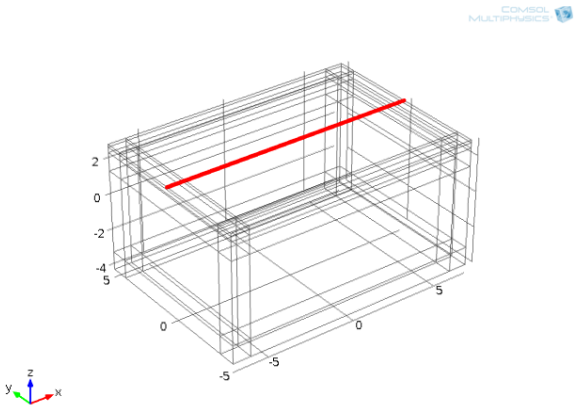

Figure 5.6: 401 points along the top of the structure data is extracted from for processing.

Table 5.1: Table of names used for various geometry lengths - see also figure 5.7.

Symbol	Description
L	Length in COMSOL along x of volume of interest.
L_∞	Length in COMSOL along x of extra volume used for infinite elements.
W	Width in COMSOL along y.
W_∞	Width in COMSOL along y of extra volume used for infinite elements.
H	Depth in COMSOL along z.
H_∞	Depth in COMSOL along z of extra volume used for infinite elements.
T_1	Thickness of first layer from the top.
T_2	Thickness of second layer.
T_3	Thickness of third layer.
T_4 [2]	Thickness of fourth layer.

5.3.1 Meshing

The meshing is always important in finite element methods. One wants a good enough refinement to get a sufficiently good approximation. The meshes used in this study has mostly been similar to that illustrated in figure 5.8. More precise meshing information can be found in the appended FEM-reports on the supplied USB-disc, as a full description is a little cumbersome so a picture tells a thousand words.

[2]Not referenced in the text, seeing as when using infinite elements the thickness of the bottom layer is in that sense infinite (or very large at least) and the total thickness of the boxis already stated.

Figure 5.8: An illustration of a representative mesh used. A quadrilateral mesh with extra refinement along $y = 0$ where the moving loads move and finer refinement closer to the top. The mesh consists of layered boxes with an extra "shell" of boxes around for enabling infinite elements as will be described in short now.

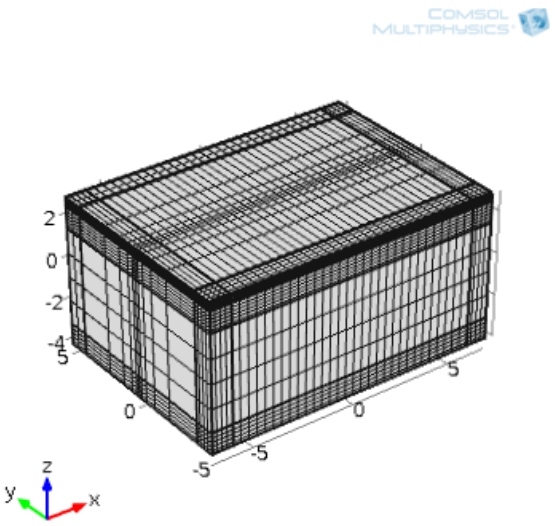

5.3.2 Infinite Elements

In FEM there are techniques to deal with unbounded domains. The problem with truncating and modelling a finite block as an approximation to an infinite domain problem is that one changes the boundary conditions and can get artifacts such as reflections from the introduced boundaries. Simply modelling a bigger slab might result in an untractably large problem with an unwieldy amount of elements/nodes.

Please refer to figure 5.5 to see the sections marked for use of infinite element highlighted.
In COMSOL 4.2 infinite elements for use in stationary and time dependant structural mechanics problems were introduced to the software. The mathematical workings of how infinite elements or other techniques for handling boundary issues such as unwanted reflections, such as Perfectly Matched Layers (PML), will not be treated here, as the author chose to see if infinite elements would be applicable.
See the appended USB-disc for an illustration on how the COMSOL equations were modified to accommodate the Laplace method together with infinite elements (Alternatively see the COMSOL reports.) Illustrated now is the difference between the use of infinite elements or not. The author apologizes for skipping forward in the text and using figure 5.9 twice. Also note a small overload of notation as $\mathbf{u}$ is now refering to the approximate solutions acquired from FEM and not the true solutions.

Figure 5.9: Example of a FWD-like simulation with and without infinite elements downwards respectively. Used are the values of run #5-FWD-S in table 5.6 for loads and material and FEM settings #4 of 5.4. Graphed are the deflections experience by fixed points X_n indexed $51, 101, 151, 201$ out of 401 datapoints seen in figure 5.6 so with the settings chosen $\{X_n\} = \{-5.25, -3.5, -1.75, 0\}$
It clearly shows how a too shallow modelling depth influences the results through reflections. It should also be noted that the width of the modelled slab is important in letting the stress cone out properly.

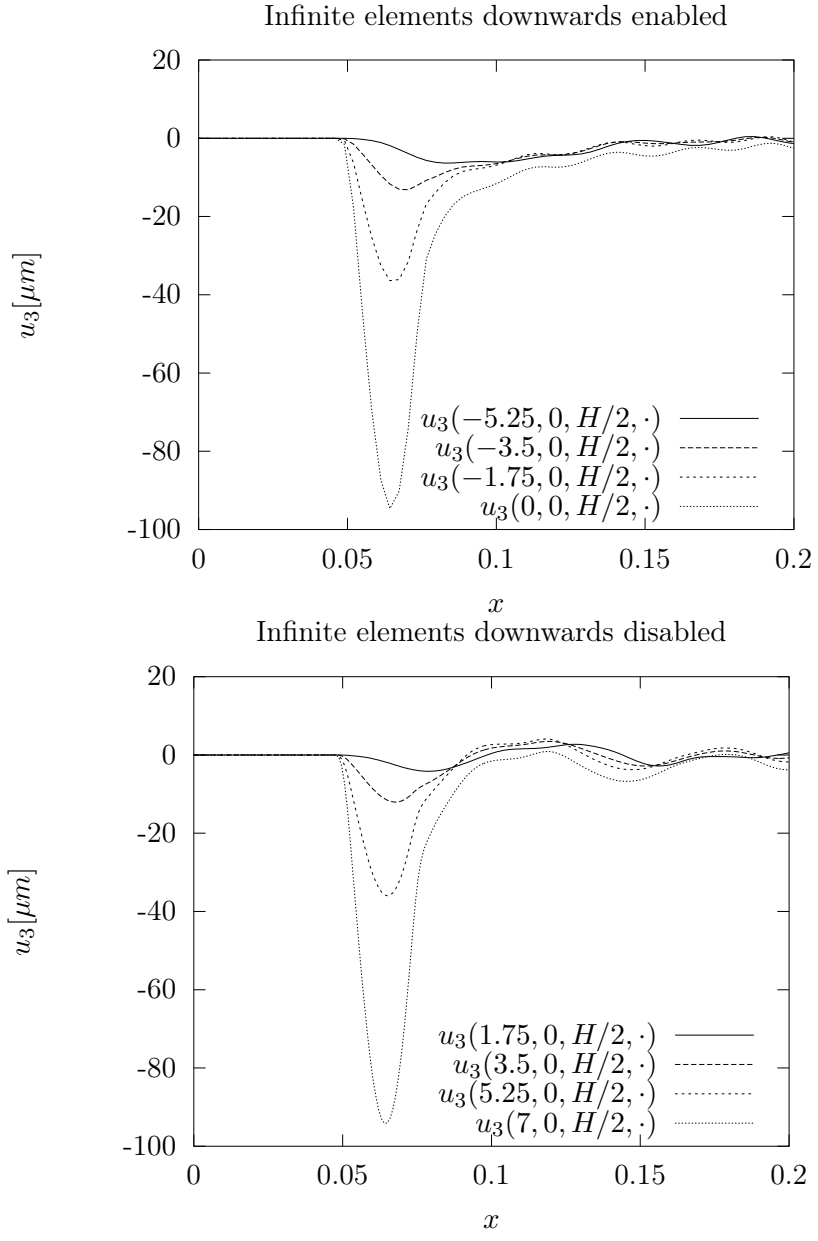

It should be noted that it is unrealistic to assume an infinite space downwards with the same E-module. There will be a bedrock or simply increasing moduli with depths and a simple linearly increasing E-module coupled with the infinite domain might be an even better option, and is approachable to try out, which will be done in the near future.

5.4 Boundary Conditions and Load Assumptions

The load conditions of the structure investigated here are imposed upon the top of the structure as seen in figure 2.4. The load functions described in this section is therefore described as functions of (x, y, t) in the time domain or of (x, y, s) in the Laplace complex frequency domain. The outer boundaries of the geometry except for the top and sides are held fixed in the simulations. It is an open question, for the author at least, which boundary conditions best describes the soil-to-road interaction at the sides of the structure.

5.4.1 Approximating Tire Pressures

A tire exerts a pressure not well represented with a rectangular pulse. A rectangular pulse is however introduced and used for validation purposes as for instance ViscoRoute to be introduced later will use rectangular pulses.
The company supervisor of the author for this project, Jørgen Krarup, has in his Ph.D. thesis, [Jørgen Krarup, 1994] measured the pressure distribution under a moving tire.
The distribution choices below are not perfect fits, but they have the properties of being relatively simple expressions and easily transformed for the Laplace method.
As seen in figure 5.10 a realistic tire footprint is much more complicated and tire-dependant, with further complexities from the fact of a dual wheel-set.

Figure 5.10: Real measured tire pressures from the Ph.D. thesis of company supervisor Jørgen Krarup. These variations will not be attempted approximated for the sake of this study. The tire pressure shown here is designated "Dual Wheel: 2 x 12 R 22.5" in [Jørgen Krarup, 1994, p. 34-35]

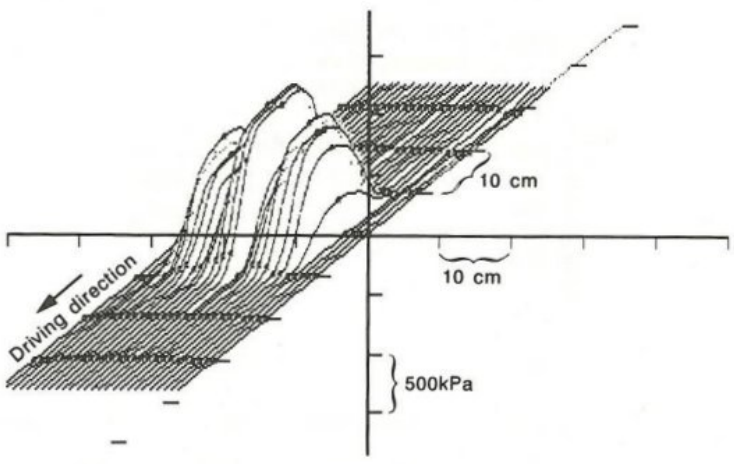

Figure 3.6 Distribution of measured vertical contact stress. Axleload is 80 kN, inflation is 700 kPa, and speed 20 km per hour. (Values are mean of the signals from three CSC's).

Let x_0 be position of the trailing edge of the tire at time $t = t_0$ Let $x_0 + L_W$ be the position of the leading edge of the tire at time $t = t_0$

The function $f_S : \mathbb{R} \to \mathbb{R}_0^+$ and $f_S : \mathbb{R} \to \mathbb{R}_0^+$ denote the pressure distribution across the tire length-wise in the x-direction, where the subscripts stand for sinusoidal and rectangular respectively. The sinusoidal pressure profile is set to:

$$f_S(x; L_W) = \begin{cases} 0 & , \quad x < 0 \\ \frac{F_T}{C_S(L_W)} \sin(\frac{\pi x}{L_W}) & , \quad 0 \leq x \leq L_W \\ 0 & , \quad x > L_W \end{cases} \tag{5.1}$$

where, for normalizing the total force and making F_T denote the total force

$$C_S(L_W) := \int_0^{L_W} \sin\left(\frac{\pi x}{L_W}\right) \mathrm{d}x = \frac{L_W}{\pi} \int_0^{\pi} \sin(y) \mathrm{d}y = \frac{2L_W}{\pi}. \tag{5.2}$$

The rectangular pressure profile is set to:

$$f_R(x; L_W) := \frac{F_T}{L_W} \mathbb{1}_{[0, L_W]}(x) \tag{5.3}$$

With respect to the width direction of the tire, writing W_W for the wheel width itself, an indicator function is simply used. So set

$$g(y; W_W) := \frac{1}{W_W} \mathbb{1}_{[-\frac{W_W}{2}, \frac{W_W}{2}]}(y) \tag{5.4}$$

Assuming the tire moves at a constant velocity v in the positive x-direction

$$\begin{aligned} Q_S(x, y, t; L_W, W_W) &= f_S((x - x_0) - v(t - t_0); L_W) g(y; W_W) \\ Q_R(x, y, t; L_W, W_W) &= f_R((x - x_0) - v(t - t_0); L_W) g(y; W_W). \end{aligned} \tag{5.5}$$

Since the pressure distributions in equation (5.1) and (5.3) are supported on the interval $[0, L_W]$ a point $x \geq x_0 + L_W$ is pressured upon in the time interval $[t_1, t_2]$ as described by:

$$\begin{aligned} x - x_0 - v(t - t_0) \geq 0 &\Rightarrow \frac{x - x_0}{v} + t_0 \geq t \\ x - x_0 - v(t - t_0) \leq L_W &\Rightarrow \frac{x - x_0 - L_W}{v} + t_0 \geq t \end{aligned} \tag{5.6}$$

so $[t_1, t_2] = [\frac{x - x_0 - L_W}{v} + t_0, \frac{x - x_0}{v} + t_0]$

Since $t \geq 0$:

To avoid having to input initial conditions it is preferable to make sure there is no loading at time $t = 0$. The author chose to start the above pulse at a x_0 at time $t_0 > 0$ and define a ramp function R, starting at a point r_1:

$$R(x; r_1, r_2) = \begin{cases} 0 & , \quad x < r_1 \\ \frac{x - r_1}{r_2 - r_1} & , \quad r_1 \leq x \leq r_2 \\ 1 & , \quad x > r_2 \end{cases} \tag{5.7}$$

By using a loading defined as follows:

$$P_R(x,y,t;L_W,W_W,r_1,r_2,x_0) = R(x,r_1,r_2)Q_R(x,y,t;L_W,W_W) \quad , \quad r_1 > x_0 + L_W$$
$$P_S(x,y,t;L_W,W_W,r_1,r_2,x_0) = R(x,r_1,r_2)Q_S(x,y,t;L_W,W_W) \quad , \quad r_1 > x_0 + L_W, \qquad (5.8)$$

the loading is zero for all x for time $t = 0$ and as the load moves it "slides onto" the ramp function and ramps up to the full loading after the point $x = r_2 + L_W$.
It is then hoped that the dynamics from this ramping up will die out sufficiently quickly and be small enough as to not interfere much with the later interval in the simulation $\approx [\frac{T}{3}, \frac{2T}{3}]$ which is from where the simulated data is sampled.
The following calculations are done to get the Laplace transformations with respect to time of the load function as needed in equation (4.7). Note the complex frequency is written $s = c + iw$.

$$\begin{aligned}
&[\mathcal{L}P_S](x,y,s;L_W,W_W,r_1,r_2,x_0) = \hat{P}_S(x,y,s;L_W,W_W,r_1,r_2,x_0) \\
&= \int_0^\infty e^{-st} P_S(x,y,t;L_W,W_W,r_1,r_2,x_0)\mathrm{d}t \\
&= R(x,r_1,r_2)g(y;W_W)\int_{t_1(x)}^{t_2(x)} e^{-st} f_S((x-x_0)-v(t-t_0);L_W)\mathrm{d}t \\
&= \frac{\pi}{2L_W}R(x,r_1,r_2)g(y;W_W)\int_{t_1(x)}^{t_2(x)} e^{-(c+iw)t}\frac{e^{i\frac{\pi}{L_W}((x-x_0)-v(t-t_0))} - e^{-i\frac{\pi}{L_W}((x-x_0)-v(t-t_0))}}{2i} \\
&= \frac{\pi}{2L_W}R(x,r_1,r_2)g(y;W_W)\int_{t_1(x)}^{t_2(x)} \frac{e^{[-c-iw-i\frac{\pi}{L_W}v]t+i\frac{\pi}{L_W}vt_0+i\frac{\pi}{L_W}(x-x_0)} - e^{[-c-iw+i\frac{\pi}{L_W}v]t-i\frac{\pi}{L_W}vt_0-i\frac{\pi}{L_W}(x-x_0)}}{2i} \\
&= \frac{\pi R(x,r_1,r_2)g(y;W_W)}{4L_W i}\left[\frac{e^{[-c-iw-i\frac{\pi}{L_W}v]t+i\frac{\pi}{L_W}vt_0+i\frac{\pi}{L_W}(x-x_0)}}{[-c-iw-i\frac{\pi}{L_W}v]} - \frac{e^{[-c-iw+i\frac{\pi}{L_W}v]t-i\frac{\pi}{L_W}vt_0-i\frac{\pi}{L_W}(x-x_0)}}{[-c-iw+i\frac{\pi}{L_W}v]}\right]_{t_1(x)}^{t_2(x)}
\end{aligned} \qquad (5.9)$$

with the rectangular loading

$$\begin{aligned}
[\mathcal{L}P_R](x,y,s:L_W,W_W,r_1,r_2,x_0) &= \hat{P}_R(x,y,s;L_W,W,r_1,r_2,x_0) \\
&= \int_0^\infty e^{-st} P_R(x,y,t;L_W,W_W,r_1,r_2,x_0)\mathrm{d}t \\
&= R(x,r_1,r_2)g(y;W_W)\int_{t_1(x)}^{t_2(x)} e^{-st}\mathrm{d}t \\
&= R(x,r_1,r_2)g(y;W_W)\left[\frac{e^{[-c-iw]t}}{-c-iw}\right]_{t_1(x)}^{t_2(x)} \\
&= R(x,r_1,r_2)g(y;W_W)\left[\frac{e^{[-c-iw]t_2}}{-c-iw} - \frac{e^{[-c-iw]t_1}}{-c-iw}\right]
\end{aligned} \qquad (5.10)$$

For added realism a twin wheel set should be considered since the TSD actually employs these setup with a special axis to allow measurements to be done between the wheel and close to the center of the load.
In the above choice of tire pressures, incorporating twin wheels would amount to superimposing two $\hat{P}_R$ or $\hat{P}_S$ translated in the y-direction. The following is used to approximately model a twin wheel set with the footprint of each tire being 0.3 m wide leaving a 0.1 m space between them

$$\begin{aligned}&\hat{P}_{2\times S}(x, y, s; L_W, W, r_1, r_2, x_0)\\ &\quad := \hat{P}_S(x, y - 0.2, s; L_W, 0.3, r_1, r_2, x_0) + \hat{P}_S(x, y + 0.2, s; L_W, 0.3, r_1, r_2, x_0). \qquad (5.11)\end{aligned}$$

The choices for this text and study is hence done for the sake of simplicity but motivated by not having an unrealistic sharp sudden loading in the x-direction of movement. There is however a lot of flexibility in the choice of loading shapes and footprints. Furthermore the bassin generated by the wheel set on both sides of the truck should be considered if it turns out the bassins are significant on the order of the length between the tire set. Possibly even the bassins stemming from the tractor should be incorporated. Doing that in the case of unbounded domains and assuming similar loads on both sets, could be done by simply translation and superposition.
In other situations, finite widths and loadings close to boundaries require a remeshing to also resolve details around the other wheelset.

5.4.2 FWD Load Assumptions

A realistic FWD pulse can vary depending on the settings of the apparatus. Without being an expert on the operation of such it is the understanding of the author that the weight, size of base plate and rubber impact plates used to distribute the load into the right duration and uniformity all contribute to the results.
Leaning against figure 2 and 3 in [Brent Rauhut Engineering, Inc, 1997] assumed here is a 25 ms pulse length. A 42 kN peak load is used there, here 50 kN was used. See also figure 5.11 for a measured FWD load pulse (and reponses)[3].

[3]Note also the fairly large swing back above 0, which is interesting to see if it can be modelled. It should depend very much on the downwards boundary condition choice as hinted at in figure 5.9

Figure 5.11: A plot scanned from the thesis of the company supervisor Jørgen Krarups Ph.D. thesis, showing the pulse record in a FWD load cell and also the measured responses from a FWD drop. For this section what is interesting is the shape of the FWD load which is attempted formed as a sine lobe in the design.

Figure 4.1 Measured vertical soil stress time history during one second and one drop of the FWD load.

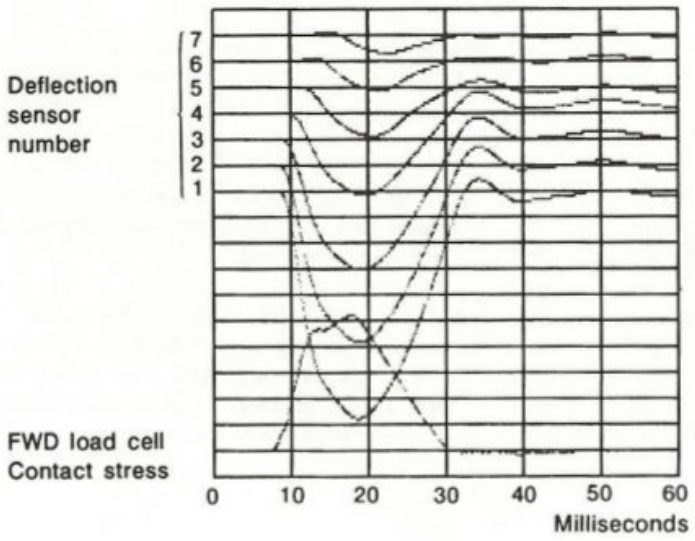

*Figure 4.2 Time history plot from FWD output (measured date: 90.11.05). The y-scale for deflections is 50 m * 10^6 per division. The y-scale for the load contact stress is 100 kPa per division.*

In the Laplace method coming up in section 5.5 the Laplace transform of appendix .2 of the load with respect to time is needed, so the load should preferably be approximated with functions which are easily and explicitly transformable.
The pulse shape with respect to time shown in figure 5.11 is assumed to be simply a lobe of a sine curve. Seemingly the consensus is that FWD loads are described by the peak force denoted here F_P. The temporal distributions used are described with the following functions $h_S : \mathbb{R}_0^+ \to \mathbb{R}$ and $h_R : \mathbb{R}_0^+ \to \mathbb{R}$ where the subscripts denote "Rectangular" and "Sinusoidal" respectively.

$$
\begin{aligned}
h_R(t; t_1, t_2, F_P) &:= F_P \mathbb{1}_{[t_1,t_2]}(t) \\
h_S(t; t_1, t_2, F_P) &:= \begin{cases} 0 & , \quad t < t_1 \\ F_P \sin\left(\frac{\pi(t-t_1)}{t_2-t_1}\right) & , \quad t_1 \leq t \leq t_2 \\ 0 & , \quad t > t_2 \end{cases}
\end{aligned} \tag{5.12}
$$

Assumed here is also that the plate loads the road uniformly across the plate so each points underneath experiences the same load profile in time. The plate is assumed round so define $h_1 : \mathbb{R}^2 \to \{0, 1\}$ as

$$h_1(x,y;r_0) = \frac{1}{\pi r_0^2}\begin{cases} 1 & , \quad \sqrt{x^2+y^2} \leq r_0 \\ 0 & , \quad \sqrt{x^2+y^2} > r_0 \end{cases} \tag{5.13}$$

The pulses $P_{FWD,S} : \mathbb{R}^2 \times \mathbb{R}_0^+ \to \mathbb{R}$ and $P_{FWD,S} : \mathbb{R}^2 \times \mathbb{R}_0^+ \to \mathbb{R}$ used for the FWD simulations are

$$\begin{aligned} P_{FWD,S}(x,y,t;t_1,t_2,r_0,F_P) &:= h_S(t;t_1,t_2,F_P)h_1(x,y;r_0) \\ P_{FWD,R}(x,y,t;t_1,t_2,r_0,F_P) &:= h_R(t;t_1,t_2,F_P)h_1(x,y;r_0) \end{aligned} \tag{5.14}$$

The Laplace transform of $P_{FWD,S}$ is calculated similarly to equation (5.9) using the substitution $t \mapsto \tau$ defined by:

$$\tau := \frac{(t-t_1)}{t_2-t_1} \Rightarrow \begin{cases} \mathrm{d}t = (t_2-t_1)\mathrm{d}\tau \\ \tau_1 = \frac{(t_1-t_1)}{t_2-t_1} = 0 \\ \tau_2 = \frac{(t_2-t_1)}{t_2-t_1} = 1 \\ t = (t_2-t_1)\tau + t_1 \end{cases} \tag{5.15}$$

$$\begin{aligned} &[\mathcal{L}P_{FWD,S}](x,y,s;t_1,t_2,r_0,F_P) = \hat{P}_{FWD,S}(x,y,s;t_1,t_2,r_0,F_P) \\ &= h_R(x,y;r_0)\int_0^\infty e^{-st}h_2(t;t_1,t_2,F_P)\mathrm{d}t \\ &= h_R(x,y;r_0)\int_{t_1}^{t_2} e^{-st}\sin\left(\frac{\pi(t-t_1)}{t_2-t_1}\right)\mathrm{d}t \\ &= h_R(x,y;r_0)(t_2-t_1)e^{-st_1}\int_0^1 e^{-s(t_2-t_1)\tau}\sin(\pi\tau)\,\mathrm{d}\tau \\ &= h_R(x,y;r_0)(t_2-t_1)e^{-(c+iw)t_1}\int_0^1 \frac{e^{-(c+iw)(t_2-t_1)\tau+i\pi\tau} - e^{-(c+iw)(t_2-t_1)\tau-i\pi\tau}}{2i}\mathrm{d}\tau \\ &= h_R(x,y;r_0)\frac{(t_2-t_1)e^{-(c+iw)t_1}}{2i}\left[\frac{e^{[-(c+iw)(t_2-t_1)+i\pi]\tau}}{-(c+iw)(t_2-t_1)+i\pi} - \frac{e^{[-(c+iw)(t_2-t_1)-i\pi]\tau}}{-(c+iw)(t_2-t_1)-i\pi}\right]_0^1 \end{aligned} \tag{5.16}$$

By using the Laplace transform of an indicator function as in example 7 it follows for the rectangular pulse:

$$\begin{aligned} [\mathcal{L}P_{FWD,R}](x,y,s;t_1,t_2,r_0,F_P) &= \hat{P}_{FWD,R}(x,y,s;t_1,t_2,r_0,F_P) \\ &= h_R(x,y;r_0)\frac{e^{-st_1}-e^{-st_2}}{s} \end{aligned} \tag{5.17}$$

Expressions (5.16) and (5.16) will be used for the Laplace transformed surface tractions as required for equations (4.7) cases where a sinusoidal pulse or rectangular pulse (temporally) are required.

5.5 Laplace Transformed FEM

The idea with the approach sought in this section is to use the properties of the Laplace transform to be able to write up rheological models including variable dampers such as the Huet-Sayegh model easily in the complex frequency domain. Then do the FEM simulations on the transformed equations and invert the transform. This inversion is documented in Appendix .2.2, and the Octave scripts[4] are included on an USB-disc as mentioned in Appendix .4. See [Eaton et al., 2008] for Octave info. The forward transform is done analytically however the inversion is done numerically which requires some care. The work builds strongly upon [Zamorano and Campos, 2007] and [Xu and Solaimanian, 2009], and a Lanczos data window was used. To make the reader familiar with the shown outputs as to better concentrate on the actual results later here follows few comments on the output of the method and the type of plots used for concluding later.

5.5.1 Output

First a few examples from a simulation using the settings of table 5.4 and 5.5 (The exact settings are not so important right now as it is just an example for illustration purposes.):

[4]Or alternatively MATLAB(TM), The MathWorks Inc.

Example 5.5.1 (Deflections of a point over time.)**.**

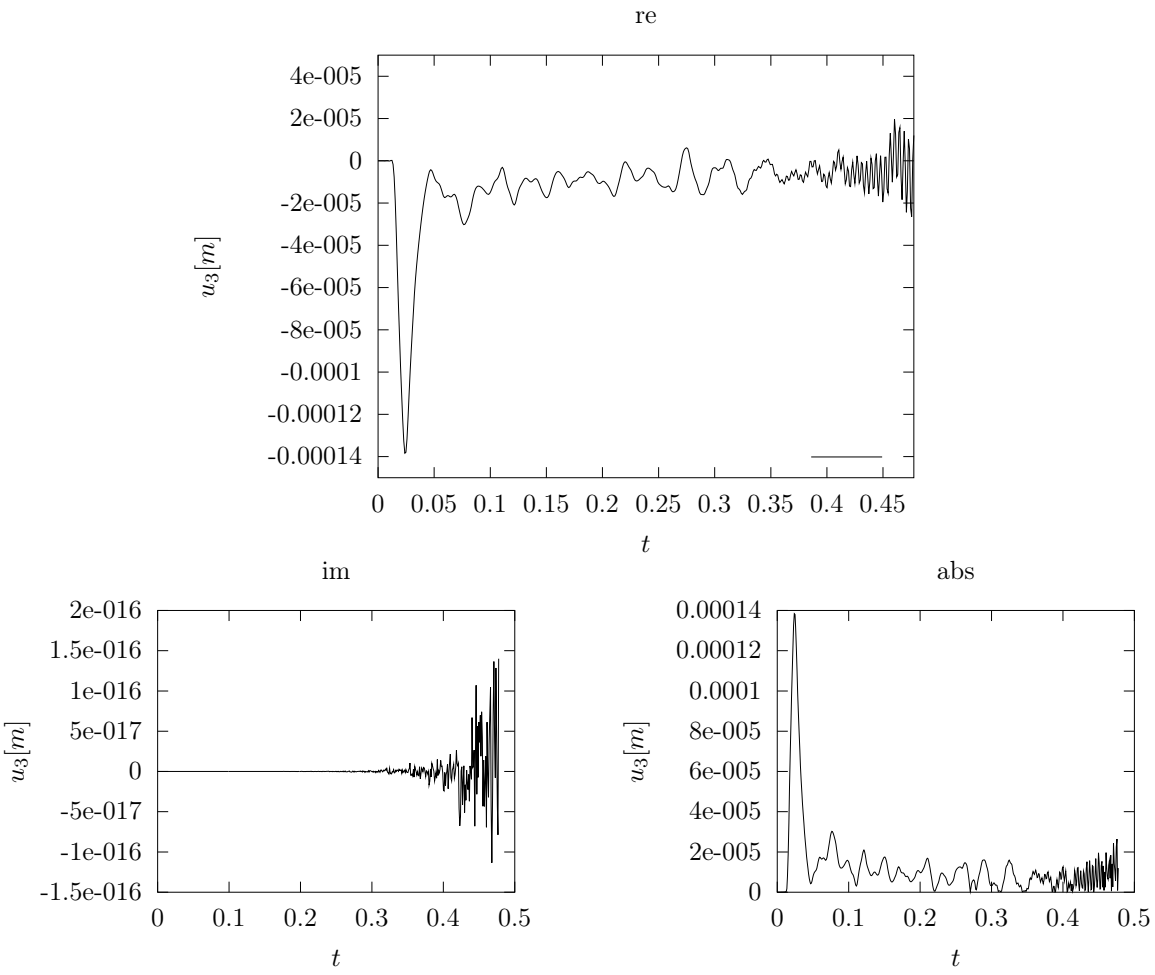

Figure 5.12: Real part, imaginary part and absolute value of the Laplace solution for the run #1 setting of table (5.3) for $(x, y, z, t) = (0, 0, \frac{H}{2}, \cdot)$, i.e. directly under the pulse-like load. As mentioned in the text below, before interpreting on the exact oscillations it should be considered that some are results of meshing and in parts from the Laplace method producing oscillations towards the end

The imaginary part shown on the bottom left of figure 5.12 is satisfyingly small seeing the physical solution being approximated of course is real valued.
It is important to note that the oscillating and diverging nature of the Laplace approximations are a natural aliasing consequence of the discretization of the transform. This behaviour towards the end of the simulations restricts the interval in which the approximation some. Also the exact oscillations should not be over-interpreted as it will be dependant on the meshing used, and hopefully minimized in later applications backed by more computing power for better discretizations.

◇

5.5.2 Spectra

Example 5.5.2 (Spectrum of the deflections at a point)**.** The spectrum graphs in figure 5.13 and 5.14 are used to evaluate whether the truncation is done at a high enough cutoff such that the spectrum and thereby influence of the leftout frequencies are adequately small. In principle one cannot know if there are effects taking place at a higher frequency, but it is assumed from considering the origin of the physical problem that it is not the case.
Alternatively the viewpoint that it is simply a modelling choice could be taken. By not including the high frequency response noise[5] is smoothed out. It could also be argued that the spectrum should be looked at over the whole geometry or an average thereof as in principle effects could be taking place at other frequencies elsewhere.
However the point chosen for figure 5.14 is directly under the FWD-load and it seems reasonable to assume that is the point where most is going on.

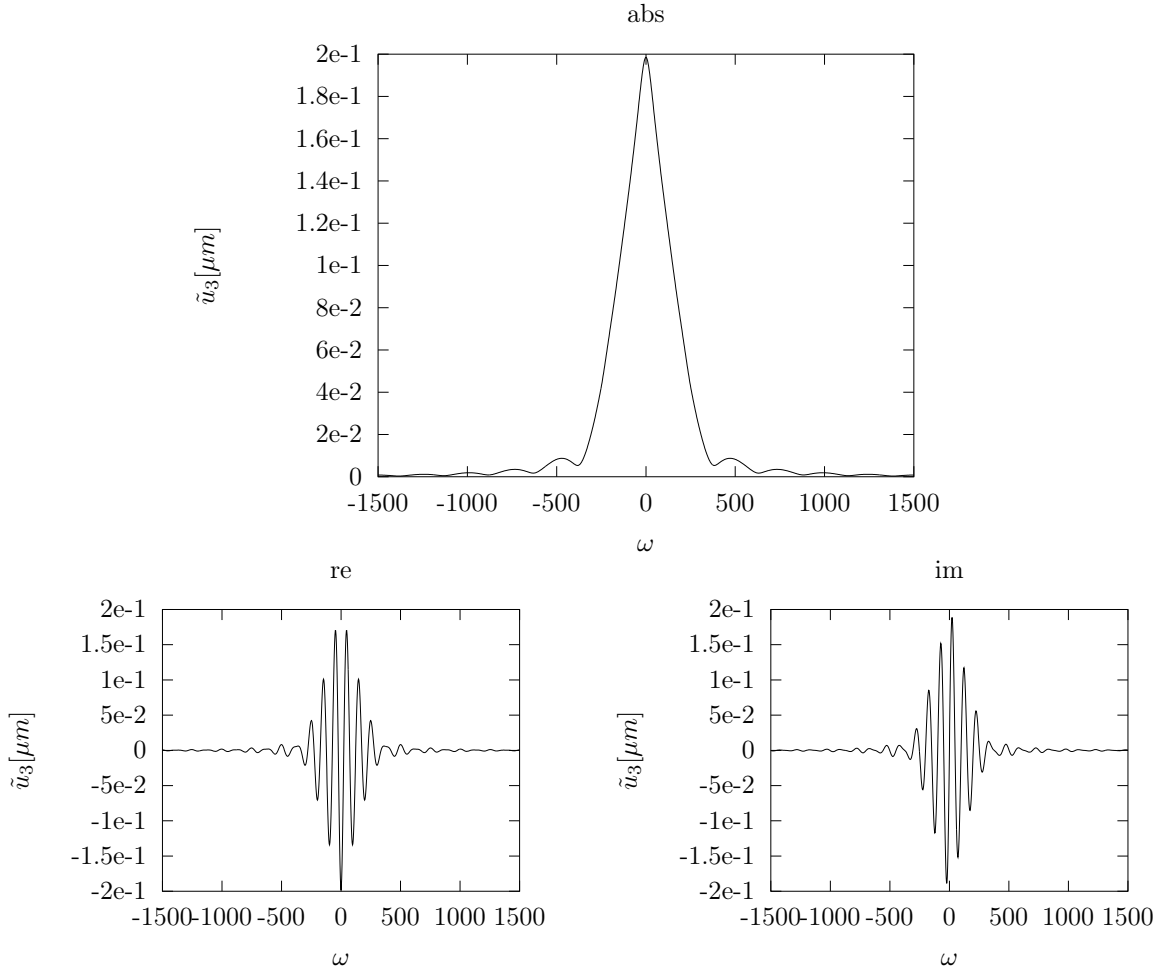

Figure 5.13: Examples of Real, Imaginary and Absolute values of the solution in the Laplace domain, $\tilde{u}$ for $\tilde{u}(x, y, z, w) = (0, 0, \frac{H}{2}, \cdot)$ for a FWD-like loading where the ω-axis is the imaginary part of the complex frequency $s = c + i\omega$.

[5]Noise from meshing, discretization errors etc.

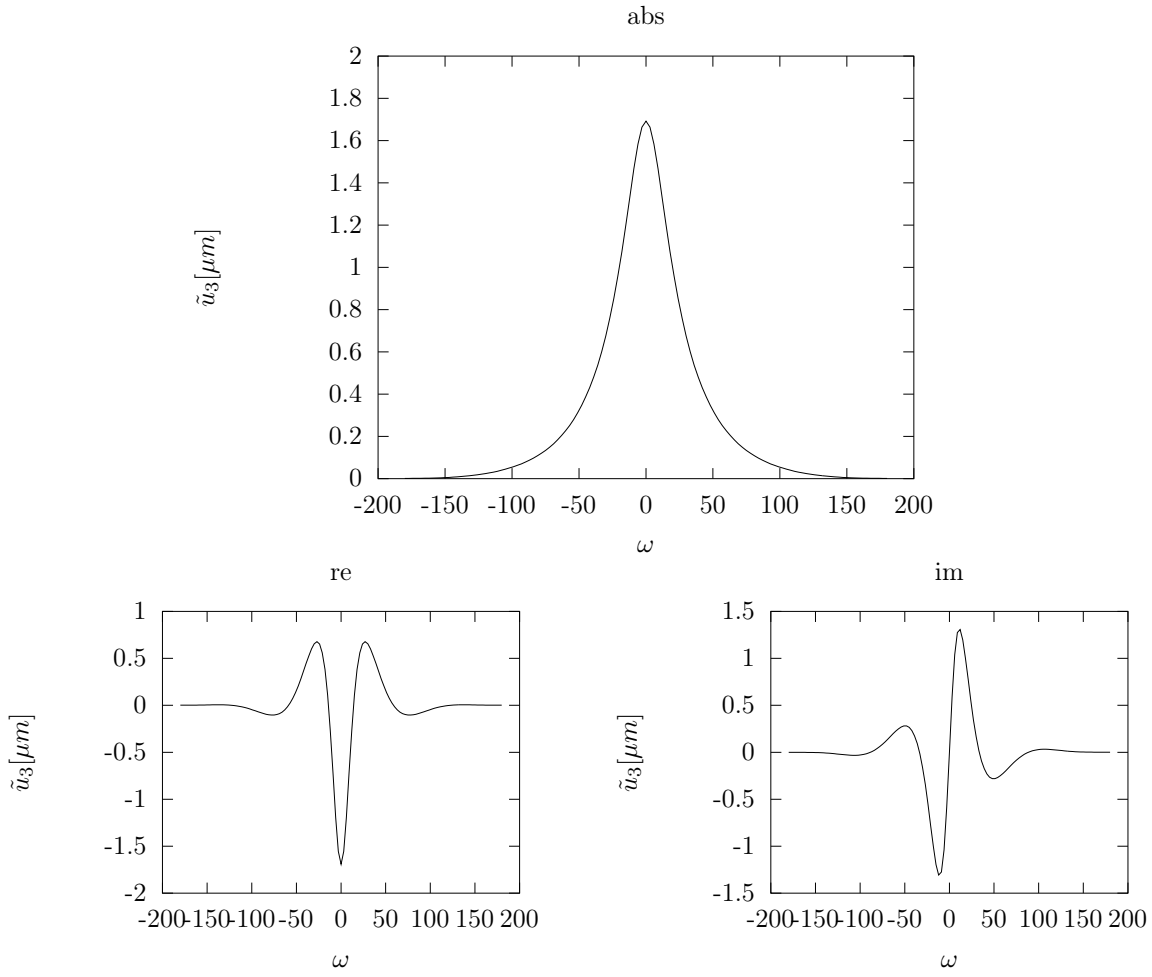

Figure 5.14: Examples of Real, Imaginary and Absolute values of the spectrum for $(x, y, z, w) = (0, 0, \frac{H}{2}, \cdot)$ for a TSD-pulse like loading where the ω-axis is the imaginary part of the complex frequency $s = c + i\omega$.

As the comments in section .2.2 suggest only the results for positive w was simulated as the real and imaginary part should be respectively even and odd stemming from the physical problem being real-valued, and the graphs reflect this setup.
It should also be noted that when doing FWD-like simulations one needs a much broader range of frequencies modelled than in the TSD-situation

◇

5.5.3 Plotting Simulated Data

A few comments on moving load outputs: The surface in figure (5.15) graphing the vertical displacement u_3 with the length-wise position x along one axis and time t along the other shows the load moving along the road and how the bassin looks at the top of the structure along the line $y = 0$.

Figure 5.15: Example plot of the vertical deflection $u_3(\cdot, 0, \frac{H}{2}, \cdot)$. The ramping up of the load is visible towards the front of the image (earlier time) at the starting point further to the left in the negative x-direction.

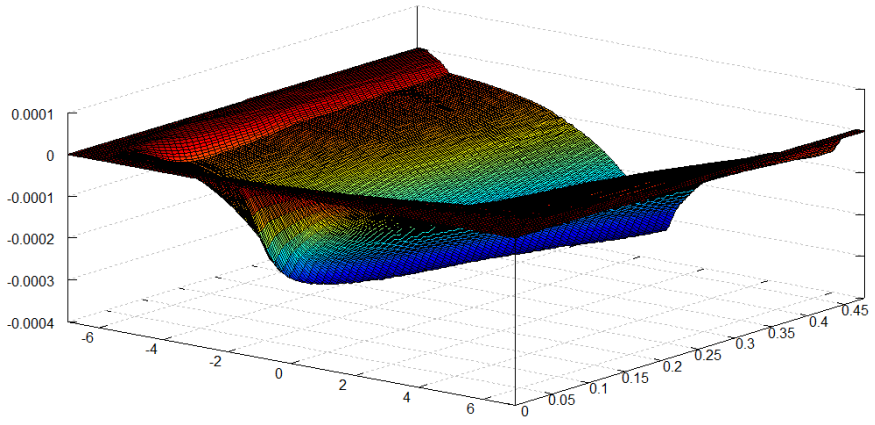

This data could be reformated into an X-frame moving along with the load centered, $X = (x - (x_0 + \frac{L}{2}) - v(t - t_0)$ and the following plots shows the bassins along the X-axis, $y = 0$, for different fixed times, again on the top of the structure ($z = \frac{H}{2}$). See figure 5.16

Figure 5.16: Plots of bassins at various times as seen from the X-frame of the moving load. Disregard the artefacts of the infinite elements in the sides. They are taken from the time interval [0,T] resampled to 1001 times and plotted here are bassins with indices 550 to 700 in increments of 10, showing little variation. The "X"s mark the length of the load.

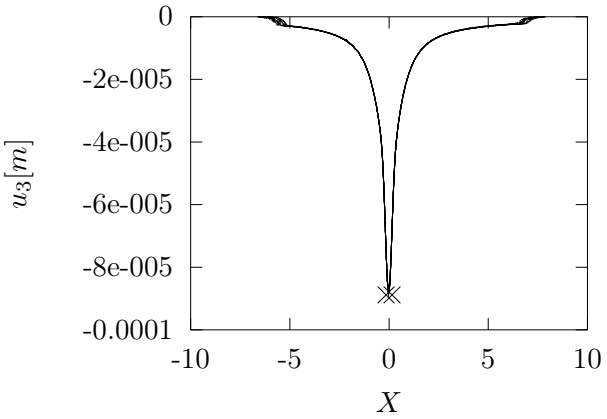

The plot in figure 5.16 shows several bassin sample corresponding to different times in the interval between the load ramp up having finished but before the effects of the Laplace transform grows too large. What it actually considered *the* solution is then an average over these slightly different bassins (Which is also marked in figure 5.16, but frankly quite hard to see.).

Pro:

- Necessary frequency truncation acts as a smoothing filter.
- Integral transform perform well if their basis functions fit the problem well - both pro and con and one could study the best choice of transform more.

Con:

- Short period of time simulated because of aliasing.
- Needs transforms of loads etc.

5.6 Time-solver FEM

One method of validating the methods and models used in this study is comparing with a more standard time-stepping setup in Comsol. The geometry used will be the same in both FEM variants.
Pro:

- Ease of adjusting modelled interval.
- Possibly more intuitive.
- Transforms of loads etc. not needed.

Con:

- Small erros getting propagated and accumulating.
- Seems more sensitive to meshing. Probably in part because of the above bullet point.

5.7 Comparing Laplace FEM to Time-stepper

The software used, COMSOL Multiphysics, includes linear visco-elasticity as a material model. In the time domain it can be set up to model a material that is elastic in compression and visco-elastic in the shear modulus - which is what is reported most often seen in for instance [COMSOL, 2008] and [Rowland Richards, Jr, 2001]. The visco-elastic model is taken to be a Maxwell model which is a case of the generalized version shown in figure 4.4 but redrawn here for convenience in figure 5.17. However note that it is now the shear modulus G which is assumed to behave according to this model - and not the Youngs Modulus E. The tests in this section is therefore parametrized in shear modulus G and bulk modulus K.
It is also important to note that this section is not aimed at realistic or particular meaningful simulations - the goal here is to see a good correspondence between the time-stepping standard procedure and the Laplace transform-approach as described in respectively sections 5.5 and 5.6 in a fairly arbitrary case.

Figure 5.17: Rheological model for the shear modulus in our comparison tests.

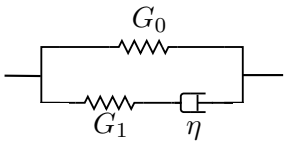

5.7.1 Validation Test Load Assumptions.

The loading will be pulse-like but more spread out than real FWD-pulse and the modelled volumes a bit smaller for technical time-saving purposes regarding fineness of mesh, time-step sizes etc. This choice of load is again for practical purposes. It is the experience of the author that time-stepping in a moving load situation introduces several necessary considerations regarding the fineness of the mesh because of how the load moves across the elements. A possible alleviation is the use of adaptive meshing, meaning refining the mesh automatically where needed, however the author judged that all this detracted from the purely proof of concept of whether time-stepping and the Laplace method gives similar results in a dynamic situation and has chosen pulse like dynamic loads for this validation.
See the actually chosen settings and parameter values in table 5.2.

5.7.2 Validation Test Material Assumptions.

The material parameters used are in the approximate order of magnitude but are not aimed at a particular asphalt mix or the like. This is purely proof of concept of the method from section 5.5 in the case of normal springs or dampers (i.e. exponents of 0 or 1 of the variable dampers the Laplace Transform method was originally aimed at solving, such as in section 4.2.3). See the actually chosen settings and parameter values in tables 5.2 and 5.3.
The Laplace Transformed expression for a one-branched generalized Maxwell model is as explained in section 4.2.1

$$\tilde{G}(s) = G_0 + \frac{1}{\frac{1}{G_1} + \frac{1}{\eta s}}. \tag{5.18}$$

5.7.3 Validation Test Geometry and Meshing.

The same basic geometry as shown in figure 5.7 will be utilized.

Table 5.2: Settings for the simulations used for comparing time-stepping vs transform method.

FEM Parameter	**Settings #1**	**Description**
Geometry		
L	12 m	See table 5.1.
L_∞	1 m	
H	6 m	
H_∞	1 m	
W	6 m	
W_∞	1 m	
Laplace		
$\Delta\omega$	3 rad/s	Discretization step of ω.
N_{samp}	501	# of complex freq. simulated.
T	$\frac{\Delta\omega}{2\pi}$	# of complex freq. simulated.
c	$\frac{\log((2N_{samp}-1)^2)}{T}$	Max imaginary frequency part.
Ω	1500 rad/s	Max imaginary frequency part.
Time-Stepper		
Solver	Gen. Alpha	Choice of time step method.
Tolerance	1e-7	Tolerance.
Δt	1e-5	Time step size.

Table 5.3: Settings for the simulations used for comparing time-stepping vs transform method.

Parameter	**Value Run #1**	**Description**
Load		
Load footprint	Circular	Shape of load footprint.
r_0	0.3 m	Radius of load.
Pulse shape	Rectangular	Shape of load pulse in time.
t_1	0.015 s	Start of pulse in time.
t_2	0.025 s	End of pulse in time.
F_x	0	Total Load i x-direction.
F_y	0	Total Load i y-direction.
F_z	2 122 065.9 N[6]	Total Load i z-direction.
Materials		
Layers #1		
T_1	0.45 m	Thickness of top layer.
K_1	14.167 MPa [7]	Bulk modulus.
G_1	6538.5 MPa [8]	Shear modulus.
ρ_1	2500 kg /m^3	Density of the top layer.
G_0	137.93 MPa [9]	Instanteneous shear modulus.
G_∞	137.93 MPa [10]	Long term shear modulus[11].
η	60 s	Relaxation time.
Layers #2		
K_2	1.3333 MPa [12]	Bulk modulus.
G_2	137.93 MPa [13]	Shear modulus.
ρ_2	1900 kg/m^3	Density.

[6] Actually $\frac{600\,\text{kPa}}{\pi r^2}$.
[7] Actually $\frac{E_1}{3(1-2\nu_1)}$ where $E_1 = 17\,000$ MPa and $\nu_1 = 0.3$.
[8] Actually $\frac{E_1}{2(1+\nu_1)}$ where $E_1 = 17\,000$ MPa and $\nu_1 = 0.3$.
[9] Actually $\frac{E_2}{2(1+\nu_2)}$ where $E_2 = 400$ MPa and $\nu_2 = 0.45$.
[10] Actually $\frac{E_2}{2(1+\nu_2)}$ where $E_2 = 400$ MPa and $\nu_2 = 0.45$.
[11] AKA static shear modulus.
[12] Actually $\frac{E_2}{3(1-2\nu_2)}$ where $E_2 = 400$ MPa and $\nu_2 = 0.45$.
[13] Actually $\frac{E_2}{2(1+\nu_2)}$ where $E_2 = 400$ MPa and $\nu_2 = 0.45$.

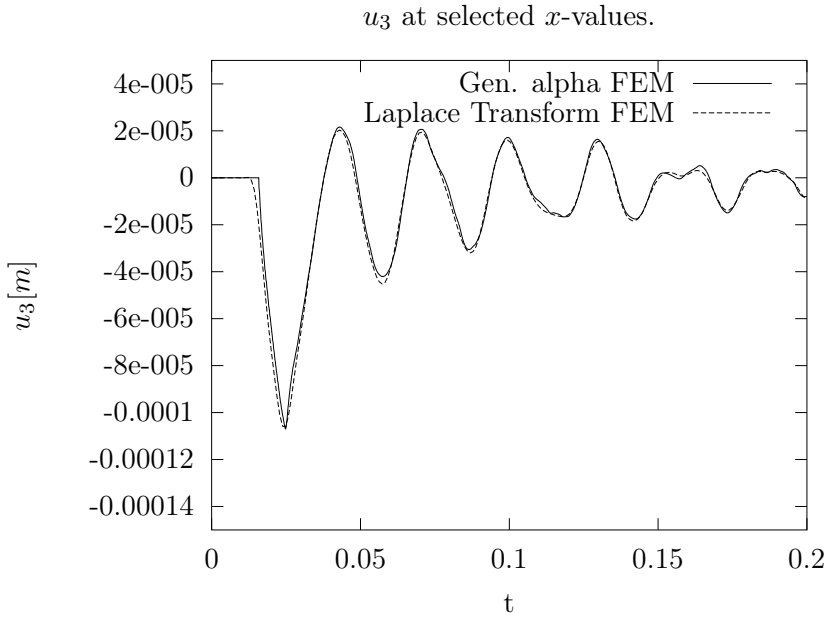

Figure 5.18: Comparison of time stepping to Laplace method by graphing the real part of the Laplace solution and the time stepping solution for run #1 in table 5.3 and settings #1 (Without infinite elements downwards) as in table 5.2 for $(x, y, z, t) = (0, 0, \frac{H}{2}, \cdot)$, i.e. directly under the load.

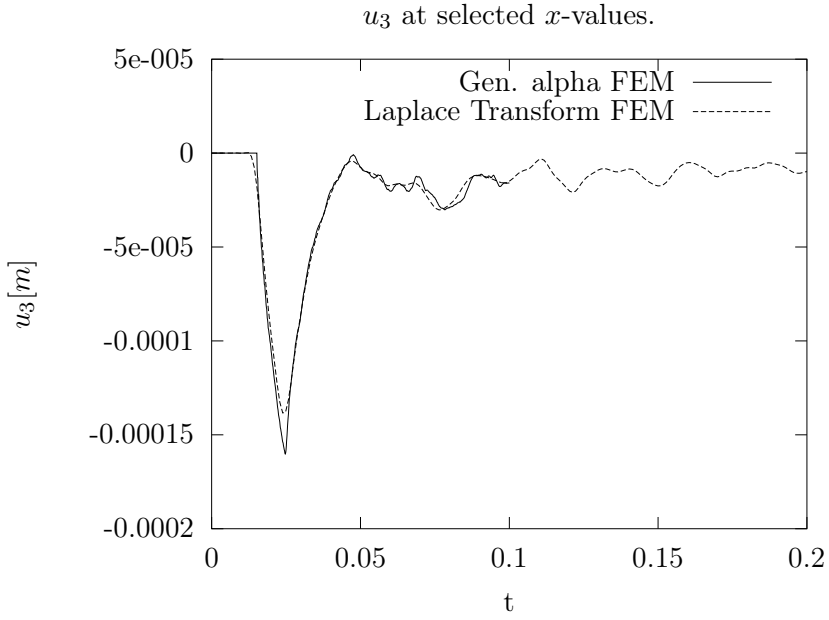

Figure 5.19: Comparison of time stepping to Laplace method by graphing the real part of the Laplace solution and the time stepping solution for run #1 (With infinite elements downwards) in table 5.3 and settings #2 as in table 5.2 for $(x, y, z, t) = (0, 0, \frac{H}{2}, \cdot)$, i.e. directly under the load.

The conclusion from figure 5.18 and 5.19 is in part that infinite elements make a difference but whether they are enabled or not, a good similarity is seen between a standard FEM method and the Laplace-FEM method for this toy problem.

5.7.4 Quasi-static Case

As an extra sanity check see figure 5.20 for the results from a simulation using the same settings as run#1 in table 5.3 but based on a quasi-static assumption meaning dropping the inertial terms in equation (4.6) and equation (4.7). Meaning basing the time-step simulation on

$$\nabla \cdot \sigma(\mathbf{x}, t) = 0, \tag{5.19}$$

and the Laplace method on

$$\nabla \cdot \hat{\sigma}(\mathbf{x}, s) = 0. \tag{5.20}$$

COMSOL allows for simply choosing to exclude the inertial part $\rho \frac{\partial^2}{\partial t^2}$ from equation (4.6) in the time dependant problem setup and in the Laplace method consisting of a series of stationary problems one simply again removes the part ρs^2 from equation (4.7) which was manually added earlier, to the stationary frequency problems in COMSOL, exactly to include inertial effects.

Figure 5.20: Quasi-static solutions produced with time-stepping and Laplace method for comparison for the point $(x, y, z, t) = (0, 0, \frac{H}{2}, t)$, i.e. directly under the load.

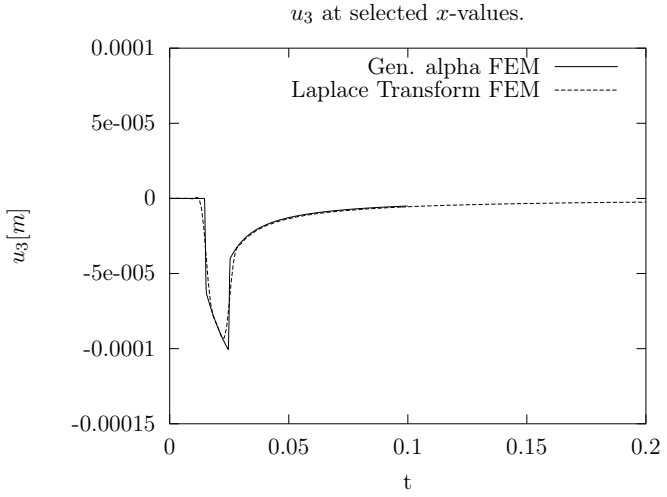

A very good alignment is shown in figure 5.20 this case too lending even more credibility to the setup. The differences in figure 5.20 are attributable to natural properties of the methods used - as mentioned earlier it is to be expected that the truncation of higher frequency smoothes out the Laplace solution and stated in words it does not have access to those frequencies required to hit the abrupt transitions exactly or the very sharpest part of peaks.

5.8 Simulation Results

For the remaining part of the text the following tables will be referred to for parameters and settings.

Table 5.4: Settings for the simulations used.

FEM Parameter	**Settings #4**	**Description**
Geometry		
L	12 m	See table 5.1.
L_∞	1 m	
D	6 m	
D_∞	1 m	
W	8 m	
W_∞	1 m	
N_x	401	# of points for sampling.[14]
Laplace		
$\Delta\omega$	5 rad/s	Discretization step of ω.
N_{samp}	61	# of complex freq. simulated.
T	$\frac{\Delta\omega}{2\pi}$	Time interval.
c	$\frac{\log\left((2N_{\text{samp}}-1)^2\right)}{T}$	Real frequency part.[15]
Ω	300 rad/s	Max imaginary frequency part.

[14] Uniformly distributed along $y = 0$ in $\left[-\left(\frac{L}{2}+L_\infty\right),\left(\frac{L}{2}+L_\infty\right)\right]$.

[15] As in [Zamorano and Campos, 2007].

Table 5.5: Material and load settings.

Parameter	Runs #3-R/S	Run #5-R/S	Run #6-S	Description
Footprint	Rectangular	2×Rectangular	Rectangular	Shape of load footprint
Pulse (-R)	Rectangular	Rectangular	N/A	Load shape. See section 5.4.1.
Pulse (-S)	Sine	Sine	Sine	Load shape. See section 5.4.1.
L_W	0.30 m	0.30 m	0.30 m	Load length along x.
W_W	0.24 m	2×0.24 m[16]	0.30 m	Load length along y.
b_3	N/A	0.1 m	N/A	Gap between twin loads along y.
F_x	0	0	0	Total Load i x-direction.
F_y	0	0	0	Total Load i y-direction.
F_z	−100 kN	−50 kN	−100 kN	Total Load i z-direction.
v	8 m/s	8 m/s	8 m/s	Velocity of the load.
Layer #1		M0251[17]		
T_1	0.45 m	0.15 m	0.45 m	Thickness.
E_0	N/A	1 MPa	1 MPa	Instanteneous Youngs Modulus.
E_∞	N/A	24 908.32 MPa	24 908.32 MPa	Static Youngs Modulus.
E_1	4000 MPa	N/A	N/A	Youngs Modulus.
μ_1	0.3	0.35	0.35	Poisson ratio.
ρ_1	2500 kg/m^3	2484 kg/m^3	2500 kg/m^3	Density.
k	N/A	0.277	0.277	Exponent of variable damper 1.
h	N/A	0.277	0.277	Exponent of variable damper 2.
δ_1	N/A	6.563	6.563	Huet-Sayegh weight of first damper.
Layer #2		M0181 [18]		
T_2	N/A	0.3 m	N/A	Thickness.
$E_{0,2}$	N/A	0.1 MPa	N/A	Instanteneous Youngs Modulus.
$E_{\infty,2}$	N/A	22 685.42 MPa	N/A	Static Youngs Modulus.
E_2	1000 MPa	N/A	1000 MPa	Youngs Modulus.
μ_1	0.45	0.35	0.45	Poisson ratio.
ρ_1	1900 kg/m^3	2394 kg/m^3	1900 kg/m^3	Density.
k	N/A	0.334	N/A	Exponent of variable damper 1.
h	N/A	0.334	N/A	Exponent of variable damper 2.
δ_1	N/A	4.145	N/A	Huet-Sayegh weight of first damper.
Layer #3[19]				
T_3	N/A	0.5 m	N/A	Thickness.
E_3	N/A	300 MPa	N/A	Youngs Modulus.
μ_3	N/A	0.35	N/A	Poisson ratio.
ρ_3	N/A	1900 kg/m^3	N/A	Density.
Layer #4[20]				
E_4	N/A	100 MPa	N/A	Youngs Modulus.
μ_4	N/A	0.35	N/A	Poisson ratio.
ρ_4	N/A	1900 kg/m^3	N/A	Density.

[16] Centered at $(x, y) = (0, 0.17)$ and $(x, y) = (0, -0.17)$ respectively, leaving a 0.1 m gap between the loads/wheels.

[17] [Xu and Solaimanian, 2009]

[18] [Xu and Solaimanian, 2009]

5.8.1 Laplace FEM and ViscoRoute

The software ViscoRoute was developed at LCPC (Laboratoire Central des Ponts et Chaussées) in Nantes, France which has since changed name to IFSTTAR (Institut Français des Sciences et Technologies des Transports, de l'Aménagement et des Réseaux[21]. It aims to model deflection bassins under a moving load in a layered structure.

Figure 5.21: As mentioned in section 5.5.3 shown are bassins corresponding to indices $550, 560, 570, \cdots, 700$ out of 1001 uniformly distributed times on [0,T]

Figure 5.23: Laplace method bassins. See run #5-R (Except only a single rectangular footprint centered at $(0, 0)$, $W_L = 0.30\,\mathrm{m}$,$W_W = 0.30\,\mathrm{m}$, $F_z = -100\,\mathrm{kN}$) in table 5.5. Settings #4 as in table 5.4

Figure 5.22: Laplace method bassins. See run #3-R in table 5.5. Settings #4 as in table 5.4

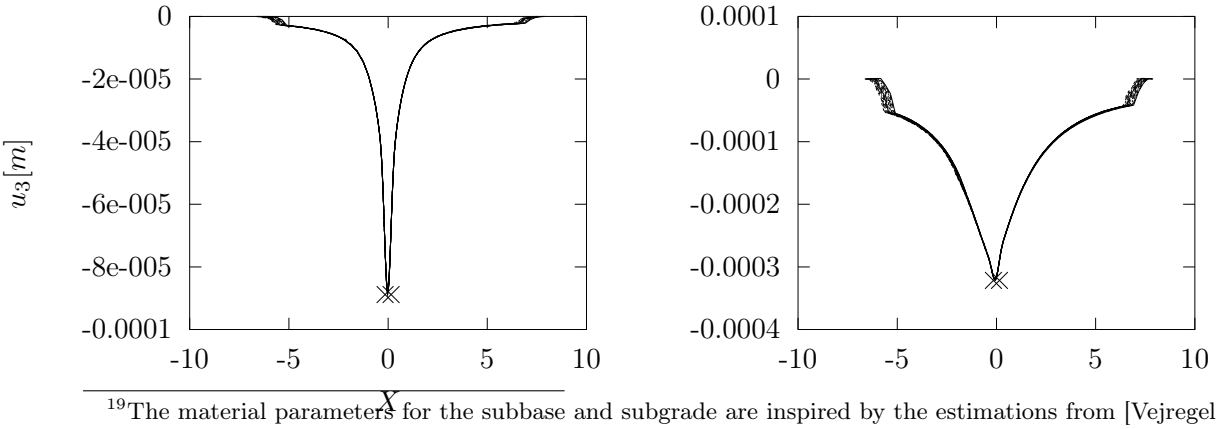

[19]The material parameters for the subbase and subgrade are inspired by the estimations from [Vejregel Arbejdsgruppe P. 21, 2011b, p. 9-10], with E drawn from gravel/stable gravel (Grus/Stabilt Grus in danish) for the subbase

[20]The material parameters for the subbase and subgrade are inspired by the estimations from [Vejregel Arbejdsgruppe P. 21, 2011b, p. 9-10], with E drawn from between gravel(Grus in danish) and sand for the subgrade

[21]www.lcpc.fr and www.ifsttar.fr respectively for more information.

Figure 5.24: Laplace method average solution from 5.22

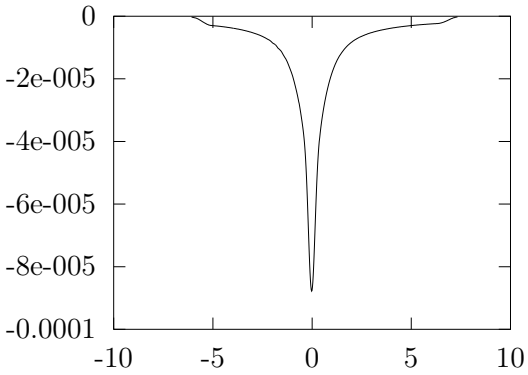

Figure 5.25: Laplace method average solution from 5.23.

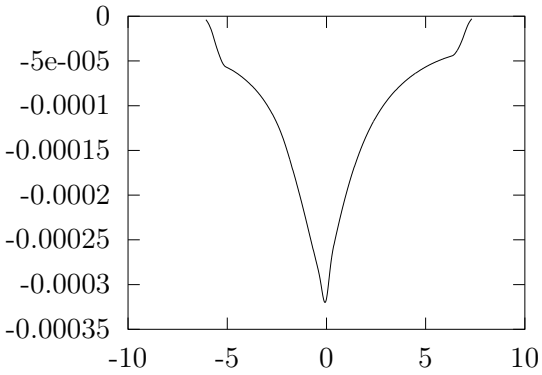

Figure 5.26: Laplace method solution bassin and ViscoRoute bassin for comparable settings as in 5.22.

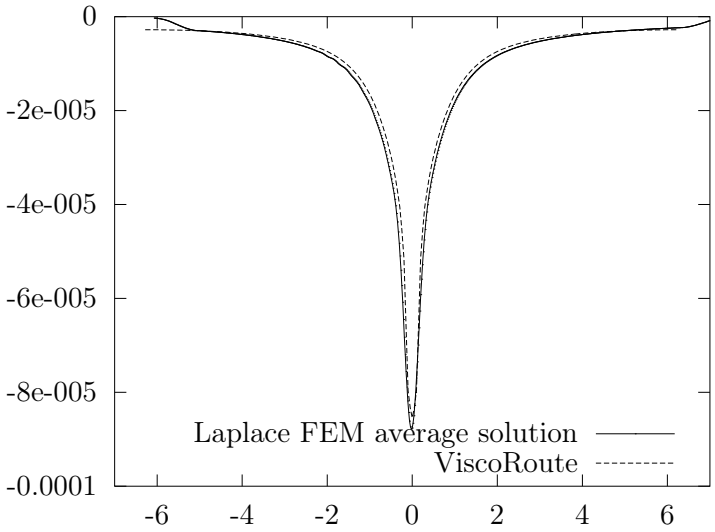

Figure 5.27: Laplace method solution bassin and ViscoRoute bassin for comparable settings as in 5.23.

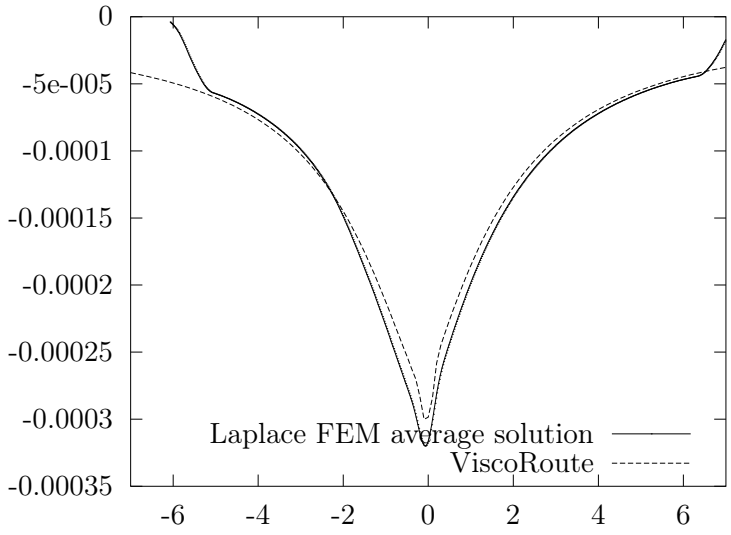

The conclusion here is that a good alignment of ViscoRoute and the Laplace FEM is achieved but more work could be done comparing and understanding ViscoRoute by the author. See also [Vu Hieu Nguyen, 2002] for further insight into ViscoRoute. Seeing as it is a simpler and faster program, and possibly collaboration on further development should be sought.
For now the conclusion will simply be that the similar shape of the bassin lend credibility to the Laplace method.

5.8.2 TSD and FWD Simulation Comparison

Here the load assumptions of section 5.4.1 and section 5.4.2 are used to emulate a TSD and FWD loading respectively along with the settings of Run #5-S 5.5 for the structure itself to compare the outcome of TSD and FWD experiments. Clarifying insights into the differences and similarities between the devices should help develop procedures for the use of TSD measurement with respect to road management responses.

Table 5.6: Material and load settings for the FWD-type simulations.

Parameter	Run #5-FWD-R/S	Description
Footprint	Circular	Shape of load footprint
Pulse (-R)	Rectangular	Temporal load shape. See section 5.4.1.
Pulse (-S)	Sine	Temporal load shape. See section 5.4.1.
r_0	0.15 m	Radius of load.
F_x	0	Total Load i x-direction.
F_y	0	Total Load i y-direction.
F_z	−50 kN	Total Load i z-direction.
v	10 m/s	Velocity of the load.
Layer #1	M0251[22]	
T_1	0.15 m	Thickness.
E_0	1 MPa	Instanteneous Youngs Modulus.
E_∞	24 908.32 MPa	Static Youngs Modulus.
E_1	N/A	Youngs Modulus.
μ_1	0.35	Poisson ratio.
ρ_1	2484 kg/m^3	Density.
k	0.277	Exponent of variable damper 1.
h	0.277	Exponent of variable damper 2.
δ_1	6.563	Huet-Sayegh weight of first damper.
Layer #2	M0181 [23]	
T_2	0.3 m	Thickness.
$E_{0,2}$	0.1 MPa	Instanteneous Youngs Modulus.
$E_{\infty,2}$	22 685.42 MPa	Static Youngs Modulus.
E_2	N/A	Youngs Modulus.
μ_1	0.35	Poisson ratio.
ρ_1	2394 kg/m^3	Density.
k	0.334	Exponent of variable damper 1.
h	0.334	Exponent of variable damper 2.
δ_1	4.145	Huet-Sayegh weight of first damper.
Layer #3[24]		
T_3	0.5	Thickness.
E_3	300 MPa	Youngs Modulus.
μ_3	0.35	Poisson ratio.
ρ_3	1900 kg/m^3	Density.
Layer #4[25]		
E_4	100 MPa	Youngs Modulus.
μ_4	0.35	Poisson ratio.
ρ_4	1900 kg/m^3	Density.

[22][Xu and Solaimanian, 2009]

[23][Xu and Solaimanian, 2009]

[24]The material parameters for the subbase and subgrade are inspired by the estimations from [Vejregel Arbejdsgruppe P. 21, 2011b, p. 9-10], with E drawn from gravel/stable gravel (Grus/Stabilt Grus in danish) for the subbase

[25]The material parameters for the subbase and subgrade are inspired by the estimations from [Vejregel Arbejdsgruppe P. 21, 2011b, p. 9-10], with E drawn from between gravel(Grus in danish) and sand for the subgrade

Figure 5.28: Using the values of run #5-FWD-R in table 5.6 for loads and material and FEM settings #4 of 5.4. Graphed are the deflections experience by fixed points x_n indexed $51, 101, 151, 201$ out of 401 so with the lengths chosen $\{x_n\} = \{-5.25, -3.5, -1.75, 0\}$

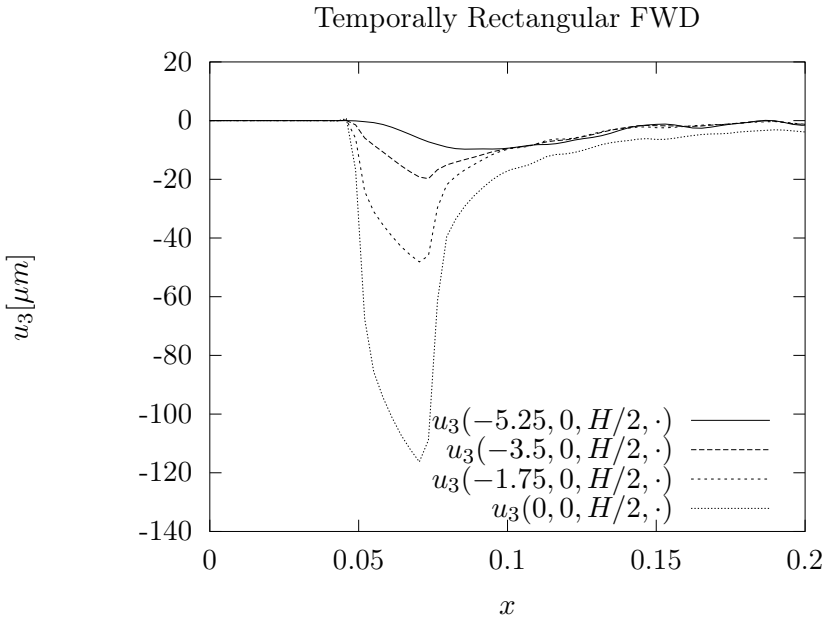

Figure 5.29: Using the values of run #5-FWD-S in table 5.6 for loads and material and FEM settings #4 of 5.4. Graphed are the deflections experience by fixed points x_n indexed $51, 101, 151, 201$ out of 401 so with the length chosen $\{x_n\} = \{-5.25, -3.5, -1.75, 0\}$

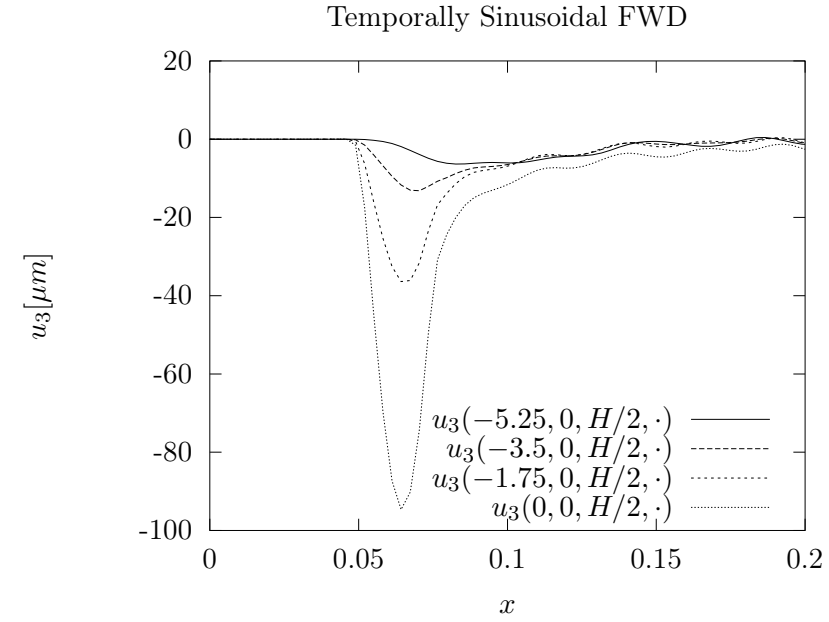

5.8.3 A Preliminary Conclusion Regarding FWD and TSD simulations

It is hard to draw any strict conclusions here. For application purposes the above is meant as a tool for comparing the FWD approach with a TSD approach.
For instance when asked by interested parties what to expect from a TSD measurement as compared to a FWD - "Do they measure the same thing?". A innocently sounding question since they are both deflectometers but with a non-trivial answer the the above tool hopefully sheds light upon.
The FWD loading here is drawn fairly arbitrary however within ranges FWDs can do. It would make more sense, in the context of getting asked the question and asking back which FWD and conditions are inquired about - including road data of course, to input all this into the Laplace FEM method and do a comparison based on simulated data so as to check for systematic differences to be expected.
This might allow for the use of TSD data fairly directly with already established FWD-procedures, which is potentially a big step in spreading the technology among FWD-users and drawing on their huge experience with those setups and procedures for interpreting data.

It is planned to gather approximate master curves from experts for typical road in a TSD operating area together with FWD data from the same roads and do such a study using the above tools.

Figure 5.30: Illustrations of TSD and FWD simulation (x, t) plots of the vertical deflection side by side. TSD bassins moving along on the left figure and on the right the pulse induced by the FWD. As mentioned in the text more studying and fine-tuning is needed to really draw conclusions, but powerful to see them side by side from the same tool.

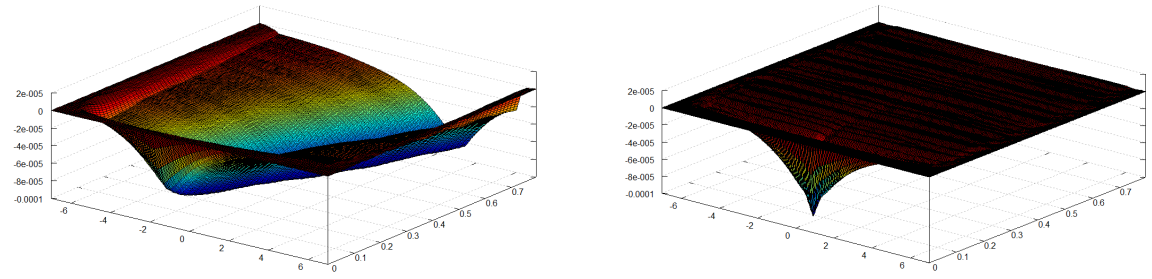

Chapter 6

Synthetic Model

This chapter proposes a practical model which can be used with TSD data. The model will be synthetic in the sense that it is not a fully analytic model derived from first principles, but rather pieced together from experience with such models and from simulations, avoiding some of the problems discussed in previous chapters, and reviewed below.

6.1 Motivation

The TSD gathers a huge amount of data which is averaged runningly over, for instance 10 m or 100 m. The resolution of the TSD is around a 1000 pulses per second and lets assume a velocity of 15 m/s comes out to a lengthwise data spacing of around $\frac{15}{1000}\text{m} = 0.015\text{m}$.
Unfortunately FEM simulations take a prohibitively long time to run for use in data-fitting with all these data acquired by a TSD.

Running FEM simulations for each bassin for numerous possible combinations of parameters for direct comparison with the gathered data does not seem doable within the timeframe needed to process the huge amount of data from the TSD.
Another approach is performing a lot of simulations based on a whole catalogue of parameters. Saving such a variety of simulations in a lookup table could be used to look up which choice of parameter settings give the most similar bassins/slopes to the gathered data.
Such a method using only the forward modelling becomes a huge task as the number of varied parameters grow though, but could concievably be a one-time task.

The author was working on setting up an inverse problem estimating parameters from data using a FEM setting early in the Ph.D. study and preliminary work was done together with co-supervisor Kim Knudsen at DTU. However it also entailed the use of FEM, namely for the forward modelling[1] as an integral part of the process but with the resolution mentioned above was deemed to not be feasible with even just one FEM run per bassin.

[1] Modelling an initial guess around where to perturb.

One could hope that it is possible to capture the important aspects of the road behaviour in a simplified synthetic model based on various observations. Knowledge from other sources such as FEM and other modelling approaches can help validate that such a model is able to encompass typical behaviour satisfactorily well, while having a computational time on a much smaller order than full FEM studies.
Such a model is sought in this section.
The logical development of a deflection model[2] has been the following:

1. Revisiting beam and plate models in section 3.1.3 based on Winkler foundations or similar ended in the conclusion that these are less than optimal for the necessary modeling of both slopes and deflections simultaneously.

2. A modelling approach based on the physically realistic starting point of continuum mechanics was sought.

3. Since flexibility in the used method was desirable, e.g. to study several situations or possible extensions to other structural conditions, FEM was adopted.

4. FEM was deemed computationally too demanding and hence relegated for use in simply studying the situations and generating simulated data.

5. A non-standard FEM approach allowing an interesting class of rheological models was suggested as seen in 5.5.

6. The non-standard FEM approach was sought validated in section 5.7 against the standard method of 5.6 for cases both can handle.

7. A new basis was sought for an empirical model - empirical meaning that the proposed solutions therein do not come directly from a physical equation or first principles .

8. The new proposed model is sought validated in the currect section (6) against:

    - Real TSD data.
    - Simulated data from FEM.

An synthetic model should of course fit well with the datasets on which it is to be used - in this case real data from a TSD.
If the model does this well, one could argue that the job is done.
However it would be much more satisfying to also make a connection to physical principles.
It is shown in section 5.7 that the Laplace FEM method corresponds very well with well-known and trusted FEM techniques for dynamic problems.

It is therefore natural to test newly proposed simpler models to be able to fit simulated data.
First the main ingredient will be introduced:

[2] neglecting the various other offshoots, uses and conclusions.

6.2 Stable Distributions

The model that will be proposed here makes use of stable distributions. In most cases stable distributions densities f as seen in [John P. Nolan, 2007] and [John P. Nolan, 2009] can not be written explicitly in terms of elementary functions.[3]
Instead they are introduced via. their characteristic function ϕ which takes the following form:

$$\phi(k;\alpha,\beta,c,\mu) = e^{ik\mu-|ck|^{\alpha}[1-i\beta\mathrm{sgn}(k)\Phi(\alpha,k)]}, \quad \alpha=]0,2], \quad \beta\in[-1,1], c\in]0,\infty[, d\in\mathbb{R}, \quad (6.1)$$

with

$$\Phi(\alpha,k) = \begin{cases} \tan\frac{\pi\alpha}{2} & \alpha\neq 1 \\ -\frac{2\log|k|}{\pi} & \alpha = 1 \end{cases}. \quad (6.2)$$

Note that there are several other often used parametrizations. This is following [John P. Nolan, 2007].
Now the stable distribution f is given by:

$$f(x;\alpha,\beta,c,\mu) = \frac{1}{2\pi}\int_{-\infty}^{\infty} e^{-ikx}\phi(k;\alpha,\beta,c,\mu)\mathrm{d}k \quad (6.3)$$

In our application where f will be used to model the deflections, the derivative of f in equation (6.3) is needed to model the slopes measured. This derivative can be calculated via. the properties of the Fourier transform[4] as

$$\frac{\partial}{\partial x}f(x;\alpha,\beta,c,\mu) = \frac{1}{2\pi}\int_{-\infty}^{\infty}(-ik)e^{-ikx}\phi(k,\alpha,\beta,c,\mu)\mathrm{d}k, \quad (6.4)$$

or simply approximated from (6.3) as a finite difference quotient

$$\begin{aligned} \frac{\partial}{\partial x}f(x;\alpha,\beta,c,\mu) &\approx \frac{f(x+h;\alpha,\beta,c,\mu)-f(x-h,\alpha,\beta,c,\mu)}{2h}, \quad h<<1 \\ f'(x;\alpha,\beta,c,\mu) &:= \frac{f(x+h;\alpha,\beta,c,\mu)-f(x-h;\alpha,\beta,c,\mu)}{2h}, \quad h<<1. \end{aligned} \quad (6.5)$$

Equation (6.5) has been used for the following, since the software package stabledist, see [Wuertz et al., 2012], to the statistical software R [Hornik, 2012] is used to calculate the stable distribution f instead of re-coding an approximation to the Fourier transform in (6.3). [5].

[3] See also `http://en.wikipedia.org/wiki/Stable_distribution`

[4] Note that the Fourier transform in equation (6.3) is actually the inverse Fourier Transform as per our convention in Appendix .1

[5] Some care has to be taken attempting this and the understanding of the author is that problems stem from the form of the integrand, range of the integrals and that much is gained by changing variables and calculating the integral / cumulative distribution function of the stable distribution density first. Time did not allow for a satisfactory fully self-implemented code to be used yet, however a rudimentary reimplementation of the explanations in [John P. Nolan, 2007] and [John P. Nolan, 2009] seems promising - preliminarily speaking - and will most likely be developed for further use instead of relying on specific software packages

In the parametrization used here μ is the location parameter and c controls the width of the distribution. The parameter α controls the decay/tails of the distribution f asymptotically as shown in [John P. Nolan, 2009] theorem 1.12, and repeated here in equation (6.6) [6].

$$\lim_{x\to\infty} f(x,\alpha,\beta,c,\mu) \propto x^{-(a+1)} \tag{6.6}$$

6.2.1 Properties

The class of stable distribution are called so because of properties related to a generalization of the central limit theorem. As such they are an interesting family of functions, however connections to their potential usefulness in physical modelling is admittedly not known to the author.
The family was chosen due to being a class of smooth functions with parameters controlling skewness/asymmetry and tail behaviour primarily.
It is the intention to further study if this choice could be heuristically defended because of their inherent properties too.
The current heuristics leading to this model were primarily to chose a family with certain parameter options for asymmetry in the hope that the asymmetry from the viscoelastic effects could be captured and at the same time capturing the elastic symmetric reponse with the use of possibly another function. Summing a symmetric function with a asymmetric function from within the same family or class of functions were considered to have a certain mathematical elegance. Again, these are purely heuristic and aesthetic considerations, but it could be hoped that the physical response could be modelled with a relatively simple sum of such functions in the hope that the symmetric and asymmetric part could be captured. Alternatively to possibly think of the sum as the superposition of the responses from different layers - all of which are quite small as the total deflection is small relative to the structure.
The family chosen might have to be modified and hence lose some of their inherent properties such that they are no longer stable distributions but as just mentioned the author feels that also in that case the function should preferably still be chosen within the same family.
These stable distributions now serve as the first attempt at defining a class of functions wellsuited for bassins and slopes, with desirable properties through their characteristic functions.

[6] The statement in equation (6.6) could potentially help in fitting a model to data by first narrowing down the decay parameter α based on the tail of the data before proceeding to the other parameters.

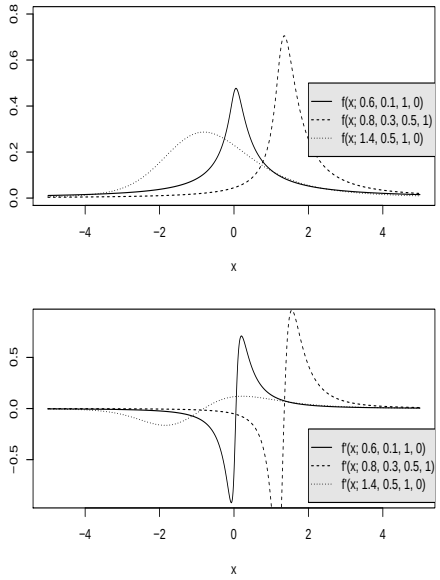

Figure 6.1: Examples of stable distributions and their slopes with a few arbitrary choices for the four parameters as calculated with the R package stabledist and (6.5).

6.2.2 Model Proposal

To better emulate the choice of a moving load moving right and the asymmetry and the choice of deflections positive upwards, flip the stable distributions as follows for convenience:

$$g_1(x;\alpha,\beta,c,\mu) := -f(-x;\alpha,\beta,c,\mu), \tag{6.7}$$

and define

$$g_2(x,\mu_1,\sigma) = -e^{-\frac{(x-\mu_1)^2}{2\sigma^2}}, \tag{6.8}$$

meaning g_2 is a gaussian function or a normal distribution without the normalizing scaling of $\frac{1}{\sqrt{2\pi}\sigma}$. It should be noted that a normal distribution of variace σ and mean μ_1 is a special case of stable distribution for $\alpha = 2$ and $c = \sigma$ and $\mu = \mu_1$.
From equation (6.8) it follows that:

$$\frac{\partial}{\partial x} g_2(x,\mu_1,\sigma) = \frac{x-\mu_1}{\sigma^2} e^{-\frac{(x-\mu_1)^2}{2\sigma^2}} \tag{6.9}$$

$$g_2'(x,\mu_1,\sigma) := \frac{\partial}{\partial x} g_2(x,\mu_1,\sigma) \tag{6.10}$$

$$\tag{6.11}$$

The proposed family of functions g' for modelling the slopes y_n as measured by the TSD at laser positions x_n is now given by:

$$g'(x,\alpha,\beta,c,\mu,x,\mu_1,\sigma,\gamma_x,\gamma_S,\gamma_N) := \gamma_S g_1'(\gamma_x x,\alpha,\beta,c,\mu) + \gamma_N g_2'(\gamma_x x,\mu_1,\sigma), \tag{6.12}$$

with associated deflection bassins given by

$$g(\gamma_x x, \alpha, \beta, c, \mu, x, \mu_1, \sigma, \gamma_x, \gamma_S, \gamma_N) := \frac{1}{\gamma_x}\gamma_S g_1(\gamma_x x, \alpha, \beta, c, \mu) + \frac{1}{\gamma_x}\gamma_N g_2(\gamma_x x, \mu_1, \sigma). \quad (6.13)$$

The parameters in the model is thus the following from which some will be chosen for actual fitting while leaving most fixed.

- α controls the tails of the stable distribution and is always one of the parameters fitted in the optimization. [7]
- β controls the skewness of the stable distribution.
- c controls the width of the stable distribution.
- μ is the location parameter for the stable distribution.
- γ_x scales the models to the right range on the x-axis.
- γ_N scales the contribution of the normal distribution.
- σ is the variance of the gaussian function. It seems likely that σ is correllated with the width of the load, which means it should be fairly constant and a candidate for fixation.
- μ_1 is the location parameter for the normal distribution and is fixed at the mode for the stable distribution.
- γ_S scales the contribution of the stable distribution.

6.3 Comparisons with both Real and Simulated Data

In this section we compare the aforementioned modelling approach with real data from two sets of TSD measurements and with outputs from the Laplace FEM. For the optimization the non-linear least squares function 'nls' in R was used.

6.3.1 Finite Element Method Simulated Data

The method was to do FEM simulations as previously described and export the average bassin. From that slopes was calculated so this slope profile could be attempted fitted with the model of this section. Then with the fitted parameters the associated deflection profile as implied by the synthetic model can be compared with the actual simulated deflection from where the slope data was taken. The initial values of fitted parameters and fixed values of the rest of the parameters can be seen in table 6.1.

[7] The asymptotic behaviour of stable distributions are known and it should be tested if possibly one could make making the data fit more precise and/or efficient/faster by first fitting this decay.

The model is attempted fitted to simulated data from Laplace-FEM simulations as described in section 5, using the settings of run #3-S, #5-S, and #7-S as seen in table 5.5.
The results is shown in figure 6.2, 6.3, and 6.4.

Table 6.1: Parameter settings for datafit. Fitted parameters are denoted with their initial value and an asterix *. These are the manually fitted parameters for figure 6.4, and they also serve as the initial guess for the optimization for the two other fittings.

Parameter	Value	Description
α	0.58	Stable decay.
β	0.18	Stable skewness.
c	12	Stable width.
μ	0	Stable location.
μ_1		Normal mean[8].
σ	1.1	Normal variance.
γ_N	0.6	Normal scale y-wise.
γ_S	90	Stable scale y-wise.
γ_x	10	Joint scale x-wise.

[8]Fixed at the mode of the stable distribution.

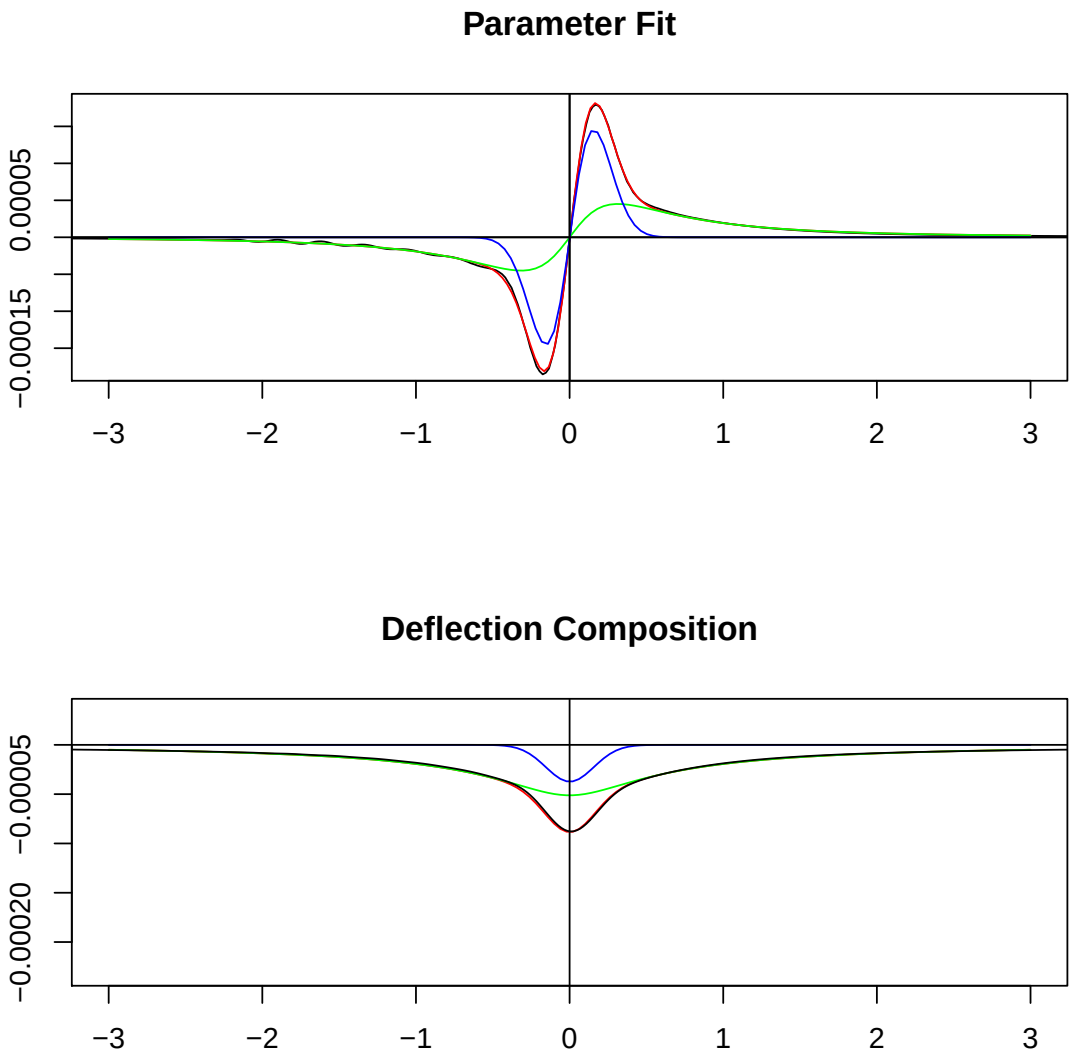

Figure 6.2: Example of a datafit to Laplace FEM slopes from run #3-S as seen in table 5.5. Units are [m] on both axes. The top plot is the FEM slope data in black and the model fitted slope modelling function g' in red with its constituents - the gaussian functions slope g'_2 in blue and stable distribution slope g'_1 in green. Bottom plot is the associated deflection bassin and its composition. A near perfect fit is achieved in this elastic case. See comments after figures.

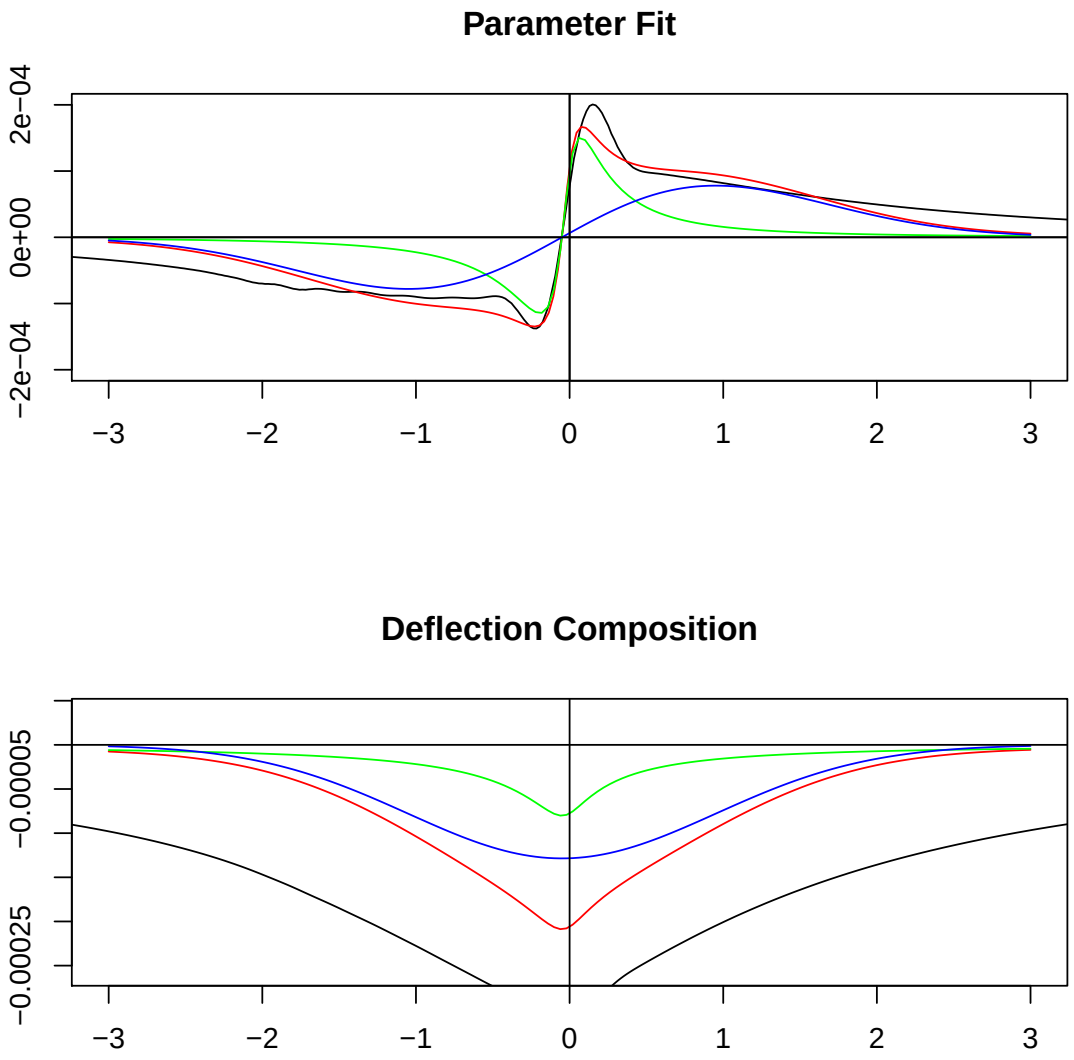

Figure 6.3: Example of a datafit to Laplace FEM slopes from run #5-S as seen in table 5.5. Units are [m] on both axes. The top plot is the FEM slope data in black and the model fitted slope modelling function g' in red with its constituents - the gaussian functions slope g_2' in blue and stable distribution slope g_1' in green. Bottom plot is the associated deflection bassin and its composition. A quite bad fit is achieved in this case. See comments after figures.

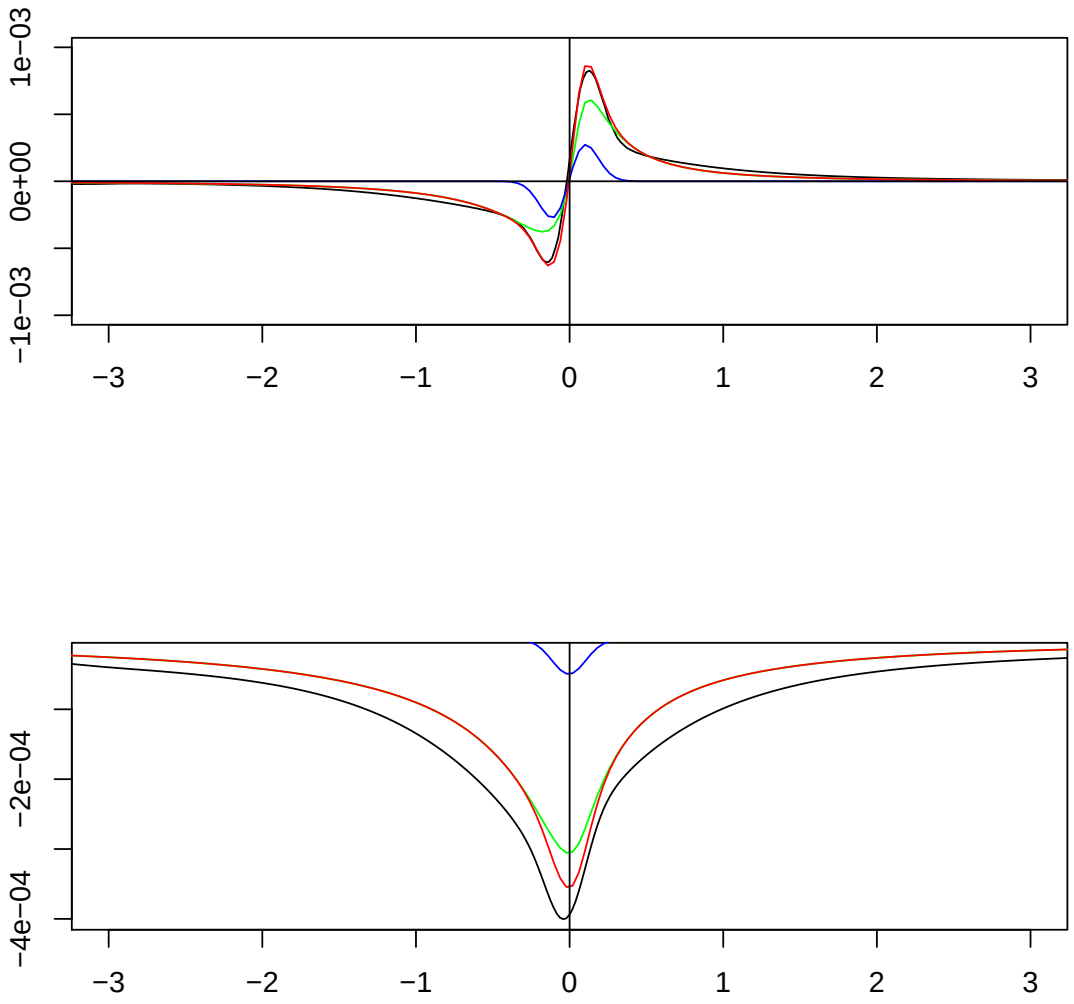

Figure 6.4: Example of a datafit to Laplace FEM slopes from run #6-S as seen in table 5.5.. The top plot is the FEM slope data in black and the model fitted slope modelling function g' in red with its constituents - the gaussian functions slope g'_2 in blue and stable distribution slope g'_1 in green. Bottom plot is the associated deflection bassin and its composition. This fit was done manually and made use of one more parameter $\xi = 0.95$ to translate the entire g'.[9] A seemingly good fit slopewise here. See comments after figures.

There are several important observations regarding figures 6.2, 6.3, and 6.4 to be made.
Firstly, the author would like to point out that 6.2 and 6.4 are examples of how the model was first envisioned. One function with the capability to model the tails and incorporate asymmetry

[9]However it was mostly practical issues regarding parametrization choices that made the author define a new parameter for translation as both g'_1 and g'_2 has location parameters.

and another function to "add in an extra bump" at the load, and it was, and still is hoped, that heuristics regarding such a decomposition as previously mentioned in section 6.2.1 can be defended. As will be shown in the next section, when using an optimization routine sometimes a different setup is suggested where the gaussian component is much wider and takes care of the tail. Firstly, as figure 6.4 illustrates, even if one achieves something which looks like a tantalizingly good fit slope-wise, the small differences in slopes adds up to quite a difference in the deflections.
On the other hand one should consider the entire context: The equipment and measurement situation of a TSD is quite compound and complex. Of course one would wish to model as precisely as possible but the needed precision might be low enough that the difficulty of the task with modelling slopes and deflections at the same time is alleviated. An often used index as mentioned in section 2.1 is SCI300 which as a difference is easier to calculate precisely from slope measurements. An often asked for measure is the deflection at zero, d_0, which the modelling above comes relatively close to - considering the complexity of the task.

At the same time, modelling tools such as the Laplace FEM used in this text contains a lot of adjustment options on top of the maybe most crucial part - the material parameters. The material parameters if for instance run #5 are taken from various litteratures, but as much as the author believes in the potentiel of the Laplace FEM method it does seem the sights are not calibrated since data extracted from the FEM simulations are in the same order of magnitude or exact shape as the actually gathered TSD data.
This discrepancy makes it a big task to create a simpler model which spans so widely.
Looking at figure 6.3 one problem the synthetic model faces seems to be the very heavy tail after the bump, stemming primarily from a quite soft subbase and subgrade.
Another comment to be made regarding such a potential problem with too soft settings for especially subbase and subgrade would be - what is the TSD actually measuring as compared to what is being modelled. If the entire truck it on such a soft structure that it sinks in its entirety together with the road and not just around the heavy loading and measuring trailer - it should not be reflected in the relative measurements.
If such a situation exists there would be a difference in the simulated deflections and velocities seen in the absolute frame of the road as done in the FEM here and the actual measurements.
Before making more comments regarding what future work should and will be done to clarify these questions, let us look at the synthetic model fitted to real TSD data.
After all, giving the above points for improvements and clarification one should maybe prioritize making a model fitting what the TSD sees.

6.3.2 Real TSD Data

This section contains the fitting of the model described in section 6.2.2 to real data acquired from a TSD measurement runs. There are two similar datasets with one being averaged over 100 m containing 35 sets of slopes and the other over 10 m containing 331 sets of slopes. The 10 m dataset however had a problem with the fourth sensor so only five sensors actually have

useful data associated with them.
In this dataset the model will still fit 5 parameters so as to avoid having two different procedures. This is not seen as a problem with respect to overfitting since the restrictions of the model function still apply - i.e. there is not 5 points being fitted with a 5th-degree polynomial which would always be able to fit perfectly. Als interesting to see how the procedure handles an occurrance that will happen, however seldomly. First the 100 m dataset as illustrated in figure 6.5. For now 5 parameters $(\alpha, \beta, \gamma_N, \gamma_S, \sigma)$ are fitted and see table 6.2 for the initial values and fixed values of the model parameters.
Shown will be examples drawn forward at the authors discretion to show when the data-fit looks promising, when it is typical and a few examples in ways it can go wrong. Two examples of each categories of good, decent and poor will be shown from each data set as deemed by the author. The full sets of fitted models are enclosed on the USB-disc in the back. The R-scripts used for this are also to be found there.

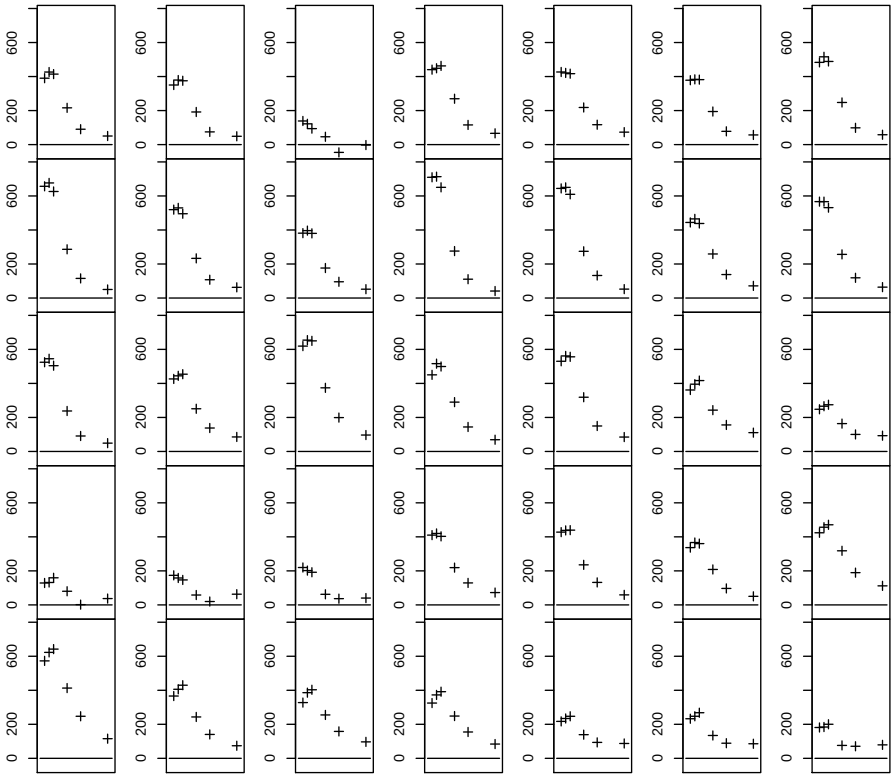

Figure 6.5: Dataset with 100 m average

Table 6.2: Parameter settings for datafit. Parameters which will be fitted are denoted with their initial value and an asterix *.

Parameter	Value	Description
α	0.8^*	Stable decay.
β	0.03^*	Stable skewness.
c	0.8	Stable width.
μ	0	Stable location.
μ_1		Normal mean[10].
σ	2^*	Normal variance.
γ_N	1^*	Normal scale y-wise.
γ_S	1^*	Stable scale y-wise.
γ_x	1.5	Joint scale x-wise.

[10]Fixed at the mode of the stable distribution.

Now the dataset with 10 m averaging in effect:

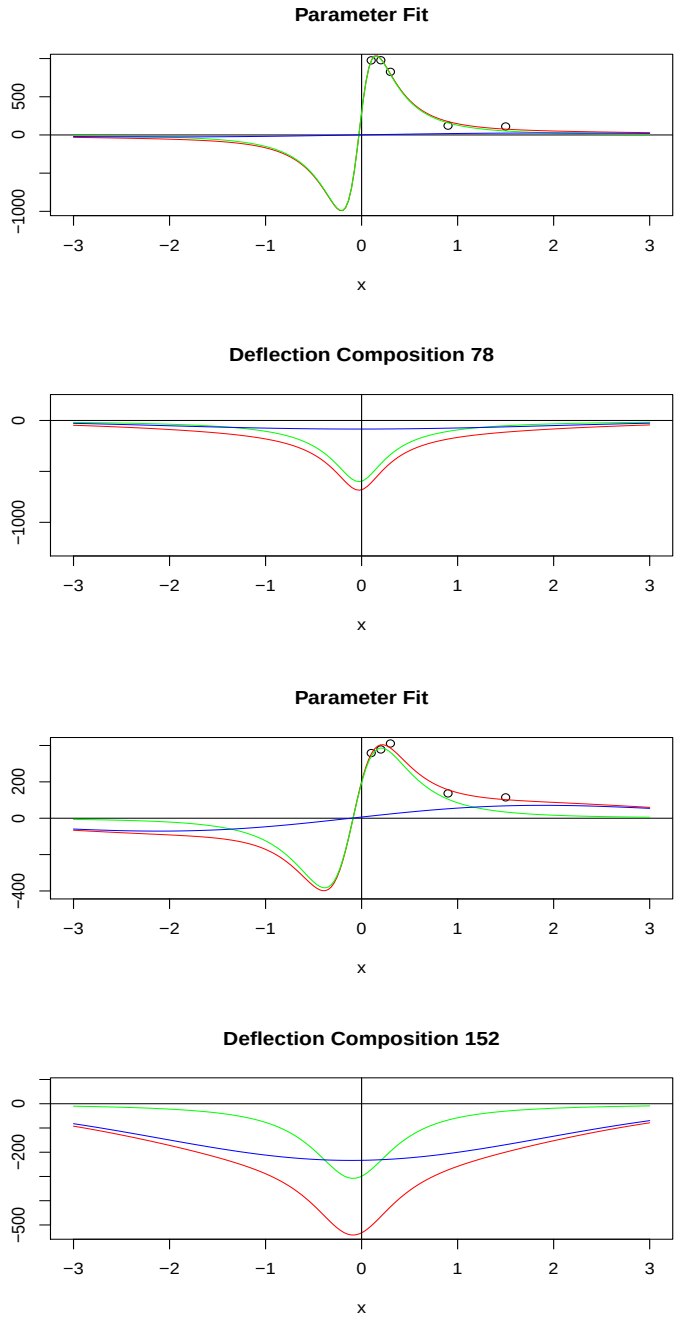

Figure 6.6: Example of a datafit to real measured data on index 78 and 152 in the 10m dataset. Measured slopes at their respective positions shown with circles. Top plot shows the model fit after optimization. Bottom plot shows deflection profile. Both are split into the constituent gaussian function and stable distribution associated with fitted parameters in blue and green respectively.

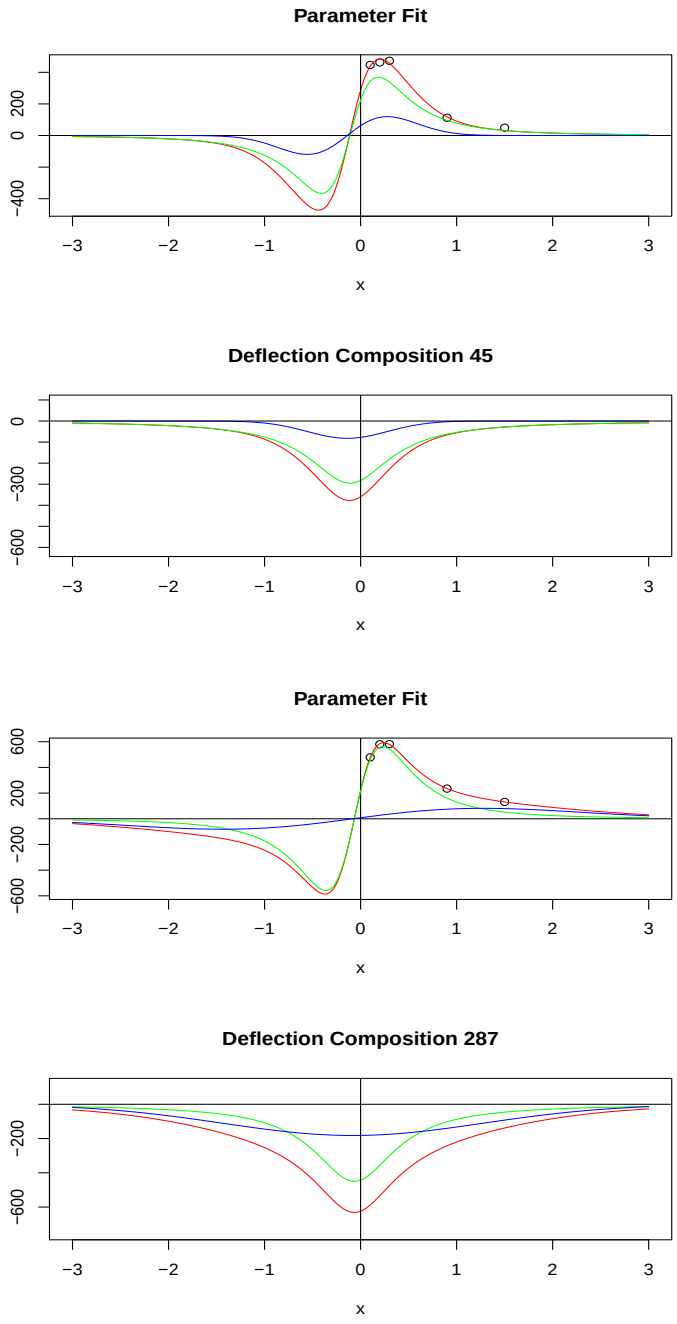

Figure 6.7: Example of a datafit to real measured data on index 45 and 287 in the 10m dataset. Measured slopes at their respective positions shown with circles. Top plot shows the model fit after optimization. Bottom plot shows deflection profile. Both are split into the constituent gaussian function and stable distribution associated with fitted parameters in blue and green respectively.

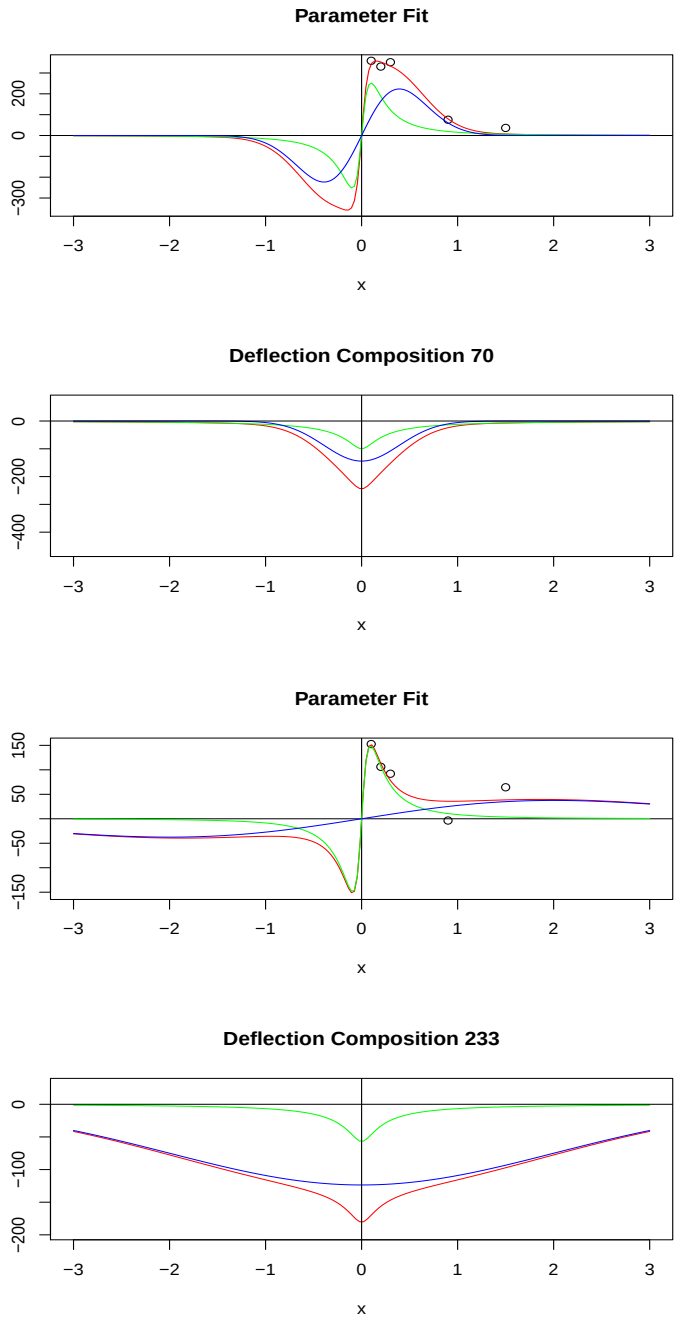

Figure 6.8: Example of a datafit to real measured data on index 70 and 233 in the 10m dataset. Measured slopes at their respective positions shown with circles. Top plot shows the model fit after optimization. Bottom plot shows deflection profile. Both are split into the constituent gaussian function and stable distribution associated with fitted parameters in blue and green respectively.

Now the dataset with 100 m averaging in effect:

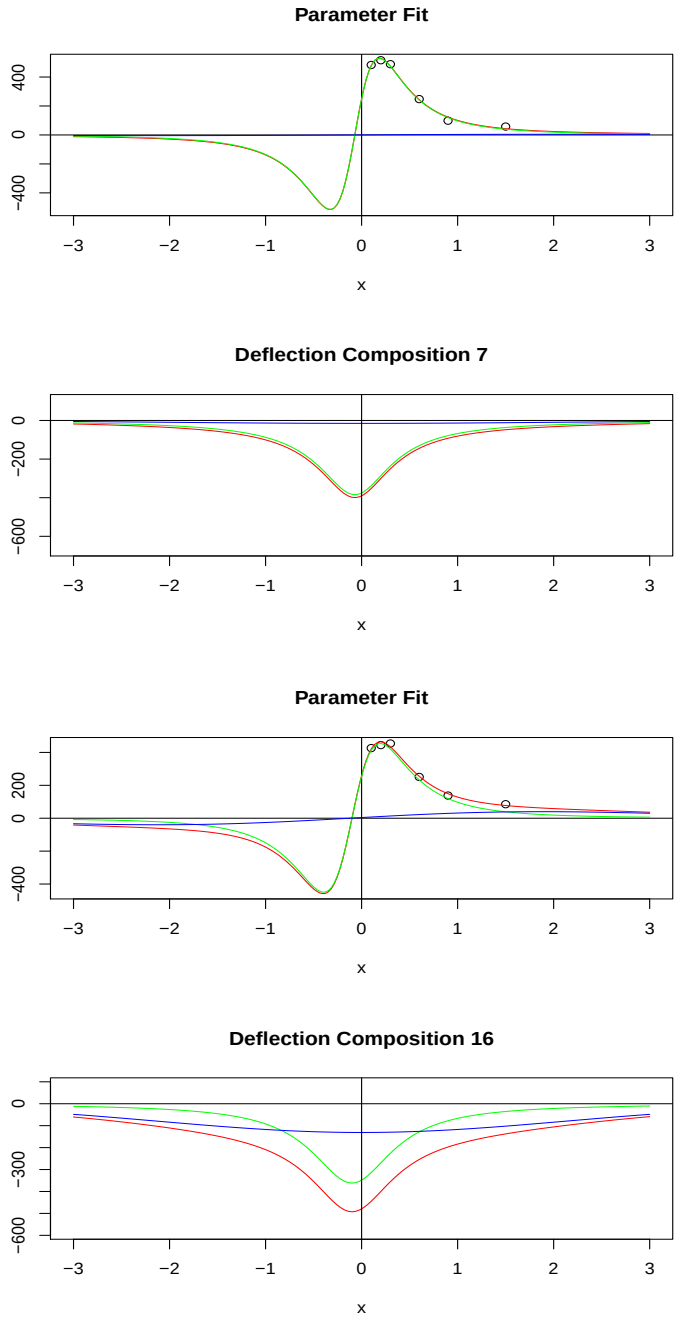

Figure 6.9: Example of a datafit to real measured data on index 7 and 16 in the 100mdataset. Measured slopes at their respective positions shown with circles. Top plot shows the model fit after optimization. Bottom plot shows deflection profile. Both are split into the constituent gaussian function and stable distribution associated with fitted parameters in blue and green respectively.

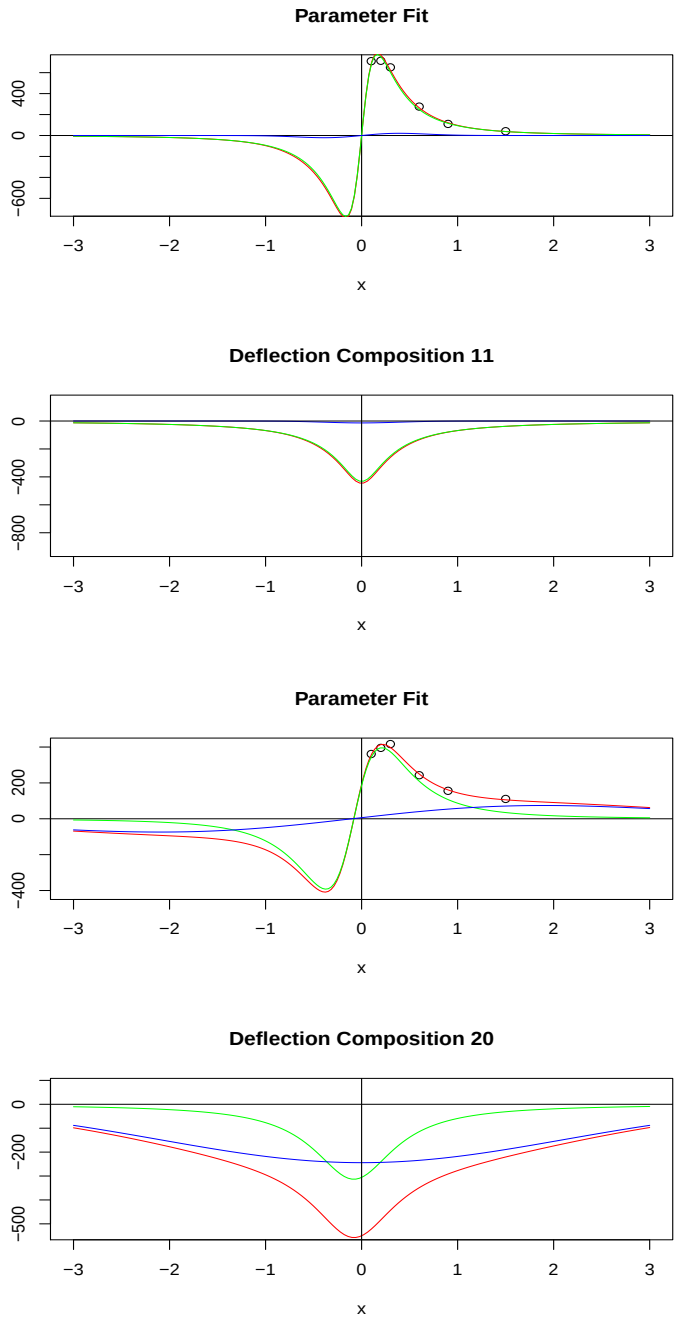

Figure 6.10: Example of a datafit to real measured data on index 11 and 20 in the 100m dataset. Measured slopes at their respective positions shown with circles. Top plot shows the model fit after optimization. Bottom plot shows deflection profile. Both are split into the constituent gaussian function and stable distribution associated with fitted parameters in blue and green respectively.

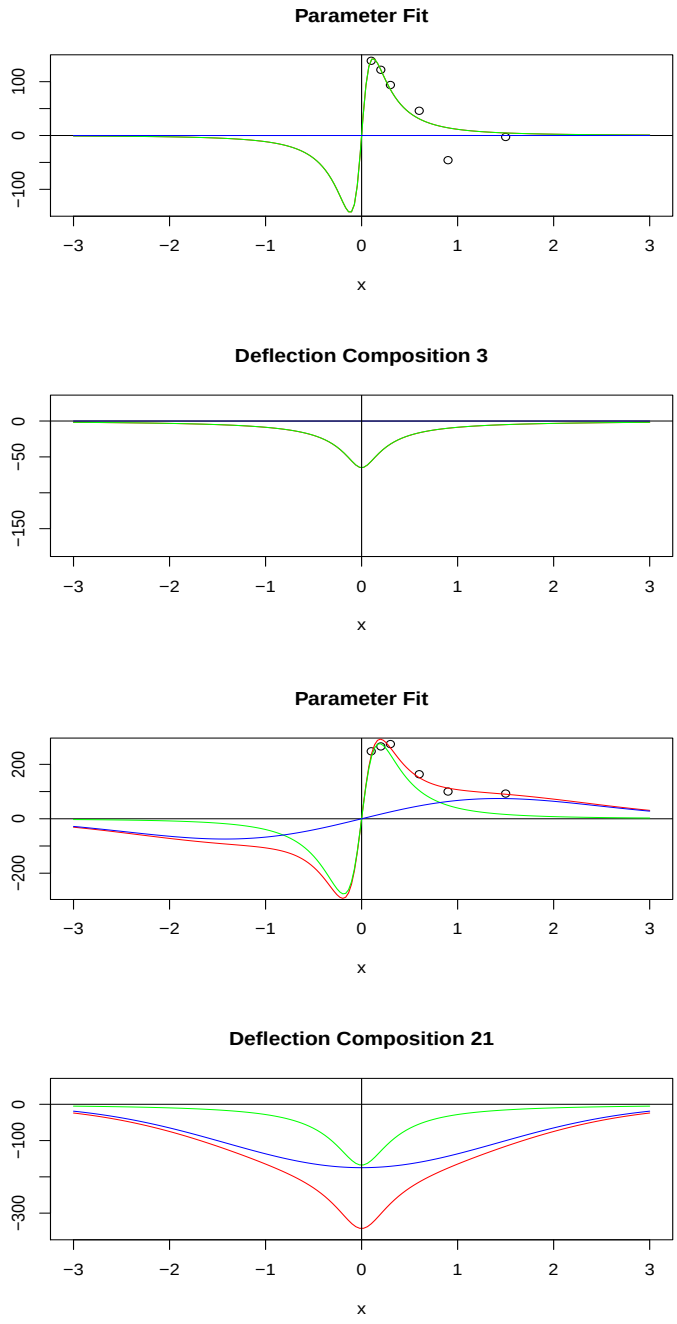

Figure 6.11: Example of a datafit to real measured data on index 3 and 21 in the 100m dataset. Measured slopes at their respective positions shown with circles. Top plot shows the model fit after optimization. Bottom plot shows deflection profile. Both are split into the constituent gaussian function and stable distribution associated with fitted parameters in blue and green respectively.

It is important to point out that the above is still very much a work in progress. The analysis of which parameters should be fixed and which to be fitted leaves work to be done. Viewing the above as a starting point for future research the author finds it encouraging.

Chapter 7

Conclusion

Here the study and report will be concluded upon - more or less sectionwise.
The author will allow himself for the use of a more personal tone to better convey some of the following which are both based on solid research and some views and experiences which will be more based on qualified guesses, non-quantified observations and good old gut feelings.
Firstly let me sum up the report and give my suggestions for further work, before moving into an evalution of the Ph.D. study in broader terms.

7.1 Findings

The author finds in chapter 3 that beam and plate models on Winkler foundations and similar models leaves room for improvement for the usage sought here.
The reasons for this when it comes to the most basic and easily solved models such as the ESGI beam model or a Winkler plate model is simply a poor fit with observed data. As mentioned in sections 3.1.1 and chapter 3 there is other work out there regarding beam and plate models however the author has not seen an approach that both models both the deflections themselves and the slopes.
A good peak value fit of deflections has been seen for instance but with qualitatively and quantitatively different slopes making the computation from acquired slope data to deflection bassins a hard task.
Also regarding beam and plate models it is also important to remember that the starting premise of a beam or plate-like behaviour is in no way justified dealing with a more halfspace-like structure as a road structure.

If beam or plate models are sought in a generalized manner they could become unweildy and for instance lose their important property of explicit solutions.
It is the view of the author that if one is already introducing slightly unrealistic models and parameters and the model framework at the same time becomes complicated one might as well take the more complicated but physically defendable framework of continuum mechanics as the starting point.

Also choosing an unphysical/un-realistic model and using the solutions from there to forcibly fit onto real data - for the only sake of wanting some sense of governing model equation - is just as much guesswork as simply going to an empirical model directly. And hard to do.

Chapter 5 explained and validated the Laplace FEM allowing for the use of variable dampers in for instance a Huet-Sayegh model. Also granting certain features with regards to smoothing and seemingly easier meshing at the cost of a restricted modelling interval. The author has much faith in the usefulness of this approach given its flexibility and access to interesting rheological models.
Finally Chapter 6 introduced a synthetic model based upon observations of simulated and real data. The results were intriguing and invites further work. Also the chapter brought up some apparent discrepancies between simulations and data which is a priority to resolve.
Beam and plate models are put aside until situations arise where the assumption might be more fitting, bridges or rail roads possibly. Also the validation process regarding Laplace FEM vs. Time Stepping was found satisfactory. Leaving my overall conclusion that I find the approach promising. Learning and studying the behaviour through Laplace FEM and adopting a computationally simpler model to capture the essentials.

The answer to the main thesis statement, regarding whether a new model based on more advanced and realistic mathematical simulation of asphalt physics can fit data from the Traffic Speed Deflectometer better - and whether further useful information can be extracted from this data, is from the authors point a view cautiously affirmative. The author believes that the synthetic model will be useful for extracting for instance information about the asymmetry of the bassin and that it, or a variant thereof, can fit data better.
Coupled with the Laplace FEM for a better future understanding of pavement dynamics, it is deemed that these mathematical methods are valuable for a further development. However there is still calibration and research to be done but the author strongly believes more work along these lines would be well invested.

As mentioned several times throughout the text the are many avenues of possible improvements which will now be attempted organized a bit.

7.2 Future Work and Recommendations

The TSD is continuously being developed and the author will soon have access to data from the newer TSD with 9 measurement lasers and data from roads about which more information is given plus FWD from the same roads. It will be a rich opportunity to further the above studies of TSD vs. FWD and bassin modelling given more data points and it will be most interesting to work on the following while further developing the concepts presented in this study.
The author recommends further pursuing the following points in a prioritized man-

ner

- Determine material parameters to be used in Laplace FEM.

This point is crucial - more realistic pavement parameters must be obtained. Whether it will come from laboratory master curves etc. from experts in the field or simply from trial and error of actual simulations held up against real TSD and FWD measurements. It can be hard to evaluate how realistic laboratory measured parameters are and there are many different measurement procedures.

- Attempt, given better estimates of parameters or as part of that process, to achieve a convergence of TSD-like simulations and FWD-like simulations towards real TSD and FWD measurements respectively on a stretch of road.

Such a study would also shed light on the similarities and differences between data from a TSD and a FWD, opening up for a translation procedure and interchangeability regarding the data interpretation procedures.

- Further development of the synthetic model. The author will continue working on the choice of function family and parameter settings for use in the model.

As the simulation tool is calibrated with better parameters and choice of settings the simulated data should provide much information about essential behaviour to help improve synthetic models.

- Further FEM studies with the considered Laplace method for geometric variations
  - Youngs modulus increasing with depth to continue not having a reflecting cutoff boundary but also not having the unrealistic assumption of a last infinite layer.
  - How transitions of material parameters or gaps in various layers affect measurements. Preliminary simulations of such have already been run, but not in a polished enough manner for inclusion and conclusions here yet.
  - Different geometric setup, e.g. a trapezoidal cross-section to make sure stresses have space to cone out downwards and are not cutoff by boundaries.
  - Footprint and shape of load pulses based on real measurements of typical tires.
  - Regarding the loads: Loads near transverse boundaries, uneven loads, tire footprint influence, pulse shape influence and the like are all interesting points.

- It is strongly recommended to look into velocity-based indexation of roads.

Much of the information wanted about pavements is conjectured to be in the more raw velocity data without attempting to calculate absolute deflections. This should be looked into using the methods of this study as a tool, to help understand the connection between raw velocimetry data and pavement structural condition.

- Varying load, e.g. a harmonic oscillation of load amplitude as loading is now measured in the TSD with strain gauges and it could be a valuable source of fine-tuning and correcting for load variation.

Understanding the dynamic reponse better both from a modelling viewpoint and from a purely signal analytic viewpoint is an important point for making corrections to take into account the dynamics within the TSD.

- Simulating situations such as a sudden transition to much softer/harder material and looking into whether it can be seen in the real data across the lasers.
- More thorough search of and comparisons with various analytic solutions and approximations available - e.g. points loads on halfspaces, Bousinessq equations. [Per Ullidtz, 1987] and [Per Ullidtz, 1998].
- Similarly: more comparisons with traditionally used models.
- Studying if the choice of integral transform is optimal - Fourier performance vs. Laplace, possibly Mellin or Hilbert transforms also.

The author also recommends the following regarding the use, setup and development of Traffic Speed Deflectometers.

- Measuring behind the wheel load would be very interesting to look into the asymmetry and thereby the viscoelasticity of the bassin[1] and testing up against the methods used here that take into account asymmetry.
- It is possible that certain situations approach the assumptions of beam/plate models. Certain stretches of asphalt, hard subsurfaces, bridges etc.
- A recurring theme is the question of how many lasers to install. The author believes more lasers further out in the bassin would greatly help estimating the tails of the bassin and hence increase precision in the deflection calculation and give hints to the proper development of the synthetic model.

Regarding the number of Doppler lasers and their positioning: To elaborate on the amount of lasers. It can be argued that one should use less parameters than data points which for this use

[1] The newer TSDs already have this capability.

is the number of lasers used.
Therefore it could always be argued that the number of lasers should be increased since, for the sake of argument, lets say we have a 4 layer road with some visco-elastic behaviour in the top layers. The amount of parameters to account for the dynamics quickly adds up even assuming temperature can be taken into account otherwise and leaving that out. The amount of lasers is presently left up for decision of the customer but it will be most interesting to shift to working with data from some of the newer design with more lasers. Hopefully, and quite likely to the author, studying the dynamics of typical roads will also help optimize the positioning and configuration of both measurement and reference lasers.

7.3 Study Process

I would like to take the time to make a small evaluation of the Ph.D. study. Without burying the reader in actual number of hours and periods here is an outline of the Ph.D. study as a whole.

I started out pursuing extended beam models via. Timoshenko beam theory and at some point the finite element method was suggested as possibly interesting by the Greenwood CEO. I looked into it, having no experience in it exactly, but with a toolbox of functional analysis especially in the bag, the basic principle seemed approachable.

A considerable amount of time was spent on an envisioned inverse problem (Known as backcalculation in the pavement modelling community.) and it was done within a FEM framework to use a FEM forward simulation for an initial guess and the searching for a small pertubation in the material parameters fitting the data. I took courses related to inverse problems. Preliminary work was done on an inverse problem setup with some initial success, however as mentioned in section 6 FEM as the actual foundation for data processing was deemed too heavy.
Hence this inverse problem was relegated, for the time being at least, to being a possible academic pursuance and less of a practical one. As practical solutions are needed for an industrial Ph.D. study - where of course the interests of the company funding it has a big say in what should be focused on - other avenues were chosen instead, and the author has not had time yet to return to the interesting framework of inverse problems.

I took an interest in certain asphalt models that were easier to write up in a frequency domain and looked into how to model using transforms - Fourier or Laplace. Knowing that frequency analysis could be done in certain FEM packages I decided the combination of a transform with FEM might be interesting and started investigating it. The Laplace transform was chosen because of not going back to $t = -\infty$, knowing that the Laplace transform was used with viscoelasticity and a hunch it could be well suited. Also it would allow for fairly easy inclusion of initial values, although that has not been used here - yet.

During the study I have taken two courses in various aspects of FEM, inverse problems, combi-

natorics, road structures and self studying learning MATLAB, Octave, Maple and R scripting. I have also completed the industrial Ph.D. course. I have participated in two ESGI weeks - once as a contributor and once as the company representative where the problem sought solved was related to image recognition. The dissemination of maths as required during a study has been done in several ways, besides the aforementioned ESGI participations. One avenue was by helping colleagues at Greenwood Engineering with challenges of a mathematical nature. I have consulted on a variety of topics such as inertial positioning, image recognition, and signal analysis. I have also made research presentations both at DTU and through Greenwood Engineering for interested parties and an article for Transport Research Arena 2012 in Athens - see Appendix .7.

Finally I would just like to say it has been most rewarding learning and gaining insights into a wide variety of topics and I very much look forward to continuing the work along the outlines above, and I thank the reader for your attention.

Bibliography

A.C. Fowler. *Mathematical Models in the Applied Sciences*. Cambridge Texts in Applied Mathematics, 1997.

Adam Loverro. Fractional Calculus: History Definitions and Applications for the Engineer, 2004. Department of Aerospace and Mechanical Engineering, University of Notre Dame, IN 46556 U.S.A.

Allan F. Bower. Applied Mechanics of Solids, 2008. Online available text - `http://solidmechanics.org/` .

Lars Andersen. *Wave Propagation in Infinite Structures and Media*. PhD thesis, Department of Civil Engineering, Faculty of Engineering and Science, Aalborg University, 2002.

ARA, Inc. and Eres Consultants Division. Guide for Mechanistic-Empirical Design, 2004. Prepared for NCHRP, National Cooperative Highway Research Program. Transportation Research Board, National Research Council.

Axel O. Bohn. The History of the Falling Weight Deflectometer (FWD) , . `http://sites.grontmij.dk/Pavement-consultants-com/About-us/Fwd-history/Pages/default.aspx` .

Susanne Baltzer, David Pratt, Justin Weligamage, Jens Adamsen, and Gregers Hildebrand. Continuous Bearing Capacity Profile of 18000 km Australian Road Network in 5 Months, 2010. 24th ARRB Conference, Melbourne Australia 2010 - also available through `www.greenwood.dk` .

Brent Rauhut Engineering, Inc. Advanced Methods for Using FWD Deflection-Time Data to Predict Pavement Performance, 1997. FHWA Publication number: FHWA-RD-97-093, FHWA Contact Person Cheryl Richter - `http://www.fhwa.dot.gov/pavement/pub_details.cfm?id=244`.

A. Carini, P. Gelfi, and E. Marchinal. An Energetic Formulation for the Linear Viscoelastic Problem: Part I: Theoretical Results and First Calculations , 2008.

A. Chabot, P. Tamagny, D. Poché, and D. Duhamel. Visco-elastic modelling for asphalt pavements - Software ViscoRoute.

A. Chabot, O. Chupin, L. Deloffre, and Duhamel D. Viscoroute 2.0: a tool for the simulation of moving load effects on asphalt pavement. *Road Materials and Pavements Design*, X, 2009.

COMSOL. Viscoelastic Material - Solved with COMSOL Multiphysics 3.5a, 2008. COMSOL Instructions.

COMSOL. COMSOL Multiphysics Users Guide ® 1998-2011, 2011.

Lokenath Debnath and Dambaru Bhatta. *Integral Transforms and Their Application.* CRC Press, 2007.

K. Dias, J. Gravesen, P.G. Hjorth, P. Larsen, C. Please, N. Radulovic, and L. Wang. Beneath the Wheel: Greenwood Engineering. ESGI report, 2005.

John W. Eaton, David Bateman, and SÃ¸ren Hauberg. *GNU Octave Manual Version 3.* Network Theory Limited, 2008. ISBN 0-9546120-6-X.

Jacob Fish and Ted Belytschko. *A First Course in Finite Elements.* Wiley, 2007.

G.R.Liu and Nguyen Thoi Trung. *Smoothed Finite Element Methods.* CRC Press, 2010.

M.S.A Hardy and D. Cebon. Response of Continuous Pavements to Moving Dynamics Loads. *Journal of Engineering Mechanics*, 119, 1993.

M. Hayes, S.B.G.O'Brien, and J.H. Lammers. Green's function for steady flow over a small two-dimensional topography. *Physics of Fluids*, 12:2845–2858, 2000.

Kurt Hornik. The R FAQ, 2012. ISBN 3-900051-08-9 - `http://CRAN.R-project.org/doc/FAQ/R-FAQ.html`.

Jacob Ajslev Hersbøll. Undersøgelse af kørebanedeformationer ved hjælp af en Traffic Speed Deflectometer. Master's thesis, Technical University of Denmark, 2008.

Jørgen Krarup. *Bearing Capacity and Water - Part II: Measured Response.* PhD thesis, Institute of Roads, Transport & Town Planning - Technical University of Denmark, 1994. Report no. 74, Danish Road Institute Note 249.

John P. Nolan. Numerical calculation of stable densities and distribution functions. *Communications in Statistics. Stochastic Models*, 13:759–774, 2007.

John P. Nolan. Stable Distributions - Models for Heavy Tailed Data, 2009. `http://academic2.american.edu/~jpnolan/stable/chap1.pdf`.

Maplesoft. Maple User Manual. Toronto: Maplesoft, a division of Waterloo Maple Inc., 2005-2012.

G. Thomas Mase and George E. Mase. *Continuum Mechanics for Engineers, Second Edition.* CRC Press, 1999.

Ministerie van Verkeer en Waterstaat. Revival of the Huet-Sayegh response model - Notes on the Huet-Sayegh Response model. `english.verkeerenwaterstaat.nl/English/` , 2012. Not known to be published.

National Research Council (U.S.). Transportation Research Board and Universidad Católica de Chile and Ingenieria Dictus. Development of a Simplified Method for Interpreting Surface Deflections for In-Service Flexible Pavement Evaluation. In *Eighth International Conference on Managing Pavement Assets*, 2011. ISBN 9789561412309.

Per Ullidtz. *Pavement Analysis*. Elsevier, 1987.

Per Ullidtz. *Modelling Flexible Pavement Response and Performance*. Polyteknisk Forlag, 1998.

A.C. Pronk. The Variable Dashpot. Working paper for the Rijkswaterstaat in the Netherlands, 2003.

Soren Rasmussen, Lisbeth Aagaard, Susanne Baltzer, and Jorgen Krarup. Comparison of two years of network level measurements with the Traffic Speed Deflectometer, 2008. Transport Research Arena Europe 2008, Ljubljana - also available through `www.greenwood.dk` .

Rowland Richards, Jr. *Principles of Solid Mechanics*. CRC Press, 2001.

Shyam S. Sablani, Ashim K. Datta, M. Shafiur Rehman, and Arun S. Mujumdar. *Handbook of Food and Bioprocess Modeling Techniques*. CRC Press, 2006.

J-M Simonin, D. Lèvre, S. Rasmussen, and G. Hildebrand. Assessment of the Danish High Speed Deflectograph in France, 2003. Study and trials partly funded through the EU FORMAT project done in cooperation with LCPC, France - also available through `www.greenwood.dk` .

Vejregel Arbejdsgruppe P. 21. MMOPP Dimensioneringsprogram for vejbefæstelser - Brugervejledning. `http://vejdirektoratet.dk/DA/vejsektor/ydelser/programmer/Sider/Dimensioneringsprogram.aspx`, 2011a.

Vejregel Arbejdsgruppe P. 21. VEJREGEL - DIMENSIONERING AF BEFÆSTELSER OG FORSTÆRKNINGSBELÆGNINGER - ANLÆG OG PLANLÆGNING. `http://www.vejdirektoratet.dk/DA/vejsektor/vejregler-og-tilladelser/vejregler/Sider/Vejregelgrupper.aspx`, 2011b.

Vu Hieu Nguyen. *Comportement dynamique de structures non-linéaires soumises à des charges mobiles* . PhD thesis, Ecole Nationale Des Pont et Chaussees, 2002.

Diethelm Wuertz, Martin Maechler, and Rmetrics core team members. Package 'stabledist' - Stable Distribution Functions. pdf and information available from `http://cran.r-project.org/web/packages/stabledist/index.html` , 2012.

Qinwu Xu and Mansour Solaimanian. Modeling linear viscoelastic properties of asphalt contrete by the Huet-Sayegh model. *International Journal of Pavement Engineering*, 10:401–422, 2009.

Y. Richard Kim. *Modeling of Asphalt Concrete*. McGraw-Hill, 2009.

P. Gómez Zamorano and F.A. Uribe Campos. On the Application of the numerical Laplace transform for accurate electromagnetic transient analysis. *Revista Mexicana de Fí sica*, 53: 198–204, 2007.

Appendix

.1 Fourier Transform

The following is a short introduction to the Fourier transform albeit ignoring considerations of on which function spaces it is defined etc.

$$[\mathcal{F}f](\omega) := \hat{f}(\omega) := \frac{1}{\sqrt{2\pi}} \int_{-\infty}^{\infty} e^{-it\omega} f(t) \mathrm{d}t. \tag{1}$$

Reminding the reader of a few properties
Define the convolution $*$ of two functions $f, g : \mathbb{R} \to \mathbb{R}$ by:

$$(f * g)(x) := \int_{-\infty}^{\infty} f(y) g(x - y) \mathrm{d}y \tag{2}$$

Example .1.1 (Convolution)**.** The Fourier transform of a convolution of two functions is the product of the transforms of the function:

$$[\mathcal{F}(f * g)](\omega) = \hat{f}(\omega)\hat{g}(\omega) \tag{3}$$

$\diamond$

.1.1 Inverse Fourier Transform

$$[\mathcal{F}^{-1}\hat{f}](\omega) := f(t) := \frac{1}{\sqrt{2\pi}} \int_{-\infty}^{\infty} e^{it\omega} \tilde{f}(\omega) \mathrm{d}\omega. \tag{4}$$

.2 Laplace Transform

The Laplace transform is defined as follows:

$$[\mathcal{L}f](s) := \hat{f}(s) := \int_{0}^{\infty} e^{-st} f(t) \mathrm{d}t. \tag{5}$$

Example .2.1 (Step function)**.** The following function will make several appearances so define the Heaviside step function $H : \mathbb{R} \to \{0, \frac{1}{2}, 1\}$ by:

$$H(x) = \begin{cases} 0 & , \quad x < 0 \\ \frac{1}{2} & , \quad x = 0 \\ 1 & , \quad x > 0 \end{cases} \tag{6}$$

$$\begin{aligned} [\mathcal{L}H(t-\tau)](s) &= \int_0^\infty e^{-st} H(t-\tau) \mathrm{d}t \\ &= \int_\tau^\infty e^{-st} \mathrm{d}t \\ &= \int_{-s\tau}^{-\infty} e^u \frac{-1}{s} \mathrm{d}u = \frac{1}{s} \int_{-\infty}^{-s\tau} e^u \mathrm{d}u \\ &= \frac{1}{s} [e^u]_{-\infty}^{-s\tau} \\ &= \frac{e^{-s\tau}}{s}. \end{aligned} \tag{7}$$

◇

Example .2.2 (Rectangular pulse/indicator function)**.** From equation (7) is follows that the Laplace transform of a rectangular pulse such as

$$\mathbb{1}_{[t_1,t_2]}(t) = \begin{cases} 0 & , \quad t < t_1 \\ 1 & , \quad t_1 \leq t \leq t_2 \\ 0 & , \quad t > t_2 \end{cases}, \tag{8}$$

is given by

$$[\mathcal{L}\mathbb{1}_{[t_1,t_2]}](s) = \frac{e^{-st_1} - e^{-st_2}}{s} \tag{9}$$

since $\mathbb{1}_{[t_1,t_2]}(t) = H(t-t_1) - H(t-t_2)$ [2].

◇

Example .2.3 (Convolution)**.** For $f : \mathbb{R}^+ \to \mathbb{R}$ define (Not to be confused for complex conjugation.)

$$\bar{f}(x) := \begin{cases} 0 & , \quad x < 0 \\ f(x) & , \quad x \geq 0. \end{cases} \tag{10}$$

[2]Technically only almost everywhere except the two points t_1 and t_2 where the Heavyside functions takes the value $\frac{1}{2}$, but the integral transform cannot distinguish this.

For $f, g : \mathbb{R}^+ \to \mathbb{R}$ we define our convolution $*_+$ as:

$$\begin{aligned}
[f *_+ g](t) &:= [\bar{f} * \bar{g}](t) \\
&= \int_{-\infty}^{\infty} \bar{f}(t-\tau)\bar{g}(\tau)\mathrm{d}\tau \\
&= \int_{0}^{t} \bar{f}(t-\tau)\bar{g}(\tau)\mathrm{d}\tau \\
&= \int_{0}^{t} f(t-\tau)g(\tau)\mathrm{d}\tau,
\end{aligned}$$

since $\bar{g}$ kills the integrand for $\tau < 0$ and $\bar{f}$ when $t - \tau < 0 \Leftrightarrow \tau > t$.

$$\begin{aligned}
[\mathcal{L}(\bar{f} * \bar{g})](s) &= \int_0^{\infty} e^{-st} \int_0^{t} f(t-\tau)g(\tau)\mathrm{d}\tau\mathrm{d}t \\
&= \int_0^{\infty} e^{-st} \int_{-\infty}^{\infty} \bar{f}(t-\tau)\bar{g}(\tau)\mathrm{d}\tau\mathrm{d}t \\
&= \int_{-\infty}^{\infty} \int_0^{\infty} e^{-st}\bar{f}(t-\tau)\mathrm{d}t\ \bar{g}(\tau)\mathrm{d}\tau \\
&= \int_{-\infty}^{\infty} e^{-s\tau}\bar{g}(\tau)\mathrm{d}\tau \int_0^{\infty} e^{-su}\bar{f}(u)\mathrm{d}u \\
&= [\mathcal{L}f](s)[\mathcal{L}g](s), \qquad (11)
\end{aligned}$$

where the substitution $u = t - \tau$ was made so $\mathrm{d}u = -\mathrm{d}\tau$ and $u_1 = -\infty$ and $u_2 = -\tau$.

$\diamond$

Example .2.4 (Derivative)**.** Assuming the following integrals makes sense, i.e. that the derivative of f to be of exponential type:

$$\begin{aligned}
[\mathcal{L}(Df)](s) &= \int_0^{\infty} e^{-st}\frac{df}{dt}(t)\mathrm{d}t \\
&= \left[e^{-st}f(t)\right]_0^{\infty} - \int_0^{\infty} \frac{d}{dt}e^{-st}f(t)\mathrm{d}t \\
&= 0 - f(0) + s\int_0^{\infty} e^{-st}f(t)\mathrm{d}t \\
&= s[\mathcal{L}f](s) - f(0). \qquad (12)
\end{aligned}$$

$\diamond$

Example .2.5 (Integral)**.**

$$\begin{aligned}\left[\mathcal{L}\left(\int_0^t f(\tau)\mathrm{d}\tau\right)\right](s) &= \int_0^\infty e^{-st}\int_0^t f(\tau)\mathrm{d}\tau\mathrm{d}t \\ &= \int_0^\infty e^{-st}\int_0^\infty H(t-\tau)f(\tau)\mathrm{d}\tau\mathrm{d}t \\ &= \int_0^\infty f(\tau)\int_0^\infty e^{-st}H(t-\tau)\mathrm{d}t\mathrm{d}\tau \\ &= \int_0^\infty e^{-s\tau}f(\tau)\tau\int_0^\infty e^{-su}H(u)\mathrm{d}u\mathrm{d} \\ &= \frac{1}{s}\int_0^\infty e^{-s\tau}f(\tau)\mathrm{d}\tau\int_{-\infty}^0 e^{w}\mathrm{d}w \\ &= \frac{1}{s}[\mathcal{L}f](s) \end{aligned} \tag{13}$$

◇

Example .2.6 (Polynomial)**.** Let $m \in \mathbb{N}$, $\beta \in \mathbb{R}$.

$$\begin{aligned}\mathcal{L}[t^{m-\beta-1}] &= \int_0^\infty e^{-st}t^{(m-\beta)-1}\mathrm{d}t \\ &= s^{m-\beta-1}\int_0^\infty e^{-u}u^{(m-\beta)-1}\mathrm{d}u \\ &= \frac{s^{-(m-\beta)+1}}{s}\int_0^\infty e^{-u}u^{(m-\beta)-1}\mathrm{d}u \\ &= s^{-(m-\beta)}\Gamma(m-\beta) \end{aligned} \tag{14}$$

◇

.2.1 Fractional Calculus

Define for $\alpha > 0$ the fractional integral, see [Debnath and Bhatta, 2007] of order α as:

$${}_aD_t^{-\alpha}f(t) = \frac{1}{\Gamma(\alpha)}\int_a^t (t-\tau)^{\alpha-1}f(\tau)\mathrm{d}\tau. \tag{15}$$

Note that

$${}_0D_t^{-\alpha}f(t) = \frac{1}{\Gamma(\alpha)}(\cdot)^{\alpha-1} *_+ f \tag{16}$$

Giving

$$\begin{aligned}[\mathcal{L}_0D_t^{-\alpha}f](s) &= \frac{1}{\Gamma(\alpha)}\mathcal{L}\int_0^t (t-\tau)^{\alpha-1}f(\tau)\mathrm{d}\tau. \\ &= \frac{1}{\Gamma(\alpha)}\mathcal{L}[(\cdot)^{\alpha-1} *_+ f] \\ &= s^{-\alpha}[\mathcal{L}f](s), \end{aligned}$$

Therefore

$$[\mathcal{L}\ {}_0D_t^{-\alpha_1}\ {}_0D_t^{-\alpha_2} f](s) = s^{-\alpha_1}[\mathcal{L}\ {}_0D_t^{-\alpha_2} f](s) = s^{-\alpha_2}s^{-\alpha_1}[\mathcal{L}f](s) = [\mathcal{L}_0D_t^{-(\alpha_1+\alpha_2)} f](s), \quad (17)$$

and by $\mathcal{L}^{-1}$ we have the exponentiation law for the fractional integral.
The Caputo fractional derivative, see [Adam Loverro, 2004], of a function f of order $\beta > 0$ we define as

$$ {}_0D_t^{\beta} f(t) := {}_0D_t^{-(m-\beta)} D^m f(t) = \frac{1}{\Gamma(m-\beta)} \int_0^t (t-\tau)^{m-\beta-1} f^{(m)}(\tau) \mathrm{d}\tau \quad (18)$$

where $m \in \mathbb{N}$, $m \geq \lceil \beta \rceil$ so that $m - \beta > 0$ and the fractional integral as in equation (15) can be applied.

$$[\mathcal{L}\ {}_0D^{\beta} f](s) = \frac{1}{\Gamma(m-\beta)} \int_0^{\infty} e^{-st} \int_0^t (t-\tau)^{m-\beta-1} f^{(m)}(\tau) \mathrm{d}\tau \mathrm{d}t$$

Assuming $f^{(i)}(0) = 0$ for $i = 1, \ldots,$.

$$\begin{aligned} [\mathcal{L}\ {}_0D_t^{\beta} f](s) &= s^{-(m-\beta)} \mathcal{L}\left[\frac{\mathrm{d}^m f}{\mathrm{d}t^m}\right] \\ &= s^{-\beta}\hat{f}(s) \end{aligned} \quad (19)$$

.2.2 Inverse Laplace Transform

The inverse Laplace transform done numerically in this study follows [Zamorano and Campos, 2007].

$$f(t) = [\mathcal{L}^{-1} f](t) := \frac{1}{2\pi i} \lim_{\gamma \to \infty} \int_{c-i\gamma}^{c+i\gamma} e^{-st} \hat{f}(s) \mathrm{d}t. \quad (20)$$

As a reminder for $b \in R$ we have $\cos(b) = \cos(-b)$ and $-\sin(b) = \sin(-b)$ so $e^z = e^{a+ib} = e^a(\cos(b) + i\sin(b)) \Rightarrow \overline{e^z} = e^a(\cos(b) - i\sin(b)) = e^a(\cos(-b) + i\sin(-b)) =: e^{a-ib} =: e^{\overline{z}}$. Hence if assuming f is real valued and since $t \in \mathbb{R}$ by conjugating we get the following from appendix .2:

$$\begin{aligned} \hat{f}(s) &= \int_0^{\infty} e^{-st} f(t) \mathrm{d}t \Rightarrow \\ \overline{\hat{f}}(s) &:= \overline{\int_0^{\infty} e^{-st} f(t) \mathrm{d}t} = \int_0^{\infty} e^{-\overline{s}t} \overline{f}(t) \mathrm{d}t \Rightarrow \\ &= \int_0^{\infty} e^{-\overline{s}t} f(t) \mathrm{d}t = \hat{f}(\overline{s}), \end{aligned}$$

leading to the conclusion that only $f(c + iw)$ for $w \in \mathbb{R}_0^+$ needs calculating, instead of $\mathbb{R}$ as it contains the information of $f(c - iw)$ already since this work deals with physical and there by real valued functions - deflections, stresses and strains.

.3 R Scripts

On the enclosed USB-disc find R scripts for

- Real TSD data synthetic model fitting.
- Laplace-FEM data synthetic model fitting.

See the contents.pdf file there for more information.

.4 Octave Scripts

On the enclosed USB-disc find Octave scripts for use in the post-processing.
See the contents.pdf file there for more information.

.5 COMSOL reports

On the enclosed USB-disc find a selection of COMSOL reports and model files.
See the contents.pdf file there for more information.

.6 Contour Integration for Inverse Fourier Transform

Here is described how to perform certain inverse Fourier transforms used in Chapter 3 using the method of contour integration. It is well-described in many textbooks.
For a polynomial P, let assume it to be of fourth degree:

$$P(z) = \sum_{n=0}^{4} a_n z^n, \tag{21}$$

to calculate the following integral f with $x \geq 0$.

$$f(x) = \int_{-\infty}^{\infty} \frac{e^{ixk}}{P(k)} \mathrm{d}k = \lim_{R\to\infty} \int_{-R}^{R} \frac{e^{ixk}}{P(k)} \mathrm{d}k, \tag{22}$$

observe that with $\gamma(t) := Re^{i\tau}$ and $\Gamma := \{\gamma(t) | t \in [0, \pi]\}$ then $\frac{\mathrm{d}\gamma}{\mathrm{d}\tau} = iRe^{i\tau}$

$$\lim_{R\to\infty} \left(\int_{-R}^{R} \frac{e^{ixz}}{P(z)} \mathrm{d}z + \int_{\Gamma} \frac{e^{ixz}}{P(z)} \mathrm{d}z \right) = \lim_{R\to\infty} \left(\int_{-R}^{R} \frac{e^{ixz}}{P(z)} \mathrm{d}z + \int_{0}^{\pi} \frac{e^{ix(R\cos(\tau)+iR\sin(\tau))}}{P(Re^{i\tau})} iRe^{i\tau} \mathrm{d}\tau \right), \tag{23}$$

which together is a semi-circular contour through the upper halfplane and along the real axis. The semi-circular part, the last integral, of equation (23) is now shown to contribute nothing.

$$\lim_{R\to\infty}\left|\left(\int_0^{\pi}\frac{e^{ix(R\cos(\tau)+iR\sin(\tau))}}{P(Re^{i\tau})}iRe^{i\tau}\mathrm{d}\tau\right)\right| \leq \lim_{R\to\infty}\left(\int_0^{\pi}\left|\frac{e^{ix(R\cos(\tau)+iR\sin(\tau))}}{P(Re^{i\tau})}iRe^{i\tau}\right|\mathrm{d}\tau\right) \tag{24}$$

$$= \lim_{R\to\infty}\left(\int_0^{\pi}\left|\frac{Re^{-xR\sin(\tau))}}{P(Re^{i\tau})}\right|\mathrm{d}\tau\right) \tag{25}$$

$$\leq \lim_{R\to\infty}\left(R\pi\left|\frac{\frac{R}{R^4}e^{-xR\sin(\tau_0))}}{a_4(e^{i\tau_0})^4+\cdots+\frac{R}{R^4}e^{i\tau_0}+\frac{a_0}{R^4}}\right|\right) \tag{26}$$

$$= \lim_{R\to\infty}\left(\pi\frac{|e^{-xR\sin(\tau_0))}|}{|a_4|R^2}\right) \tag{27}$$

$$= 0, \tag{28}$$

by using the estimation lemma and concluding the value of τ_0 for which the maximum is achieved is of no influence. For $x < 0$ using a clockwise contour through the lower halfplace will ensure still having the exponential decay in that case.
The conclusion is that the integral f is easily computed using the Cauchy Residue Theorem and identifying the residues at the roots of the polynomial P located in the upper or lower halfplane of $\mathbb{C}$ for $x \geq 0$ and $x < 0$ respectively by using a clockwise or counter-clockwise contour.

.7 TRA 2012 Article

The author submitted an article for TRA 2012 Athens which he intended to participate in. The publishing was conditional upon participation of an author. Since none of the authors ended up participating for various reasons, the author is actually not sure if it was ever printed in the proceedings. A copy has been enclosed on the USB-disc - it consists mostly of a 2d version of the work found in this text. Made as proof of concept and saving computation time.